DESIGN OF MASSIVE MIMO ANTENNA SYSTEM FOR 5G BASE STATIONS

BY

MONJED AL-TARIFI

A Thesis Presented to the
DEANSHIP OF GRADUATE STUDIES

KING FAHD UNIVERSITY OF PETROLEUM & MINERALS

DHAHRAN, SAUDI ARABIA

In Partial Fulfillment of the
Requirements for the Degree of

MASTER OF SCIENCE

In

ELECTRICAL ENGINEERING

MAY 2017

KING FAHD UNIVERSITY OF PETROLEUM & MINERALS
DHAHRAN 31261, SAUDI ARABIA

DEANSHIP OF GRADUATE STUDIES

This thesis, written by **MONJED AL-TARIFI** under the direction of his thesis adviser and approved by his thesis committee, has been presented to and accepted by the Dean of Graduate Studies, in partial fulfillment of the requirements for the degree of **MASTER OF SCIENCE IN ELECTRICAL ENGINEERING**.

Thesis Committee

Prof. Mohammad S. Sharawi (Adviser)

H. Masoudi 7/6/2017
Prof. Husain M. Masoudi (Member)

Dr. Ali Muqaibel (Member)

Dr. Ali Ahmad Al-Shaikhi
Department Chairman

Prof. Salam A. Zummo
Dean of Graduate Studies

15/6/17
Date

To my parents.

ACKNOWLEDGMENTS

At a main station in life, everyone has to stop at and express his thankfulness. Of course, the main thanks go to Allah, who just accepts whatever good things we do for his sake. Then my thanks go to my family, specially my parents, who encouraged me to complete studying and get higher educational degrees. After that, I really acknowledge that person who tolerated me and my dereliction, who stood with me and with all my mistakes, special thanks, of course, go to my advisor Prof. Mohammad Sharawi. Also, I don't forget all the professors whmo I dealt with, specially my committee members Prof. Husain Masoudi and Dr. Ali Muqaibel, for their efforts and revising my work with meaningful comments.

TABLE OF CONTENTS

LIST OF TABLES

LIST OF FIGURES

THESIS ABSTRACT

NAME:	Monjed Al-Tarifi
TITLE OF STUDY:	Design of Massive MIMO Antenna System for 5G Base Stations
MAJOR FIELD:	Electrical Engineering
DATE OF DEGREE:	May 2017

In this work, we provide a novel solution for future base station antenna systems. Future base station antenna systems will have powerful capabilities such as providing multiple simultaneous beams to large number of users to enhance the link quality and increase data throughput. The concept of massive multiple-input-multiple-output (mMIMO) weill be implemented. The presented design is the first to provide two modes of operation; namely multiple individual ports mode and beam switching mode for future 5G base station systems.

A 72 port mMIMO antenna system with switch beamsteering capability is presented for 5G base stations. Each side of the triangular antenna system consists of 3 layers with a total size of $44.4\times 29.6\times 0.1524$ *cm*^{3}*, and contains 24 ports. Each port (subarray) consists of 2×2 patches on the top layer, feeding lines with* *pre-calculated phases on the bottom layer and the ground layer is the middle one. The operating frequency is the potential 5G 3.6 GHz band. Each subarray (one port) is fed in a way to tilt its beam direction with respect to others to achieve uncorrelated channels. The design is fabricated and measured to test its performance. The minimum measured bandwidth is 100 MHz. The gain of a single port equals to 9.4 dBi. The envelop correlation coefficient does not exceed 0.12.*

The array operates in two modes; large MIMO and Beamsteered mMIMO. An algorithm to steer the beam of each 24-port side to different directions in space is derived and applied. 12 switched beams are obtained with elevation coverage up to 30 °. The total gain of the array dropped from 18.9 dBi at broadside direction to 11.93 dBi at 30 ° in elevation. The sidelobes also dropped from 11.2 dBi to 4.53 dBi. The half-power beamwidth (HPBW) is about 9 ° *at broadside, and it is 20 ° in elevation direction and 26 ° for the azimuth one in the direction of 30 ° beam.*

ملخص الرسالة

الاسم: منجد الطريفي

عنوان الدراسة: تصميم نظام هوائيات mMIMO لأبراج اتصالات الجيل الخامس

التخصص: الهندسة الكهربائية

تاريخ الدرجة العلمية: أيار 2017

في هذا العمل، قمنا بتوفير حل مبتكر لأنظمة هوائيات أبراج الاتصالات المستقبلية. أنظمة هوائيات أبراج الاتصالات المستقبلية سيكون لديها قدرات قوية مثل تزويد إشعاعات متعددة متزامنة لعدد كبير من المستخدمين لتحسين جودة الاتصال وزيادة إنتاجية البيانات. مفهوم نظام متعدد-المدخلات-متعدد-المخرجات كبير (mMIMO) سيتم تحقيقه. التصميم المعروض هو الأول الذي يزود نطاقين من التشغيل؛ نطاق منافذ متعددة تعمل لوحدها ونطاق تحديد اتجاه الإشعاع لأنظمة أبراج هوائيات الجيل الخامس 5G.

تم عرض نظام هوائيات mMIMO بـ72 منفذ مع قابلية توجيه الإشعاع لأبراج اتصالات 5G. كل جانب من نظام هوائيات ثلاثي الشكل يحتوي ثلاث طبقات مع حجم 44.4×29.6×0.1524 سنتيميتر مكعب، ويحتوي على 24 منفذ. كل منفذ (مصفوفة جزئية) يحتوي 2×2 هوائي patch على الطبقة العلوية، خطوط التغذية مع phases تم حسابها مسبقاً على الطبقة السفلية وطبقة الأرضي في المنتصف. تردد التشغيل هو نطاق 3.6 جيجاهيرتز المحتمل للـ5G. كل مصفوفة جزئية (منفذ واحد) تم تغذيته بطريقة لإمالة اتجاه الإشعاع بالنسبة للمنافذ الأخرى تحقيق قنوات غير مترابطة. تم تصنيع وقياس التصميم للتحقق من أدائه. أقل عرض للنطاق تم قياسه هو 100 ميجاهيرتز. مقدار الكسب ل منفذ واحد يصل إلى 9.4 dBi. مقدار مربع معامل الترابط لا يتجاوز 0.12. المصفوفة المصممة تعمل على نظامين؛ نظام MIMO كبير و mMIMO موجهة الإشعاع.

نظام حلول حسابي لتوجيه الإشعاع لكل جهة بـ24 منفذ لعدة اتجاهات بالفضاء تم اشتقاقها وتطبيقها. 12 إشعاع تم الحصول عليها مع تغطية بارتفاع 30 درجة. الكسب الكلي للمصفوفة تهبط من 18.9 dBi بالاتجاه العمودي إلى 11.93 dBi باتجاه ارتفاع 30 درجة. الإشعاع الجانبي أيضاً انخفض من 11.2 dBi إلى 4.53 dBi. عرض الإشعاع بنصف القدرة (HPBW) تقريباً 9 درجات بالاتجاه العمودي، و20 درجة ارتفاعاً و26 درجة عرضاً باتجاه ارتفاع 30 درجة.

CHAPTER 1

INTRODUCTION

Over time, the human life is becoming connected, and internet availability and connectivity everywhere at any time is becoming an integral part of our daily life. This can be clearly observed by the increasing demand on data rates. Engineers are working continuously to satisfy this demand.

In the 1980s, wireless systems started with the 1^{st} generation, and now the 4^{th} generation is used in most countries. In each generation, there are many improvements in size, functions and other features. But the main improvement is based on the increase in the channel capacity and data rate, which is the main aim of each new generation.

1.1 5G and Massive MIMO

Wireless generations (1G-4G) were proposed during the past few decades. Not only have smart-phones increased in numbers dramatically, but a lot of other wireless devices and applications are increasing very fast, such as small sensors and machine-to-machine as well. This huge evolution in wireless communications should be treated by the designers to overcome the demand of very high data transfers that include high definition video streams. Figure 1.1 shows the forecast of the coming few years in terms of devices and data traffic [1]. It is obvious how the increase in the demand of data transfer by 2021 will become. The increase of data traffic is growing exponentially with time. Also, the use of different devices other than mobile phone is increasing too.

Figure 1.1: Global Mobile Traffic Growth by Device Type [1].

So, new wireless systems should meet the requirements of this huge demand for data transfer. The next wireless communication generation (5G) is expected to see the light before 2020 to follow such demand of high data transmissions. A 1000 times increase in the capacity is to be achieved through the use of multiple enabling technologies [2]. Three major technologies have been introduced to help reach the expected capacity levels in 5G systems which are: ultra-densification, millimeter-wave (mm-Wave) based systems, and massive Multiple-Input-Multiple-Output (mMIMO) which will be the focus of this work [3]. Figure 1.2 shows some basic enabling technologies for 5G [4].

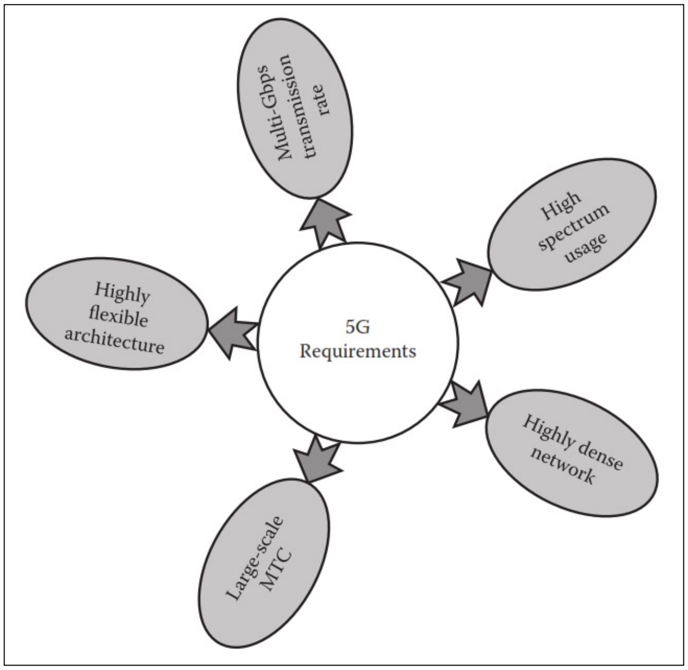

Figure 1.2: Key technology trends for 5G networks and their requirements [4] (MTC: Machine-Type communications.).

The currently applied wireless communication standard (4G) introduced by many technologies to enhance the channel capacity was the first to utilize MIMO technology. MIMO systems use multiple antennas at the transmitter and the receiver ends to send and receive multiple parallel data streams, thus increasing the data rates.

mMIMO or very large MIMO or titan MIMO, is a new technology that will be used in the next wireless communication generation (5G). In mMIMO, a large number of antennas (up to hundreds) will be used at the base station to serve the users. This antenna array (mMIMO antenna) has to be designed to transmit the signals to multiple users by beamforming techniques, that is called Multi-User MIMO (MU-MIMO). MU-MIMO system for downlink operation can be illustrated as in Figure 1.3.

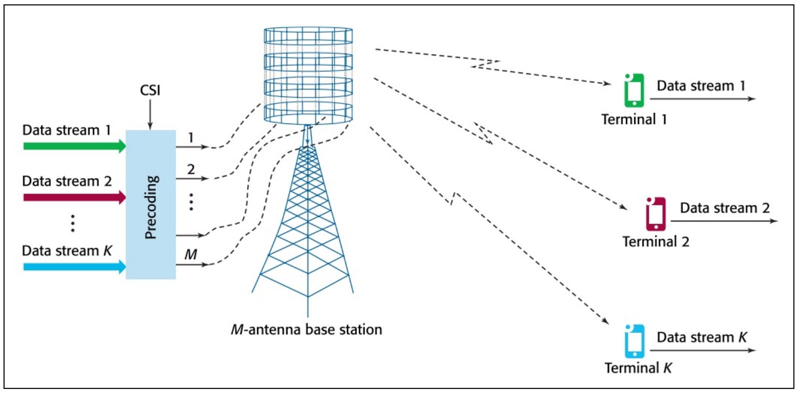

Figure 1.3: Downlink operation of a MU-MIMO link [5].

This MU-MIMO system operation can be done using precoding techniques that are defined in the literature, like Zero Forcing (ZF) and Matched Filter (MF) [2]. These techniques are used to suppress the interference between served terminals. The use of a large number of antennas at the base station side will increase the channel capacity as well [2]. A comparison between some precoding techniques is introduced in [6].

1.2 Features of Massive MIMO

Massive MIMO has many features that makes it a potential major candidate for future wireless standards. These features can be summarized by the following [2]:

1.2.1 Capacity Improvement

In mMIMO, the capacity can be increased to more than 10 times that of the capacity in Single-Input-Single-Output SISO wireless systems [2]. This increase in the capacity comes from better spatial multiplexing when using large number of antennas instead of small number in the ordinary MIMO (up to 8 antennas as in IEEE 802.11ac standards). In the ideal case, the channel capacity is a function of the number of transmitting and receiving antennas as in [7]:

$$C = B\ log_2(1 + M \times N \times SNR) \tag{1.1}$$

where B is the bandwidth of the channel, and SNR is the signal-to-noise ratio. N and M are the numbers of the transmitting and receiving antennas. It is obvious from the equation that the channel capacity is directly proportional to the number of antennas. So, the increase of the number of antennas at the base station side will raise up the channel capacity according to that. More details on the capacity will be explained in Chapter 2.

1.2.2 Energy Efficiency

When using a mMIMO antenna system, signals will be more directive to every user, not sent everywhere as in regular currently deployed base stations, so less loss in power is encountered towards unused directions.

Also, the data rate in MU-MIMO systems is improved by a factor of the number of antennas. Consider the uplink transmission, with perfect Channel State

Information (CSI) (CSI is the estimation of the channel effects at the transmitter and receiver, like scattering, fading, etc.). The achievable data rate for a user in a massive MIMO system, assuming single-antenna users, is [8]:

$$R \approx log_2(1 + Nd_k\rho_u)\ bits/sec/Hz \tag{1.2}$$

where N is the number of the antennas on the base station, d_k is the uplink large-scale fading coefficient. (Large-scale fading coefficient quantize the effect of the shadowing phenomena that affects the propagating signals due to large obstacles. Its value is a random variable with Gaussian distribution.) from the k^{th} user, where N is much larger than number of users K, and ρ_u is the up transmit power. On the other hand, in a SISO system, the data rate is given by [8]:

$$R \approx log_2(1 + d_k\rho_u)\ bits/sec/Hz \tag{1.3}$$

It can be noticed that the energy performance by a massive MIMO system is improved with a transmit power value of $\frac{\rho_u}{N}$ instead of ρ_u in a SISO system.

1.2.3 Inexpensive low-power components

Instead of bulky and high demanding power antenna elements, low-power antennas are used in massive MIMO because of the high number and low-cost elements. Also, in the classical base station array, the antennas are fed by high power amplifiers with bulky coaxial cables (with large diameter), which can be avoided in massive MIMO design because of lower power demanding antennas.

1.2.4 Reduction of latency

Fading of the signals is one of the most performance degradation phenomena during transmission. Utilizing multiple paths, as in massive MIMO, helps to limit the effect of fading, so this leads to lower latency in transmission. Also, if the terminal was at the fading dip, then the it has to wait for changing the channel propagation, which can be avoided by using multiple paths in mMIMO systems. The latency in 5G is supposed to reduced from 15 ms in 4G to about 1ms [3].

1.2.5 Robustness against jamming

In MU-MIMO systems, the signals are more robust against interference or jamming. This is achieved by beamforming the signal to a certain user, who will be less probable to be in the jammer side.

1.3 Work Motivation

mMIMO is one of the promising fields for research, since it is one of the main technologies for 5G. Just few works are there in the literature since mMIMO antennas has high number of element which means more size, cost and complexity. Having uncorrelated channels for a high number antenna system is one of the main challenges of designing MIMO systems.

In this work, the design of a mMIMO antenna system is presented. The system can be employed on the base station side for the 5G systems, and it works at 3.6 GHz operating frequency which is a band of LTE technologies and potential one for 5G backward compatibility. A high number of antennas are located at this system, which will increase the channel capacity compared with previous wireless generation. To get the antenna elements as uncorrelated ports, the concept of antenna arrays is used to tilt the beams of each port toward different directions. Then, the designed system is modified to operate the system as one antenna array with multiple beams.

1.4 Work Contributions

There are several contributions of this work:

1. Designed mMIMO antenna with 16 ports and 24 ports, operating at 3.6 GHz using FR4 (the most common substrate) and RO4350b (which is an efficient substrate), to compare their performance. The obtained bandwidth was 140 MHz with 30% efficiency when using FR4 material and more than 60% when using RO4350b.
2. Designed and implemented a triangular shape antenna array (as shown in Fig. 1.4) for base station using the designed board.
3. Tested and characterized the performance of the single board and the whole mMIMO system. Good agreement between simulation and measurement results was obtained.
4. Implemented a switched beamsteering algorithm for the designed 24 port mMIMO antenna that covered $\pm 32^o$ in θ-plane with HPBW of 26^o along

ϕ-plane, and maximum gain of 18.9 dBi.

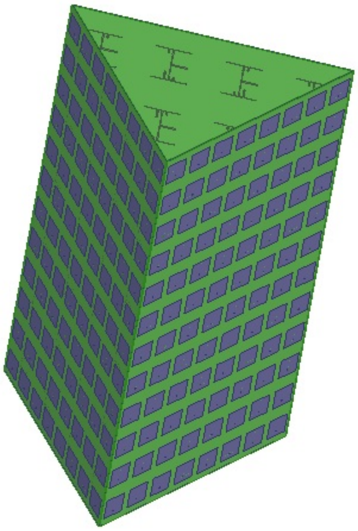

Figure 1.4: Triangular shape for base station system.

CHAPTER 2

THEORETICAL BACKGROUND

In this chapter, the performance metrics of mMIMO systems will be discussed along with their formulas. Then the concept of patch antennas and feeding networks will be presented.

2.1 Parameters of MIMO Antenna Systems

To characterize an antenna, there are many metrics to check its performance, such as the reflection coefficient, efficiency and directivity. On the other hand, using multiple antennas, as in MIMO systems, new additional metrics should be well defined to characterize the system properly as summarized in [9]. These new parameters will not be so different when scaling up to the mMIMO. The following subsections discuss these performance metrics.

2.1.1 Correlation Coefficient (ρ)

The correlation coefficient (ρ) describes how each antenna radiation can affect the radiation of other antennas when operated simultaneously. It is a metric that can provide a measurement of isolation between different channels of MIMO systems. The envelop correlation coefficient (ρ_e) or (ECC) (which is defined as approximately the square of the ρ) can be calculated using the following formula [10]:

$$\rho_e = \frac{\mid \iint_{4\pi} \vec{F_1}(\theta,\phi) * \vec{F_2}(\theta,\phi) d\Omega \mid^2}{\iint_{4\pi} \mid \vec{F_1}(\theta,\phi) \mid^2 d\Omega \ \times \iint_{4\pi} \mid \vec{F_2}(\theta,\phi) \mid^2 d\Omega} \tag{2.1}$$

where $\vec{F_1}(\theta,\phi)$ and $\vec{F_2}(\theta,\phi)$ are the radiation pattern of antenna 1 and antenna 2, respectively, in space coordinates if port 1 or port 2 is excited, respectively, and Ω represents the solid angle. The asterisk is the Hermitian product operator (conjugate multiplication).

For a lossless antenna, this equation can be reduced to a simple form to get the correlation coefficient using the S-parameters instead of the three-dimensional integral, by the following formula [10]:

$$\left|\rho_{ij}\right|^2 = \rho_{eij} = \left| \frac{\left|S_{ii}^* S_{jj} + S_{ij}^* S_{jj}\right|}{\sqrt{(1 - \left|S_{ii}^2 - S_{ji}^2\right|)(1 - \left|S_{jj}^2 - S_{ij}^2\right|)}} \right| \tag{2.2}$$

where ρ_{ij} is the correlation coefficient, and ρ_{eij} is the envelop correlation coefficient between elements i and j. The S-parameter S_{ij} is the coupling between the ith and jth element. But assuming a lossless radiating antennas is not the case in general, so, the radiation efficiency terms are added by some derivations in [11], at it is given as following:

$$\left|\rho_{ij}\right|^2 = \rho_{eij} = \left| \frac{\left|S_{ii}^* S_{jj} + S_{ij}^* S_{jj}\right|}{\sqrt{(1 - \left|S_{ii}^2 - S_{ji}^2\right|)(1 - \left|S_{jj}^2 - S_{ij}^2\right|)\eta_{radi}\eta_{radj}}} \right| \tag{2.3}$$

where η_{radi} and η_{radj} are the radiation efficiencies of antennas i and j, respectively. The value of envelope correlation coefficient in Eq.'s (2.2) and (2.3) are accurate for very limited cases, and Eq. (2.1) gives the exact value of all cases and should always be used.

2.1.2 Total Active Reflection Coefficient (TARC)

In addition to the reflection coefficient of each single element, total active reflection coefficient (TARC) describes the reflection coefficient for the whole system, taking adjacent ports effects and the coupling between the ports. In other words, TARC is the ratio between the total reflected power to the total incident power, and is given by the following equation [12]:

$$\Gamma_a^t = \frac{\sqrt{\sum_{i=1}^{N} \left|b_i\right|^2}}{\sqrt{\sum_{i=1}^{N} \left|a_i\right|^2}} \tag{2.4}$$

where Γ_a^t represents the total active reflection coefficient TARC for N element MIMO system, and b_i and a_i are the reflected and incident signals of port i, respectively. The values of b_i's can be found by applying known incident signals a_i's at each element, then find the b_i's using the S-parameters matrix using the following equation [12]:

$$\mathbf{b} = S\mathbf{a} \tag{2.5}$$

where **b** and **a** are the vectors of the reflected and incident signals, respectively. TARC value resides between 0 and 1. If it equals to zero, then the antenna will radiate the delivered power, and if one, total reflection happens.

2.1.3 Mean Effective Gain (MEG)

The transmitted signal is affected in the environment by channel fading, scattering environments and the noise in the channel. The antenna design plays an important role to deal with the environment effects. Mean effective gain (MEG) is the parameter that describes the effect of the environment on the radiation pattern. (It is a general antenna parameter, not just for MIMO systems.) The MEG can be calculated by the following set of equations [13]:

$$\int_0^{2\pi}\int_0^{\pi}\left[\frac{XPD}{1+XPD}G_\theta(\theta,\phi)P_\phi(\theta,\phi)+\frac{1}{1+XPD}G_\phi(\theta,\phi)P_\theta(\theta,\phi)\right]sin(\theta)d\theta d\phi \tag{2.6}$$

and

$$XPD = \frac{P_v}{P_H} \tag{2.7}$$

where XPD is the cross-polarization power ratio. The components $G_\theta(\theta, \phi)$ and $G_\phi(\theta, \phi)$ are the antenna gain components and $P_\theta(\theta, \phi)$ and $P_\phi(\theta, \phi)$ are the statistical distribution of the waves in the environment which should satisfy these conditions [13]:

$$\int_0^{2\pi} \int_0^{\pi} \left[G_\theta(\theta, \phi) + G_\phi(\theta, \phi)\right] sin(\theta) d\theta d\phi = 4\pi \tag{2.8}$$

$$\int_0^{2\pi} \int_0^{\pi} P_\theta(\theta, \phi) sin(\theta) d\theta d\phi = \int_0^{2\pi} \int_0^{\pi} P_\phi(\theta, \phi) sin(\theta) d\theta d\phi = 1 \tag{2.9}$$

2.1.4 Diversity Gain (DG)

Because of the fading of the signal in the channels, it is better to send multiple versions of the desired signal to achieve higher signal to noise ratio. This process is called diversity. Diversity has many types, one of them is the spatial diversity which is achieved by using MIMO systems. Diversity gain (DG) parameter describes the diversity of the communication system, and can be found by the following [14]:

$$DG = \left[\frac{\gamma_c}{SNR_c} - \frac{\gamma_1}{SNR_1}\right]_{p(\gamma_c < \gamma_s / SNR)} \tag{2.10}$$

where γ_c and SNR_c are the instantaneous and mean signal-to-noise-ratio (SNR) of the system, respectively, and γ_1 and SNR_1 are the instantaneous and mean SNR for the branch that has maximum values of γ and SNR among all branches. The DG value is conditioned by a probability that depends on a reference SNR

value. Assume that the channels are uncorrelated with Rayleigh distribution, the probability condition can be found by [14]:

$$P(\gamma_c < \gamma_s/SNR) = (1 - exp(-\frac{\gamma_s}{SNR}))^M \tag{2.11}$$

where M is the number of antennas. So, By increasing the number of elements, the diversity gain will increase.

2.1.5 Branch Power Ratio

Branch power ratio is the parameter that represents the relative power levels between the different antennas in the MIMO antenna system. It can be defined as the ratio between the minimum power level that can be obtained by any antenna in the system to the maximum power level from another antenna in the system. It is mathematically represented by [9]:

$$k = \frac{P_{min}}{P_{max}} \tag{2.12}$$

where k represents the branch power ratio, and P_{min} and P_{max} are the minimum and maximum power levels which can be obtained by the antennas in the system, respectively. It is better to get a higher branch power ratio (near to 0 dB) to get higher diversity gain. The minimum allowable value for branch power ratio is -3 dB to avoid a significant loss in diversity system performance.

2.1.6 System Capacity

One of the main reasons that leads to use MIMO systems is to increase the transmission channel capacity. Assuming an independent and identically distributed (i.i.d.) Gaussian transmit signals with perfect Channel State Information (CSI) at the receiver, the capacity in bits/s/Hz in this case has been derived in [6] as:

$$C = log_2(det(I_{N_t} + \frac{\rho}{N_t} H H^H)) \tag{2.13}$$

where N_t is the number of the transmitting antennas. ρ is the transmit power. I_{N_t} and H, are the $N_t \times N_r$ identity and channel matrices, respectively, where N_r is the number of receiving antennas.

By normalizing the propagation coefficients in H as $\mathrm{Tr}(HH^H)$=$N_t N_r$ ($\mathrm{Tr}(A)$ is the transpose of matrix A), where N_r is the number of the receiving antennas, the upper bound was derived in [8] as:

$$C \leq min(N_t, N_r) log_2(1 + \frac{\rho\, max(N_t, N_r)}{N_t}) \tag{2.14}$$

For different MIMO systems, channel capacity can be derived as following:

1. Point-to-Point MIMO

   For the Point-to-Point MIMO (not MU-MIMO), the uplink and downlink capacity limits are derived, and have been summarized in [8] as follows:

   - Uplink: where the user end is the transmitter and the BS is the receiver.

     In the case of mMIMO, the uplink receiving antennas are much larger than the transmitting antennas ($N_r \gg \ N_t$). Then, the upper bound of the capacity can be written as [8]:

$$C = N_t log_2(1 + \rho \, \frac{N_r}{N_t}) \tag{2.15}$$

- Downlink: In this case, the transmitting antennas are on the BS, and the receiving ones are on the user end. So, for mMIMO, the downlink transmitting antennas are much larger than the receiving ones ($N_t \gg N_r$). So, the upper bound of the capacity will be [8]:

$$C = N_r log_2(1 + \rho) \tag{2.16}$$

For about an infinite number of antennas at the base station side,and assuming that the row vectors of H are asymptotically orthogonal, the capacity can reach to the upper bound as shown previously. But this assumption, where the row of the channel matrix are asymptotically orthogonal, is not practically the case.

2. MU-MIMO

In mMIMO systems, MU-MIMO technology is supposed to be utilized. To derive the capacity for this system, the fading coefficients will have an effect on the achievable capacity as follows:

- Uplink: For the uplink case, the capacity can be written as [8]:

$$C = \sum_{k=1}^{K} log_2(1 + N\rho_u d_k) \tag{2.17}$$

where N is the number of antennas at the BS side, and K is the number of users who are served by this BS.

- Downlink: In this case, the capacity depends on the power allocation for each user, and can be written as [8]:

$$C = \max_{P}\ log_2\ det(I_K + \rho_d NPD) \tag{2.18}$$

where P is a $K \times K$ positive diagonal matrix of the power allocations for each user, D is a $K \times K$ matrix with large-scale fading coefficients, and ρ_d is the downlink transmit power.

2.2 Patch Antennas and Feeding Networks

In this section, an overview of antenna design will be discussed. The patch design procedure will be introduced with the basic calculation formulas. Then, the feeding network concept is explained with different structures used in designing it to meet the required excitations of the antenna elements.

2.2.1 Patch Antennas

The patch antenna simply consists of rectangle metal on one side, and an infinite ground plane on the other side. The design calculations based on the cavity model are formulated by closed form equations. The width of the patch is calculated by [15]:

$$W = \frac{c}{2f_r}\sqrt{\frac{2}{\epsilon_r + 1}} \tag{2.19}$$

where ϵ_r is the dielectric constant, f_r is the operating frequency and c is the speed of light ($3 \times 10^8 m/s$). Then, because of the microstrip line model, the effective dielectric constant ϵ_{eff} can be found by [15]:

$$\epsilon_{eff} = \frac{\epsilon_r + 1}{2} + \frac{\epsilon_r - 1}{2}\left[1 + 12\frac{h}{W}\right]^{-1/2} \tag{2.20}$$

where h is the thickness of the substrate. After that, to find the length of the patch, L, the extension, ΔL, should be calculated first by [15]:

$$\Delta L = 0.412h\frac{(\epsilon_{eff} + 0.3)(\frac{W}{h} + 0.264)}{(\epsilon_{eff} - 0.258)(\frac{W}{h} + 0.8)} \tag{2.21}$$

The value of this extension is used in the following formula to get the length of the patch [15]:

$$L = \frac{c}{2f_r\sqrt{\epsilon_{eff}}} - 2\Delta L \tag{2.22}$$

There are multiple ways to feed the patch antenna. The one that will be used in this work is the probe feeding mechanism. The position of the feeding probe specifies the input impedance of the antenna load.

2.2.2 Feeding Networks Design

To operate an antenna system as a MIMO system, the channels should be uncorrelated, so the radiation pattern by each port should be uncorrelated from the others. One method is to use beamsteering capability by an antenna array, where multiple antennas are distributed and excited by a specific excitation to steer the beam toward a desired direction.

For different amplitude and phase excitations for each element in the array, transmission lines are used with power dividing and phase shifting techniques (which is called a feeding network). The feeding network design is the most problematic part in designing such an antenna array.

T-junction Power Divider

Microstrip lines are widely used to design the feeding networks. The phase and amplitude excitation for each antenna element are based on the structure of the feeding network.

A T-junction is used to split the power coming from the port equally to each element. The geometry of a T-junction power divider is shown in Figure 2.1. To split the power equally, the impedances of the lines are calculated using [16]:

$$1/Z_1 + 1/Z_2 = 1/Z_0 \tag{2.23}$$

So, if Z_0 equals 50Ω, then for equally split ratio, Z_1 and Z_2 are 100Ω. The problem of this divider model in that the output ports of the power splitter are not isolated.

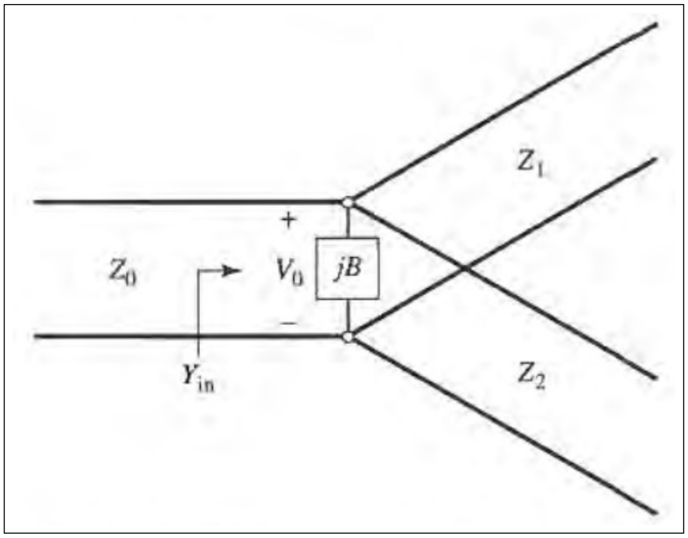

Figure 2.1: Transmission line model of T-junction power divider [16].

Phase Control

The phase excitation is determined using many ways. One of these ways is to use predefined phase shifter components, or to use a programmable varactor diode [17]. Another widely used way is to utilize different path length of the signal toward each antenna element , so the signal reaches to each element at different time, which means different phases. This can be achieved using meandering of the line to increase the length in the available space and this is the way that is used in this work.

Discontinuities

To compensate the effect of the discontinuities in the T-junction and other curves, many ways in literature are proposed. Fig. 2.2 shows some compensation techniques for T-junctions and 90^o bends that will be used in this work. In Fig. 2.2(a), the edge of the T-junction is chamfered with an angle according to the widths of input line, and split lines. Where Fig. 2.2(b) shows how to chamfer the 90^o bends depending on the line width.

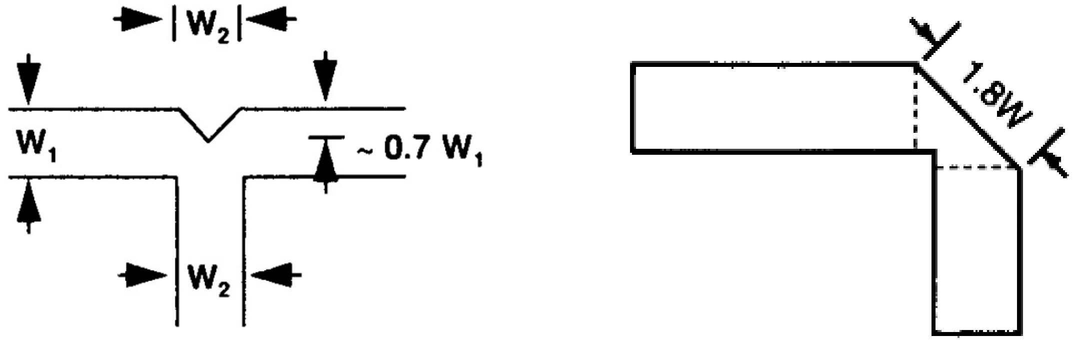

(a)

(b)

Figure 2.2: Discontinuity compensation of (a) T-junction and (b)90^o bend [18].

2.3 Full Wave Simulators

In this work, the design is simulated using two well-known simulators; ANSYS Electronics and CST Studio. Ansys Electronics, or High-Frequency-Structures-Simulator (HFSS), is a product by ANSYS, Inc. developers that provides 3D full-wave accuracy for 3D structure environment based on RF components and designs. The solver of HFSS is based on finite element method (FEM) algorithm [19].

CST Studio offers an EM solution with time domain solver, as well as frequency domain. Time domain is more time efficient than HFSS. The solver uses finite integral technique (FIT) method [20]. Both simulators are used among this work to verify the results and assure more accuracy before fabrication done.

2.4 Summary

In this chapter, the parameters of MIMO antenna systems were discussed. The main parameter that represents a MIMO performance is the correlation coefficient that describes how independent the channels are. The describing equations are presented to show the effects at each antenna parameter.

A discussion about microstrip patch antennas and microstrip transmission lines which are used in the feeding networks, is presented. The design formulas to calculate the dimensions of such structures were shown.

CHAPTER 3

LITERATURE REVIEW

Works on mMIMO systems from an antenna design point of view are not rich in literature, because it costs a lot and it is a new field. In this chapter, we present a comprehensive literature review covering all antenna systems that have appeared to date on the topic. Then, a comparison is presented between the different designs in the literature and the proposed design.

3.1 Active multibeam antenna using digital beamforming technology

A 64 RF channel and 256 antenna mMIMO antenna system was introduced by [21]. The 256 antennas are distributed along 8 PCBs (printed circuit boards), each with 8 × 4 antennas. Each 4 elements are placed in a row and connected to a single RF end. Figure 3.1 shows a single row layout of 4-patch elements.

These PCBs used a TLX-8 substrate, with $\epsilon_r = 2.55$ and a hight of $1mm$.

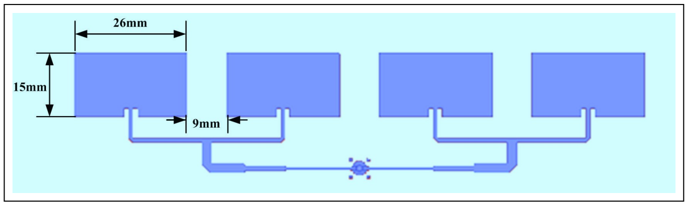

Figure 3.1: 4 patches with one RF end [21].

To reduce the coupling between the elements without having grating lobes, the spacing between them was 0.77λ, where the operating frequency is considered as 5.8 GHz with 200 MHz bandwidth. Figure 3.2 shows the gain radiation pattern with respect to θ.

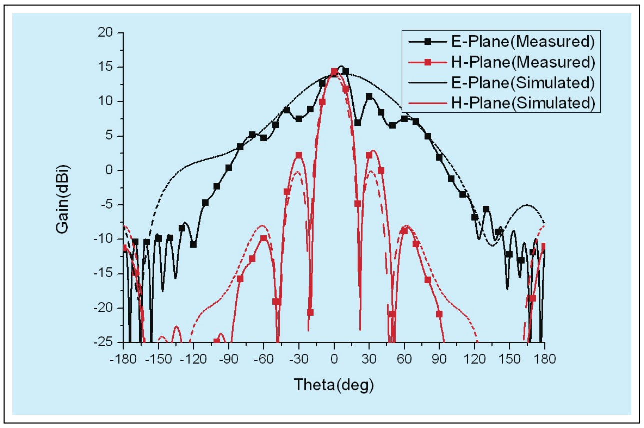

Figure 3.2: The RF channel of 4 patches radiation pattern [21].

The gain of the simulation results reaches 13 dBi, and the measured one is 11 dBi. Figures 3.3 and 3.4 shows the 32 elements PCB and the whole 256 antenna array.

The size of the single PCB is $320mm \times 215mm$. The total gain of the whole antenna array is about 18 dB. Figure 3.5 shows the beam sweep of the antenna array from -30^o to 30^o with steps of 10^o.

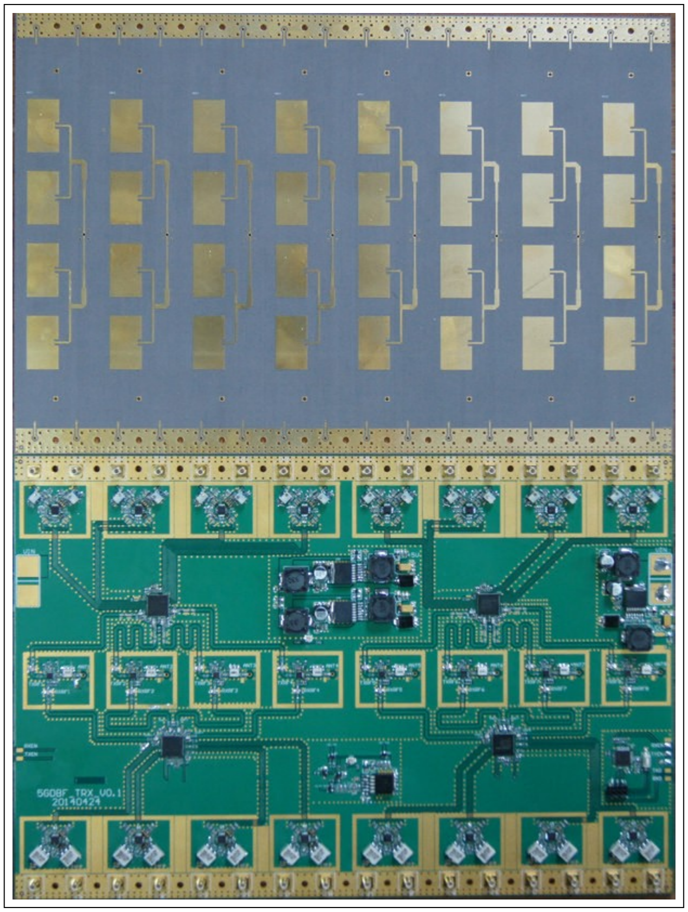

Figure 3.3: The 8 × 4 antennas PCB[21].

3.2 National Instruments

A collaboration between National Instruments (NI) and Lund University is created for mMIMO systems research topic, and they reached to a testbed that works at $3.7GHz$ as mentioned in [22]. They built a T-shaped array with 100 antenna patches. Diclad-880 substrate was used with $3.2mm$ hight to design the dual polarized $\frac{\lambda}{2}$ shorted patches. The final design is shown in Figure 3.6.

The measurements shows a $-10dB$ bandwidth of $183MHz$ with a reflection coefficient equals to $-28dB$ at $3.696GHz$, which is not far from the simulated results, where the bandwidth is $185MHz$, and the reflection coefficient at $3.7GHz$

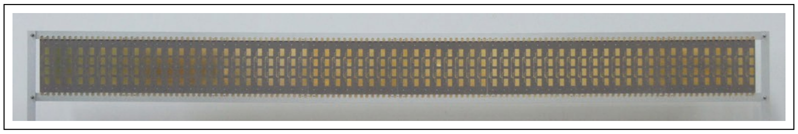

Figure 3.4: The whole 256 antenna array [21].

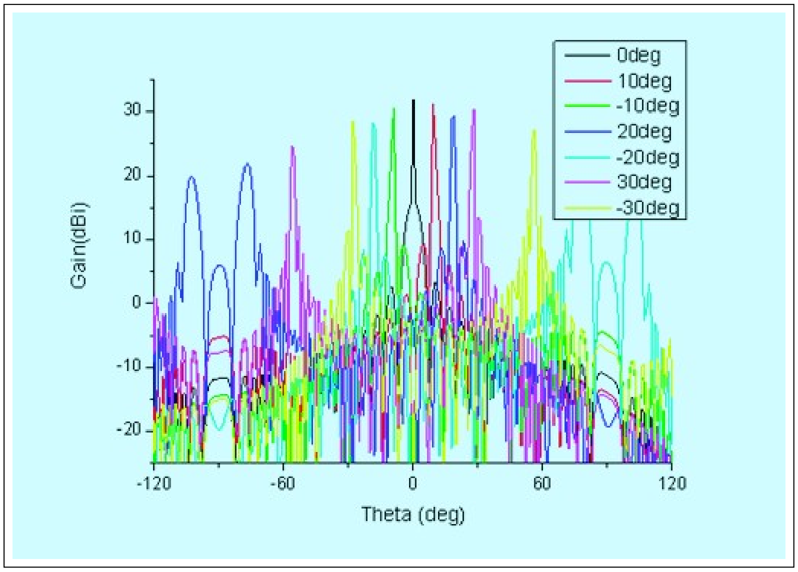

Figure 3.5: Beam sweep of the array [21].

is $-51dB$. The dimensions of the patches are not the same along the whole array to maintain a constant operating frequency.

3.3 Antipodal Linearly Tapered Slot Antenna (ALTSA) in a large array

A mMIMO antenna for Millimeter-wave applications base station was designed in [23]. This Array consisted of 36 sectors, with 4 × 4 elements to cover 10^o in azimuth plane. The single element consists of 4 antipodal linearly tapered slot antenna with Rogers substrate of $\epsilon_r = 2.94$ and hight of $1.016mm$, and with a single element geometry shown in Figure 3.7.

Figure 3.6: NI massive MIMO testbed [22].

This antenna operates at 38 GHz with a 15 dB bandwidth of 35 - 45 GHz, and a realized gain of 14.5 dBi. The half power beamwidth (HPBW) equals to 22^o and 38^o for E and H planes, respectively. The sector shape looks like as in Figure 3.8a.

The radiation pattern for the whole 36 sectors have been simulated and calculated by the array multiplication and have a results as shown in Figure 3.8b. The total realized gain at the operation frequency is $25.6 dBi$, and the HPBW equals to 10.7^o and 5.3^o in the azimuth and elevation planes, respectively.

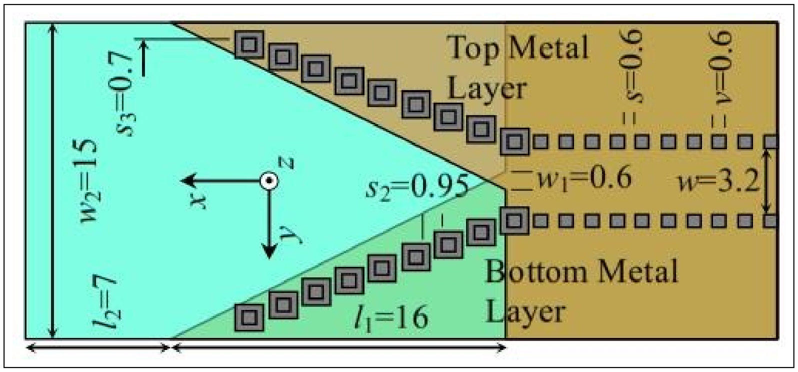

Figure 3.7: Antipodal Linearly Tapered Slot antenna with horn shape (ALTSA) [23].

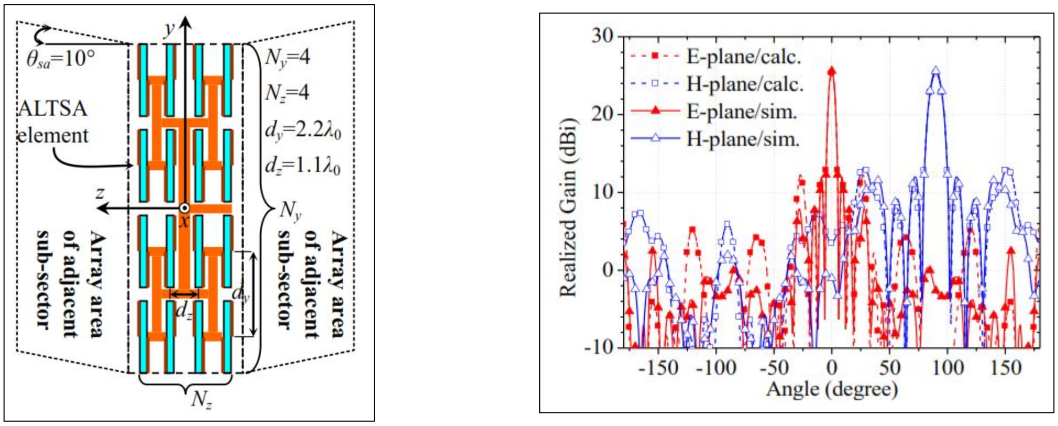

(a)

(b)

Figure 3.8: (a) A sector of 36 ALTSA antennas. (b) The realized gain pattern of the whole array [23]

3.4 A mMIMO using horn antennas for mmWave band by Samsung

A horn antenna can be used as shown in [24] withen MIMO configuration. They used a 12×4 antenna array with $(0.53\lambda, 2.71\lambda)$ spacing in the horizontal and vertical dimensions, respectively. Figure 3.9 present the design of the single horn element of this array. The dimensions (A, B) were equal to $(0.53\lambda, 2.71\lambda)$ and the HPBW is $(150^o, 20^o)$ in (H, E) planes. The gain of this single element is $10dB$.

The beamsteering in azimuth > $\pm 30^o$ which can cover a 60^o sector. Figure 3.10 shows the total array. The gain of the whole array becomes $25dB$. All results are obtained in the 28 GHz band. Because of the high frequency design the array size is so small, which is equal to $11.66cm \times 6.81cm$.

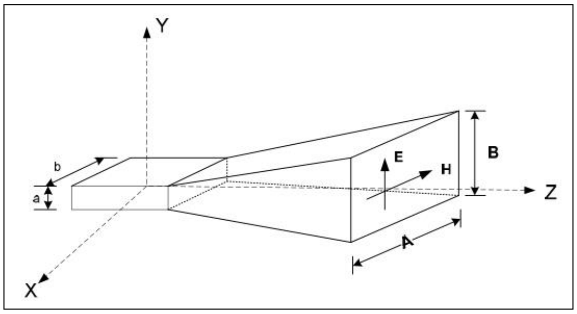

Figure 3.9: A horn antenna element [24].

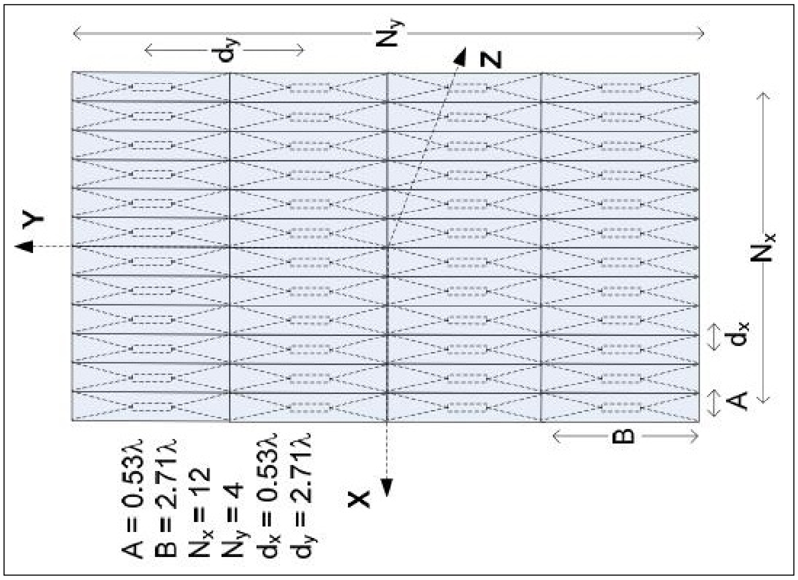

Figure 3.10: A horn antenna array [24].

3.5 Patch antenna array by Samsung

Researchers at Samsung came up with many designs of 2D active antenna array for mMIMO systems as shown in [25] and [26]. They used $8H \times 4V$ subarrays, with 4 patch antennas for each. The geometry of this array is shown in Figure 3.11. The bandwidth of this array is between 2.496 - 2.690 GHz for LTE band, and the HPBW is 24^o and 64^o for elevation and azimuth angles, respectively. The isolation between the adjacent elements is below than -16 dB and the gain is about 11.7 dB.

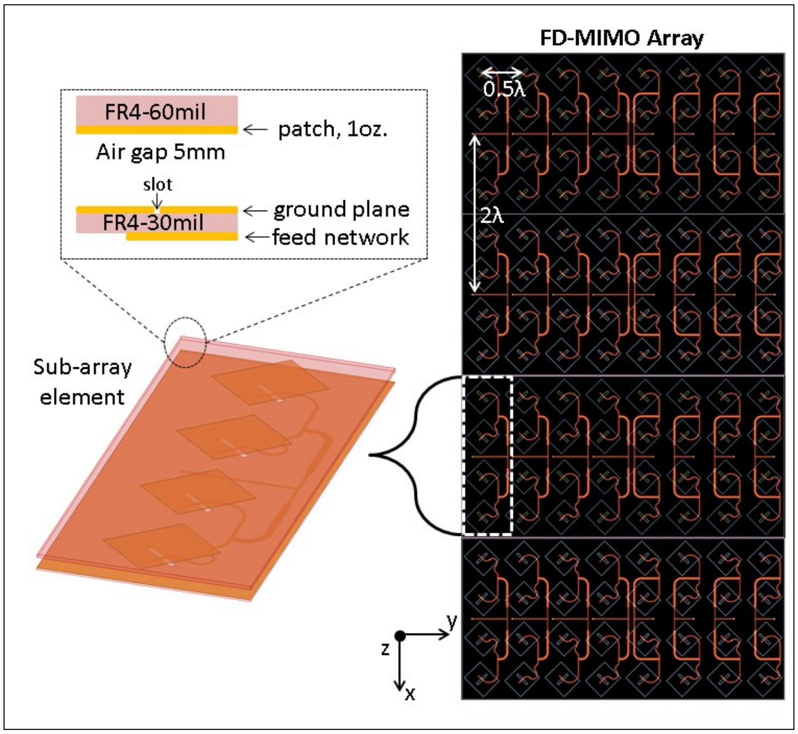

Figure 3.11: A patch antenna array [25].

3.6 108 Element Multimode Antenna Array for mMIMO

A design of 108 elements array is proposed in [27]. A 3 port antenna is designed at 2.4 GHz to get three modes by each. The design is shown in Figure 3.12.

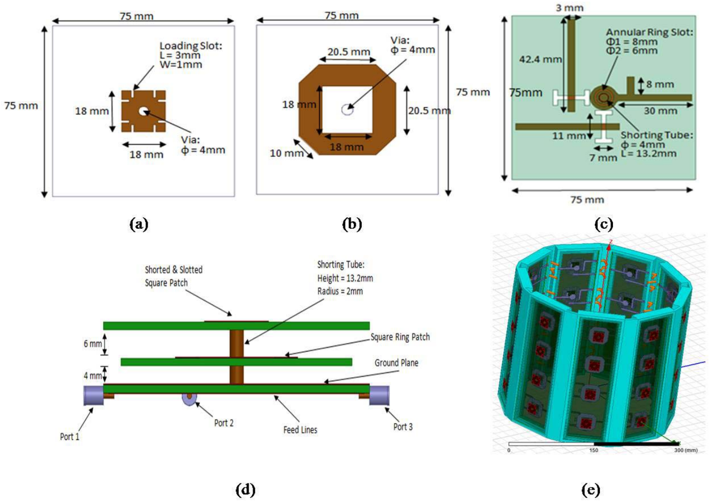

Figure 3.12: Geometry of designed multimode three-port antenna by [27].

This antenna system is simulated and one element is fabricated.The measurement results are shown in Figure 3.13. The bandwidth at port 1 is 254 MHz, at port 2 is 238 MHz and at port 3 is 102 MHz. The measured peak gain was 6.5 dBi at ports 1 and 2, and 1.21 dBi at port 3.

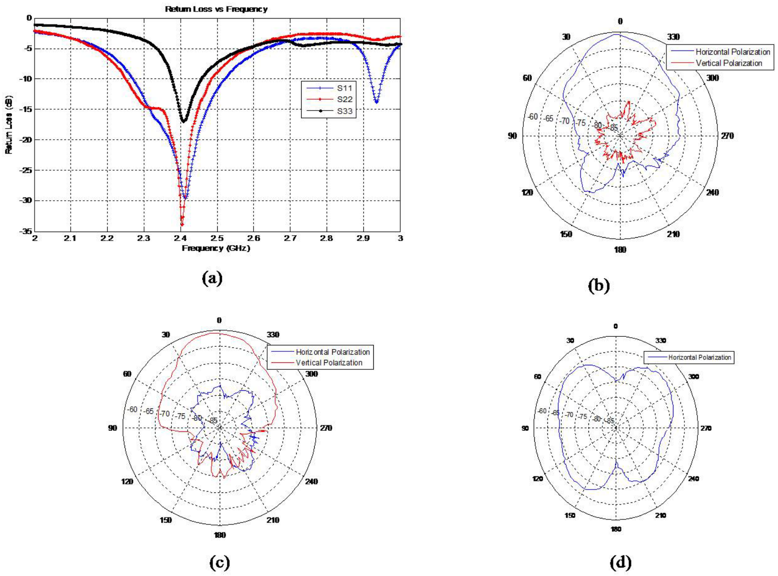

Figure 3.13: Measurement results of the designed antenna by [27]: (a) Reflection coefficients. (b)-(d) Radiation patterns of the three ports.

3.7 Compact dual-band mmWave mMIMO design

A dual-band mMIMO design was presented in [28] that operates at 28 GHz and 38 GHz. The total design is based on twelve sectors of 2×4 antenna elements, each one is an elliptical patch with series feeding network as shown in Fig. 3.14. The simulated gain is 12 dB at 28 GHz and 12.8 dB at 38 GHz.

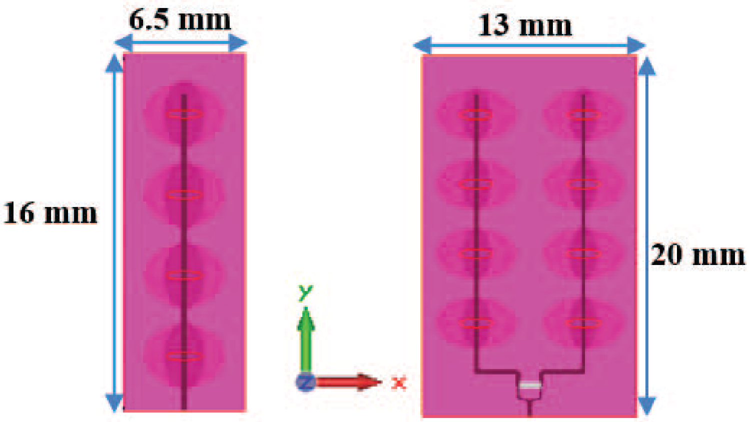

Figure 3.14: Geometry of designed Compact dual-band sector by [28].

3.8 Novel design of base station mMIMO system

A 144 ports design is shown in [29]. It is made of three layers stacked over each other, each consists of six sectors of four ports with a rotated deploying manner as shown in Fig. 3.15. Each port is an 2×2 subarray of dual polarized patches that is designed at 3.7 GHz. The measured bandwidth is 160 MHz with very low

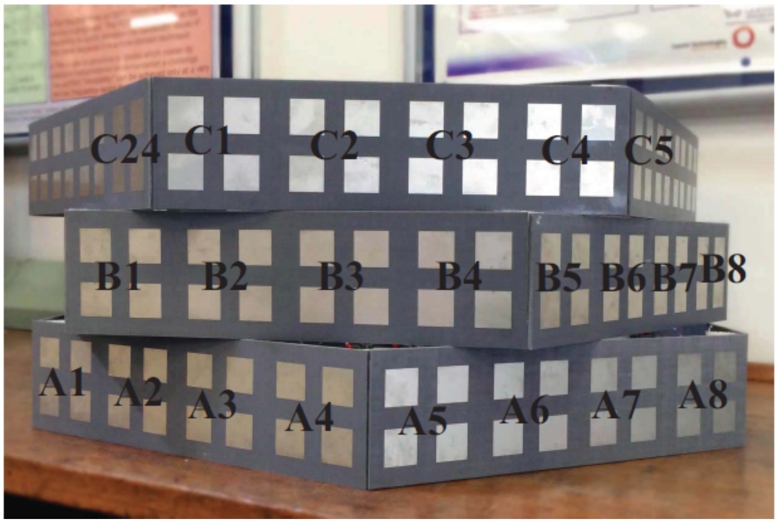

Figure 3.15: Geometry of three layers of 6 sectors mMIMO system by [29].

coupling between different ports (less than -32 dB). The realized gain by each subarray is 10.5 dB, and by each 4 ports sectors is 16.7 dB.

3.9 Low-profile closely spaced antennas for mMIMO system

In [30], a 4×4 antenna element array is presented for a sector of 6 sectors mMIMO system as shown in Fig. 3.16. Each sector contains four 4×1 subarrays of novel patch design with different feeding mechanisms that covers a band of 2.535-2.655 GHz. The coupling between different elements is less than -21 dB, and the gain by each subarray is 11-12.4 dBi

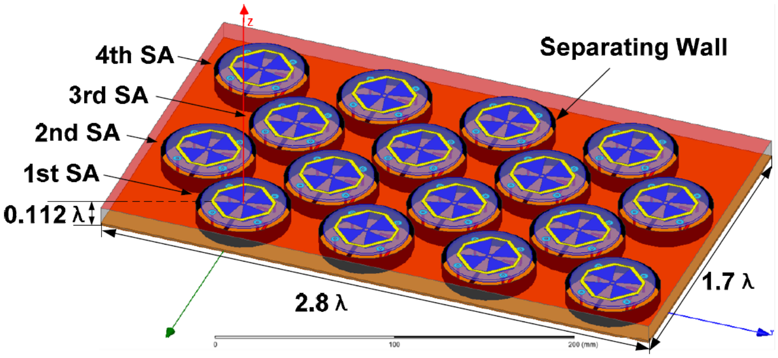

Figure 3.16: Geometry of single sectors mMIMO system by [30].

3.10 mMIMO panel array operating at Ka-band

A dual-polarization mMIMO array is presented in [31]. The array consists of 4×8 patches that is fed at two points to guarantee a dual-polarization operation as shown in Fig. 3.17. The patches are designed to cover 31.8-33.46 GHz band, and the maximum simulated coupling between different ports at this band is -15 dB.

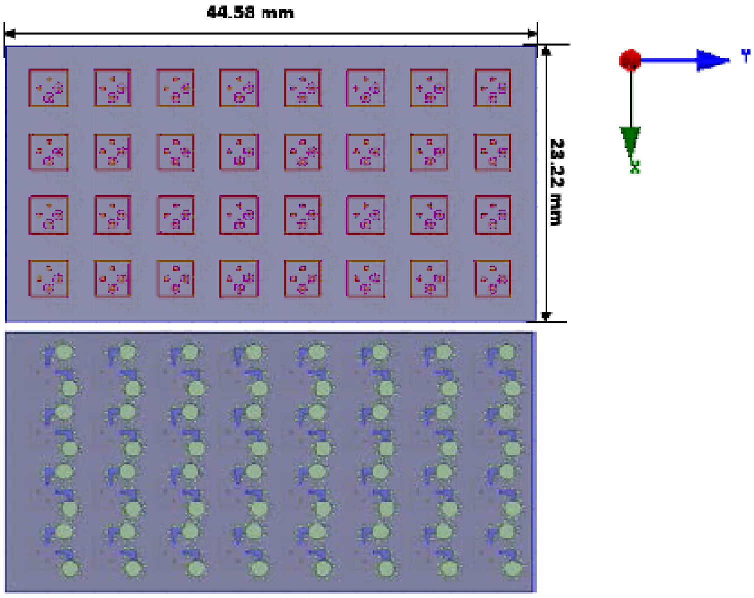

Figure 3.17: Top and bottom views of a panel of mMIMO system by [31].

3.11 UWB multimode mMIMO design

Novel mMIMO antenna system using theory of characteristic modes is introduced in [32]. The single panel consists of 11×11 antenna element as shown in Fig. 3.18, each one is a modified sheet to ensure covering four modes of operation. The antenna system covers an ultra wide band (UWB) of 6-8.5 GHz. The maximum coupling between ports is -20 dB, and maximum ECC is -20 dB, which assures good MIMO operation.

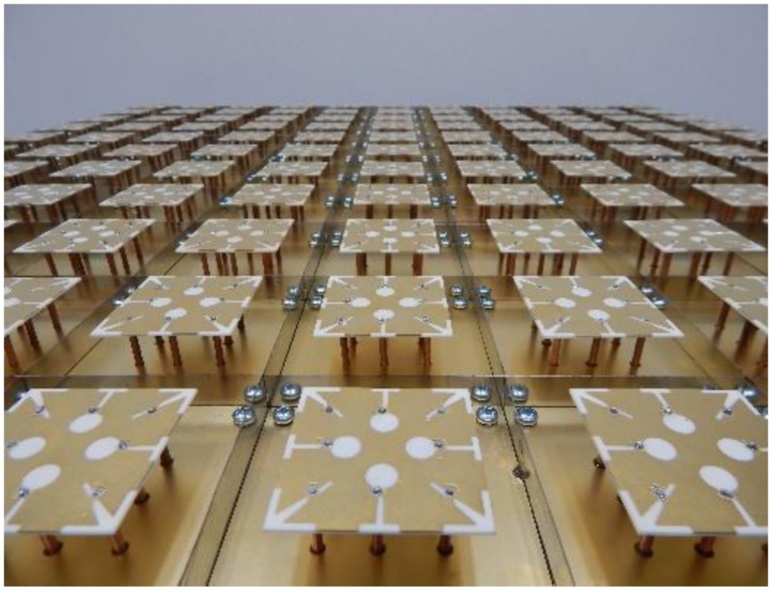

Figure 3.18: Prototype of a panel of mMIMO system by [32].

3.12 Other Designs

There are several companies that presented their work on massive MIMO with some details such as Nokia and Mitsubishi who came up with a 16 × 16 antennas massive MIMO system that operates at 3.5 GHz [33]. Figure 3.19 shows the prototype of a massive MIMO developed in [34]. This prototype consists of cylindrical system that contains 128 antenna ports which operated at 2.6 GHz. The diameter is 29.4 cm and the hight is 28.3 cm, and the spacing between adjacent antennas is about 6 cm.

Figure 3.19: mMIMO cylindrical prototype [34].

Another design is shown in [35] that is based on crossed-polarized dipole antenna elements that covers 3.6-4.8 GHz band.

3.13 Literature Review Summary

In summary, it is obvious that there is few works on mMIMO systems up to now. Also, those works that appeared in literature did not test the antenna parameters in terms of MIMO systems metrics. In literature, just two designs were based on mmWave band (28 and 38 GHz), which will be an important enabling technologies in 5G. Table 3.1 summarizes the work that has been done in literature and compares our proposed design to them.

It can be shown that most of the previous designs are based on patch antenna single element that work in array mode. In addition, the previous designs can work in array mode with beamfoarming techniques for MU-MIMO systems. In this work, the patch antennas will be excited in a way that will allow the system to operate in a MIMO mode using fixed tilted beams by each ports. Then, it will work as an array using the proposed beamsteering algorithm by exciting all ports at the same time. The proposed design has smaller size compared with those designs at the same operating frequency in [22] and [29].

In conclusion, the proposed design by this work can operate in two modes; MIMO mode and array one. MIMO mode is used for high signal-to-noise-ratio (SNR) environment scenarios when each port work individually, where array mode is used for low SNR scenarios by operating all ports as one antenna array. Since no mMIMO design is done before that operates at two modes in the same time, utilizing the both modes will be a new idea to do.

Table 3.1: Literature review summary.

Reference	**Band coverage**	**MIMO order (RF ports)**	**Single element type**	**Max. Gain (single port)**	**Max. Gain (single panel)**	**Geometry**	**Single sector size**	**Bandwidth (MHz)**	**Max. beam tilt**	**Prototype?**
[27]	2.4 GHz	9×12	multimode patch	6.5 dBi	-	Nonagon	7.5cm ×25.5cm	<254	-	No
[25], [26]	2.6 GHz	6×32	1×4 patches	10 dBi	-	Hexagonal	-	198	30^o	No
[30]	2.6 GHz	6×4	1×4 patches	9.2 dBi	11-12.4 dBi	Hexagonal	-	120	-	No
[33]	3.5 GHz	16	-	-	-	-	-	-	-	-
[22]	3.7 GHz	100 (single panel)	dual polarized patch	-	-	planar	60cm ×120cm	138	-	Yes
[29]	3.7 GHz	3×6×8	2×2 patches	10.5 dB	16.7 dBi	3× Hexagonal	32.4cm ×8.6cm	160	-	Yes
[35]	3.6-4.8 GHz	64 (single panel)	crossed-polarized dipoles	-	26.8 dBi	-	-	1200	-	No
[21]	5.8 GHz	64 (single panel)	1×4 patches	11 dB	18 dBi	Hexagonal	256cm ×21.5cm	200	30^o	Yes
[32]	6-8.5 GHz	121 (single panel)	four mode modified sheet	-	-	-	70cm ×70cm	2500	-	Yes
[24]	28 GHz	6×48	horn	9.47 dBi	26.28 dBi	Hexagonal	11.66cm ×6.81cm	-	30^o	No
[28]	28, 38 GHz	12×8	elliptical patch	12.07, 13.46 dBi	-	12 sectors	20mm ×13mm	-	-	No
[31]	32 GHz	32 (single panel)	dual polarized patch	~16 dB	-	-	23.22mm ×44.58mm	1660	47^o	No
[23]	38 GHz	36×16	Antipodal linearly tapered slot	14.5 dBi	25.6	36 sectors	-	10000	-	No
Proposed design	**3.6 GHz**	**3×24**	**2×2 patches**	**8.5 dBi**	**19.5 dBi**	**Triangular (can be hexagonal)**	**44.4cm ×29.6cm**	**100**	**34^o**	**Yes**

CHAPTER 4

DESIGN AND RESULTS

This chapter covers the proposed designs. The first section shows the first design that is done before taking some fabrication process details from the manufacturer in consideration, such as dimensions of vias, type of connectors, ... etc. Then, this proposed design is presented using FR4 and RO4350b substrate materials, with comparison of the performance between them and incorporating all the fabrication tolerances. At the end, the final design, that is fabricated, is shown with its measured characteristics.

4.1 First Design

In this section, the design of a single panel mMIMO antenna system is presented. The design is based on subarrays of 2×2 patches to get tilted beams for each port. At the beginning, the design of the patches will be discussed, then the feeding network will be designed to excite the patches with specific amplitude and phase values to tilt the beam of each subarray. After that, the single port (patch subarray with its feeding network) performance is shown. The 16 ports will be collected with a distribution of ports that have different beams to check the overall performance of the whole panel.

4.1.1 Patch Subarray Design

To design a mMIMO system, all ports have to be uncorrelated. To get this, each port is designed using an array of patches with different phase excitation at each, to tilt the beam toward different directions. The patches are designed at the top layer of the substrate. The hight of the substrate is 0.8 mm. An FR4 substrate is used with 4.1 dielectric constant and 0.02 loss tangent. The patches are designed at 3.6 GHz, which is used for LTE communication. The spacing between the patches is $\lambda/2$ to decrease the coupling between them and to avoid the appearance of grating lobes in the radiation pattern.

To find the dimensions of each single patch, equations (2.19)-(2.22) are used to calculate the length and width of the patch, and they are found as 20.42 mm and 26.09 mm, respectively. The probe feeding technique is used to feed the antenna with a specific input impedance.

The ANSYS Electronics Desktop (HFSS) simulator is used to check the performance of the patch with the calculated dimensions and to specify the 100 Ω input impedance position (the reason will be explained at the next section). After optimization of the dimensions, the layout of the top layer (antennas layer) and the simulation results are shown in Fig. 4.1. The matching at the resonance frequency reaches to -35 dB. The patches are well isolated, since the coupling between antennas is less than -23 at the operating frequency.

The next step is to find the optimum excitation of each patch to tilt the beam toward a specific angle in the space. Then, a feeding network will be designed to achieve the calculated amplitude and phase excitation at each antenna.

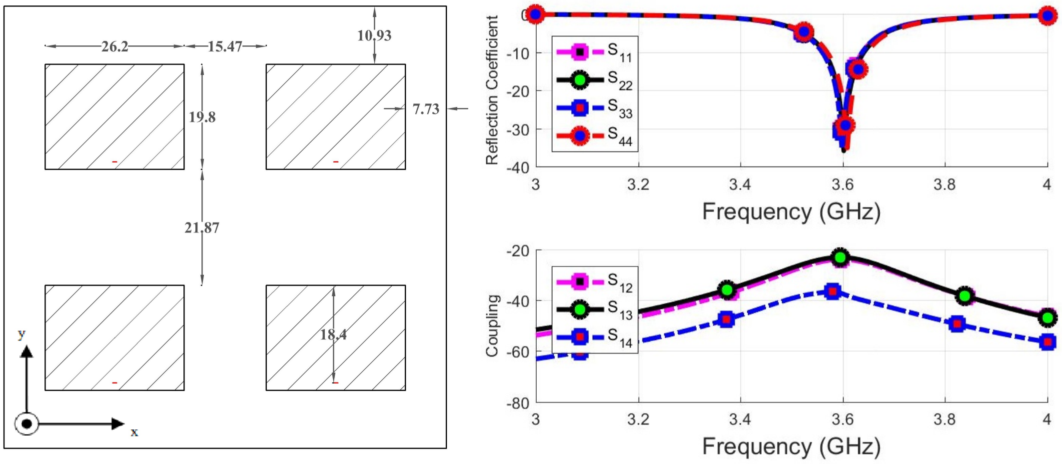

(a) (b)

Figure 4.1: (a) Four patches geometry. (All dimensions are in mm.) (b) Reflection and coupling coefficients for the four patches design.

4.1.2 Feeding Network Design

To tilt the beam radiated by an array of 2×2 antennas toward a specific direction in space, the elements should be excited to get the array factor has a maximum at the desired direction. The array factor for a planar array with constant amplitude excitation is defined as following [36]:

$$AF = \{\frac{sin(\frac{M}{2}\psi_x)}{sin(\frac{\psi_x}{2})}\}\{\frac{sin(\frac{N}{2}\psi_y)}{sin(\frac{\psi_y}{2})}\} \tag{4.1}$$

where M and N are the number of elements along the x and y, respectively. ψ_x and ψ_y are the progressive phases of the elements that is distributed along x and y axes, respectively, and they are defined as [36]:

$$\psi_x = kd_x sin\theta cos\phi + \beta_x \tag{4.2}$$

$$\psi_y = kd_y sin\theta sin\phi + \beta_y \tag{4.3}$$

where k is the wave number, and d_x and d_y are the spacing between the elements along x and y axes, respectively. β_x and β_y are the progressive phase excitation at the elements along x and y axes, respectively. To tilt the beam toward a specific angle in the space in terms of θ_0 and ϕ_0, the phase excitation should be as following [36]:

$$\beta_x = -kd_x sin\theta_0 cos\phi_0 \tag{4.4}$$

$$\beta_y = -kd_y sin\theta_0 sin\phi_0 \tag{4.5}$$

In our case, we need a good tilt along elevation direction (θ). If we choose the angles (θ,ϕ)=(45^o,45^o), the desired progressive phase excitations along the four patches are almost equal to (0^o,90^o,90^o,180^o). The phase difference can be represented with more length in transmission line of the feeding network to increase the phase excitation. Each 90^o phase is represented by $\lambda_g/2$ more length, which equals in terms of our FR4 substrate about 12 mm.

The feeding network is designed at beam directions (i.e. four directions at θ=45^o towards ϕ=45^o,135^o,225^o,315^o angles), it is firstly designed at one angle, and the other three are just a rotation of the phases between elements. Fig. 4.2 shows the designed feeding network for the first port with its dimensions.

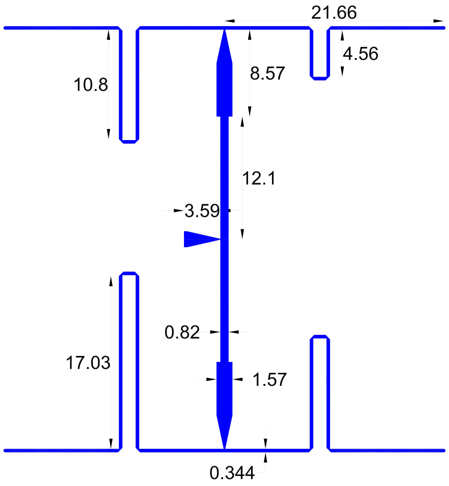

Figure 4.2: Feeding network for single port array. (the dimensions are in mm)

From the figure, the phases of each port is designed as an additional length. The angles here are assumed as $(0, 90, 90, 180)$ degrees to get a tilt angle at θ=45^o, ϕ=45^o. So, the line length toward each port is 12 mm for each 90 degrees, which means that angles of $(0, 90, 90, 180)$ degrees need $(0, 12, 12, 24)$ mm added length to excitation lines of each element, respectively. The feeding network is simulated to find the transmission coefficients from the input to each port for the check of amplitude and phase excitation, and the results are as in Fig.'s 4.3 and 4.4, respectively.

It is obvious that the maximum difference between amplitudes at each port is about 3 dB, which is not negligible, but it can be accepted if the proposed

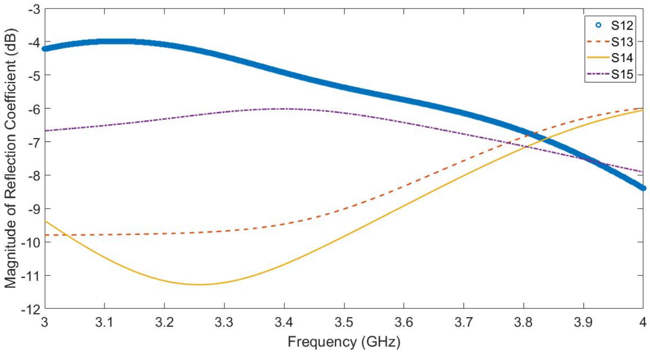

Figure 4.3: Amplitude transmission coefficients for the first feeding network.

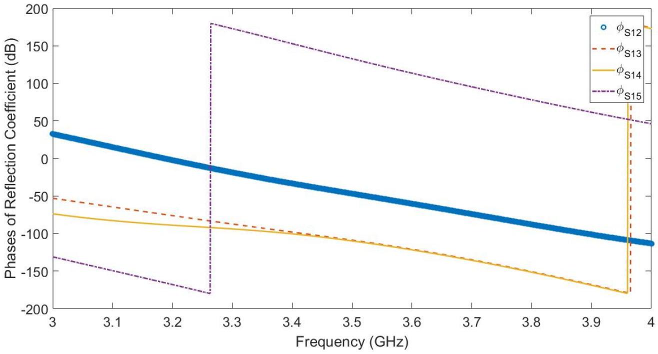

Figure 4.4: Phase transmission coefficients for the first feeding network.

tilt of the beam by the 2 × 2 patches is achieved. The resultant phases are about $(113, -121, -121, -60)$ or $(0, 126, 126, 187)$ degrees. But still with these deviations between the desired and simulated excitations, the pattern will be near to the expected maximum tilt. The excitation results are tabulated in Table 4.1.

Table 4.1: Excitation at patches results for single port array.

Port excitation	@1st patch	@2nd patch	@3rd patch	@4th patch
Desired phases	0	90	90	180
Resultant phases	0	126	126	187
Line extension lengths (mm)	0	12	12	24
Desired amplitudes (dB)	-6.02	-6.02	-6.02	-6.02
Resultant amplitudes (dB)	-5.75	-8.32	-8.91	-6.43

4.1.3 Single port design

The feeding network that is designed in the second section as added to a new layer in the bottom of the patches to achieve the desired excitations to the antenna elements. In simulation, the dimensions are modified again to get the resonance at the desired frequency. The single port geometry is shown in Fig. 4.5.

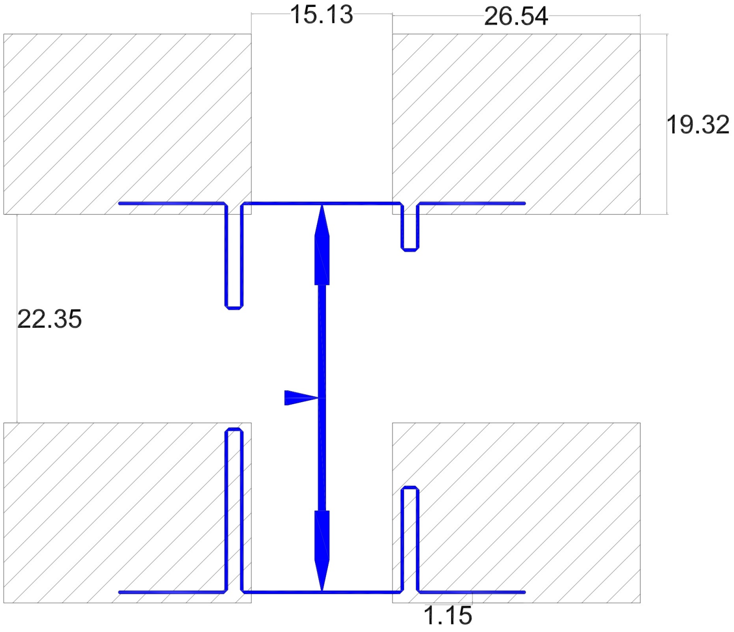

(a)

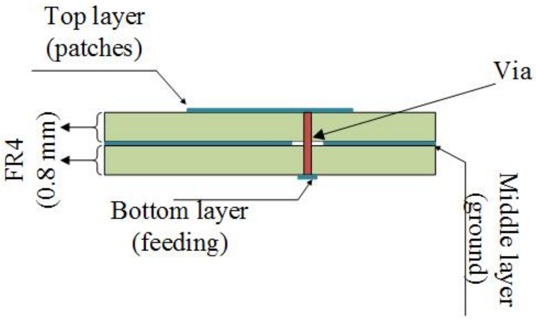

(b)

Figure 4.5: (a) Single port geometry. (All dimensions are in mm.) (b) Stack up view of the structure.

This single port is simulated, and the reflection coefficient is shown as in Fig.

4.6. Its -10 dB bandwidth is between 3.54-3.72 GHz. The 3D radiation pattern in terms of realized gain is shown in Fig. 4.7. It shows the tilt of the beam toward 28^o in elevation direction, which is different than the calculated one (45^o) because that the calculated one is based on isotropic antenna elements, which is not the case. The other three ports are just a rotation between the lines with different lengths in the feeding network.

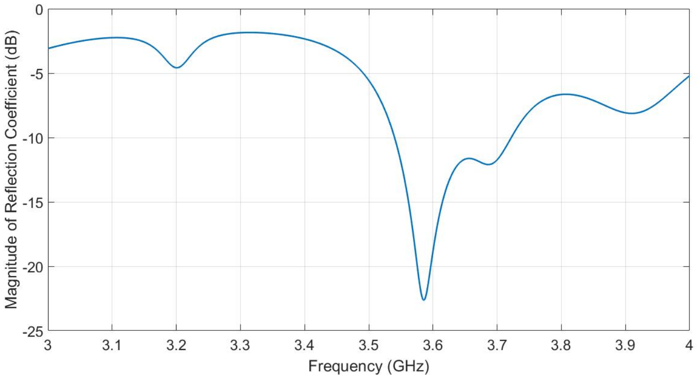

Figure 4.6: Reflection coefficient of a single port.

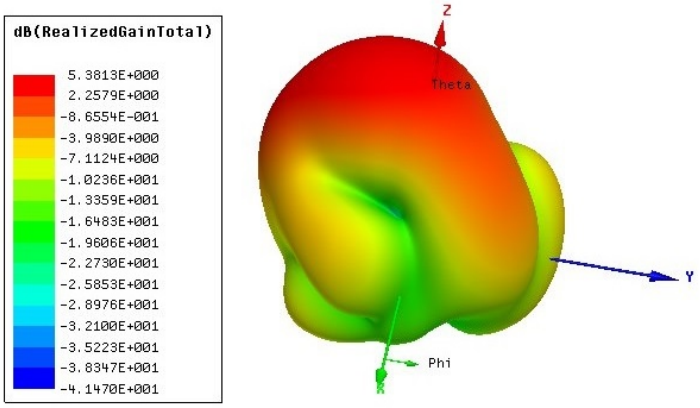

Figure 4.7: 3D realized gain pattern of a single port.

4.1.4 16 Ports mMIMO Panel Design

To design a mMIMO system, the different ports have to be uncorrelated. To achieve this, the single panel of mMIMO system consists of a distributed single ports that are designed in the previous section along the whole panel, and to get their patterns uncorrelated. The final shape of the design is an 8 × 8 patches, which is 4×4 MIMO as shown in Fig. 4.8. Notice the distribution of the ports according to the distribution of the feeding lines, which means the distribution of the patterns.

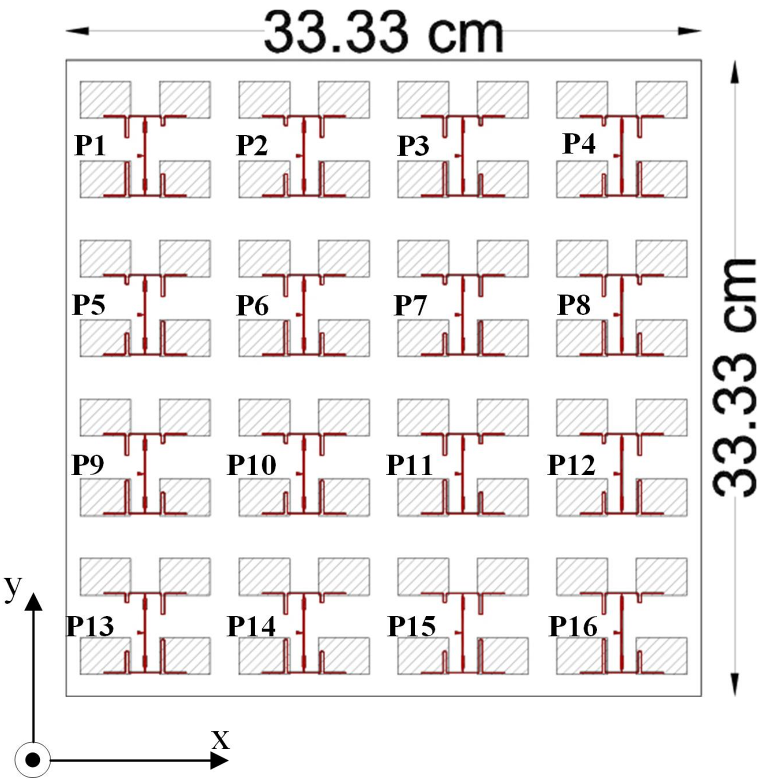

Figure 4.8: 16 port MIMO design (single panel).

This total array (Fig. 4.8) is simulated (using HFSS) to get its performance. The reflection coefficient is as shown in Fig. 4.9. It is shown that the -10 dB bandwidth from 3.45-3.68 GHz with -31 dB minimum reflection coefficient. The differences in the response of the reflection coefficient between the different 16 ports comes from their relative position with each other, and the size of ground plain below them (if the port at edge of in center). For the other directions, the reflection coefficient has the same response as in the first direction.

The coupling between the ports is shown in Fig. 4.10. A middle port is chosen to find the coupling with the adjacent ports. A good isolation is achieved at the operating frequency (3.6 GHz), which is about 25 dB at minimum.

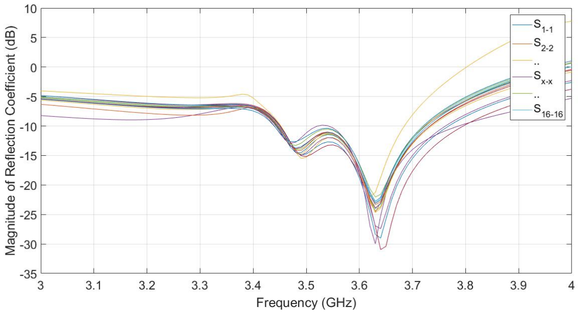

Figure 4.9: Reflection coefficient for all 16 ports array.

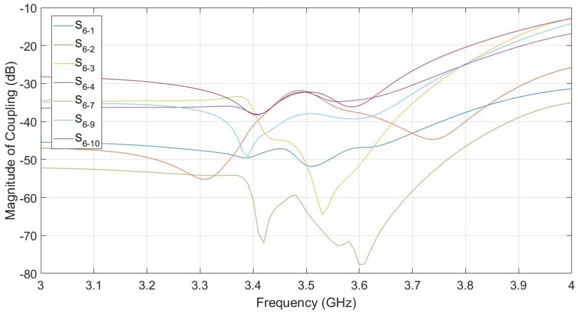

Figure 4.10: Coupling between a middle port with the adjacent ones.

The 3D radiation pattern for the four directions are shown in Fig. 4.11. It is obvious that the radiation pattern of each port is directed toward a different way, which means they are uncorrelated. The maximum realized gain is about 6 dB that is toward about 28 degrees in the elevation plane. Fig. 4.12 shows the 2D radiation pattern as a function of ϕ at the angle in elevation plane of maximum gain. The directions in azimuth angle of the four ports are (52,126,236,300). So, they seems to be uncorrelated in terms of space radiation pattern.

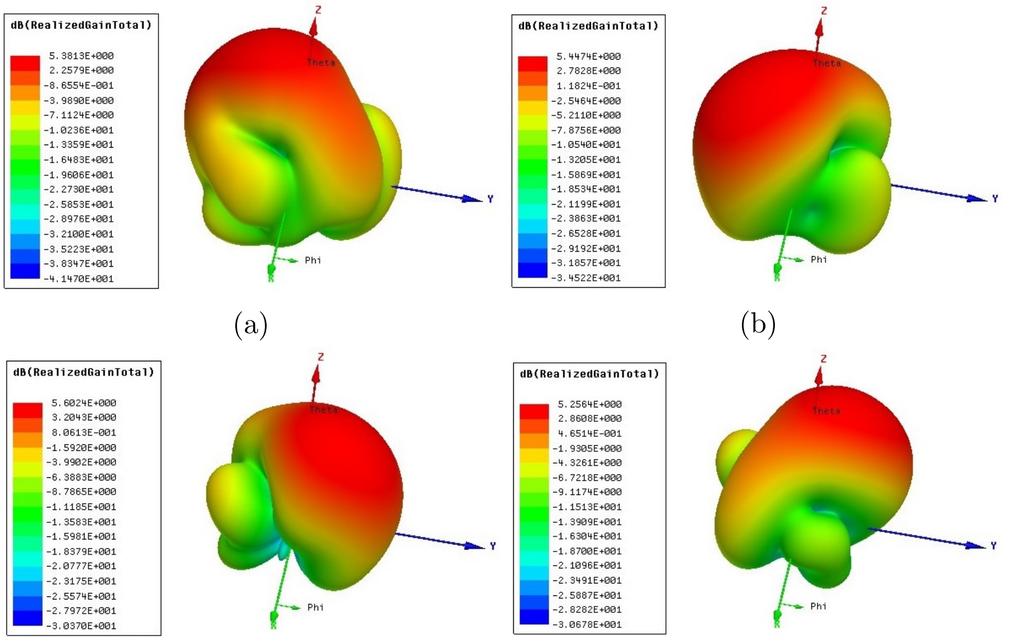

(a) (b)

(c) (d)

Figure 4.11: 3D realized gain radiation pattern for four basic port subarrays that is tilted towards θ=28^o and (a) ϕ=236^o, (b) ϕ=300^o, (c) ϕ=52^o and (d) ϕ=126^o.

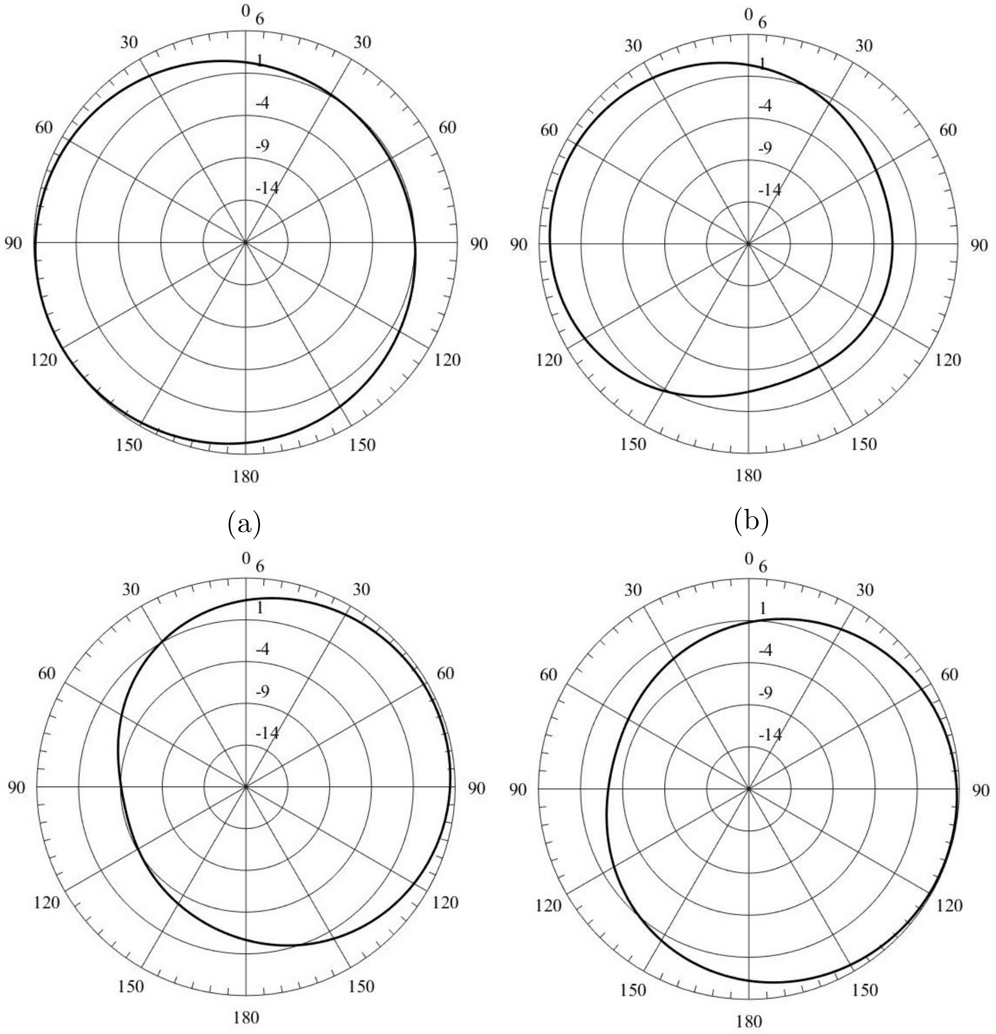

(a) (b)

(c) (d)

Figure 4.12: 2D radiation patterns at elevation angle θ=28^o of the beams that are tilted towards (a) ϕ=236^o, (b) ϕ=300^o, (c) ϕ=52^o and (d) ϕ=126^o.

The four ports with different beam tilt directions are distributed along the 16 ports panel in a way to avoid the correlation between them. Fig. 4.13 shows the distribution of the ports in terms of each 2D radiation pattern. The envelop correlation coefficient (ECC) is calculated between different ports using the space radiation pattern, and it is found not to exceed 0.095, which means that the ports are uncorrelated. The efficiency found by the software is 30.9%.

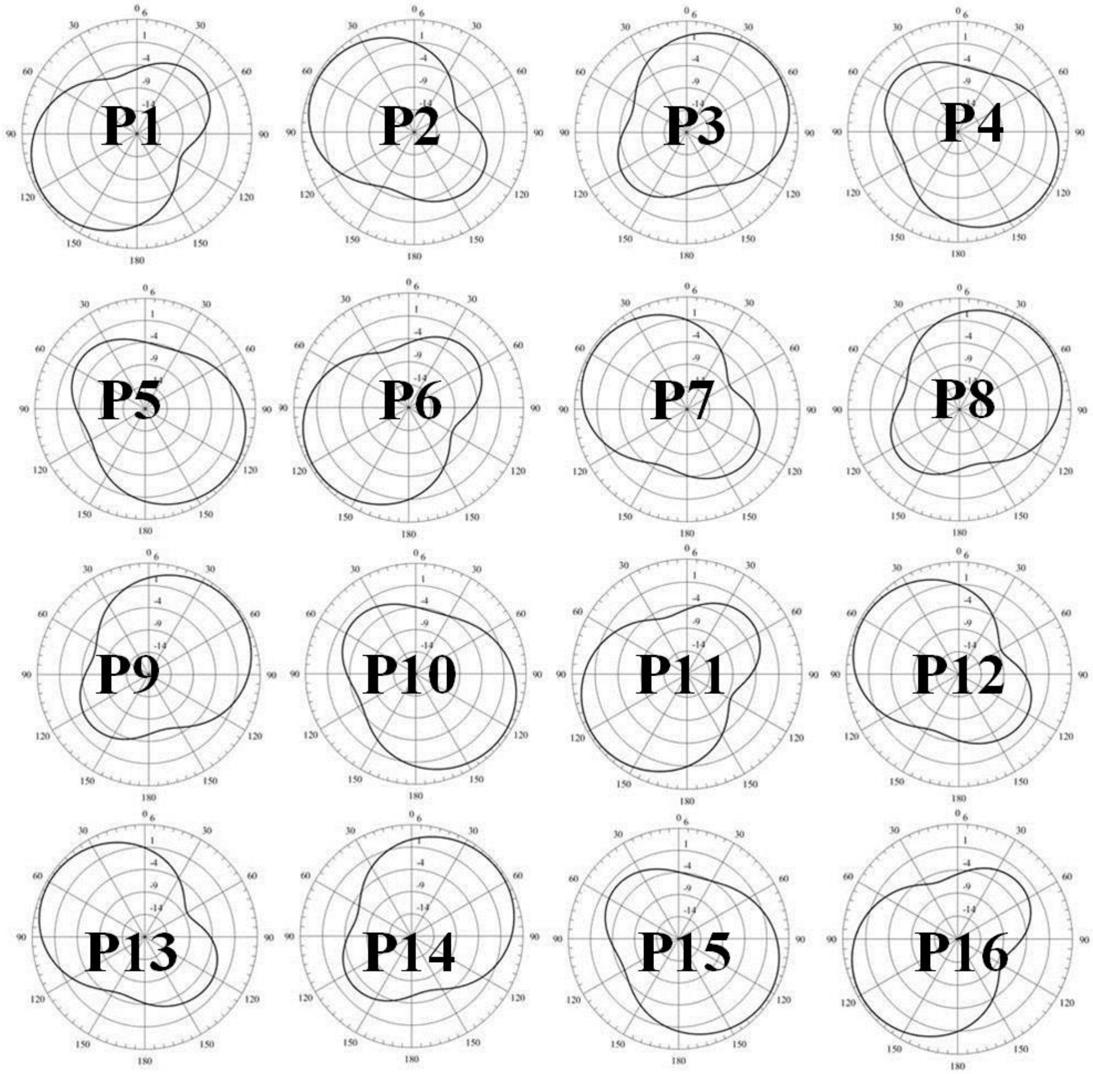

Figure 4.13: Port distribution along single panel in terms of 2D radiation pattern.

4.1.5 Design Summary

A design of single panel that consists of a 16 ports that may be used for mMIMO base station antenna systems is introduced. The design is based on a three layer PCB, which has the antenna elements (which are patches) on one side, and the feeding lines on the other side, with a ground layer in the middle. The procedure was to design the single port patches, then to find the proper excitation for each element to tilt the beam pattern of the port. Then the feeding network is designed to achieve the found excitations for feeding the patches. Then the single port (subarray of 4 antennas) is ready when we add the feeding lines as a new layer. This single port is redesigned to achieve different three ports with different angles of tilt, then these ports are distributed along the panel of 16 ports in a way to achieve uncorrelated patterns. The minimum bandwidth was 230 MHz with -25 dB maximum coupling between adjacent ports. The realized gain of each port (subarray) reaches to 6 dB with 30.9% efficiency, and the maximum ECC is found to be 0.095. This design has been presented in APCAP conference [37].

4.2 Design using FR4 material

To design any antenna model, it is important to consider all the practical details in the fabrication of the antenna into account with the simulation process. This section is a redesign of the 16 ports mMIMO antenna using FR4 material using CST and HFSS simulators with comparisons between their results.

4.2.1 Single port design

The design is based on subarray of 4 patches with each port that is designed at center frequency of 3.6 GHz. The total design is based on 3-layer structure. The top layer has the patches, the middle has the ground, and the bottom has the feeding network as shown in Fig. 4.14. The FR4 material has a 0.02 loss tangent, and with 0.8 mm hight of the board. The dielectric constant is 4.1. The feeding network for a single port is shown in Fig. 4.15 with the dimensions. The single port of the desired mMIMO system using the previous feeding network is shown as in Fig. 4.16.

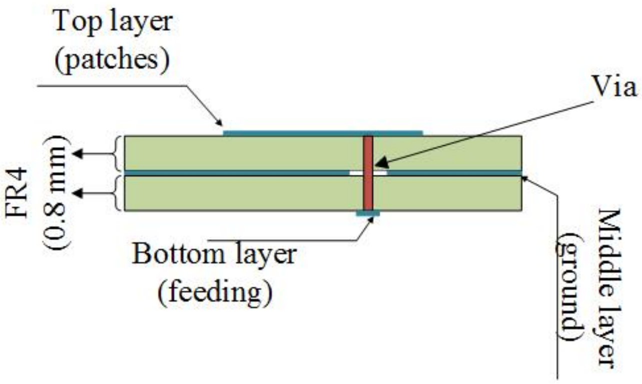

Figure 4.14: Stackup of three layer design.

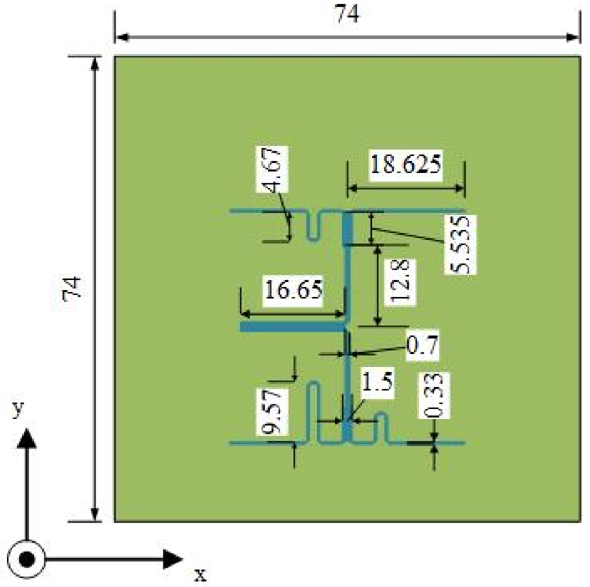

Figure 4.15: Feeding network for single port array (the dimensions are in mm).

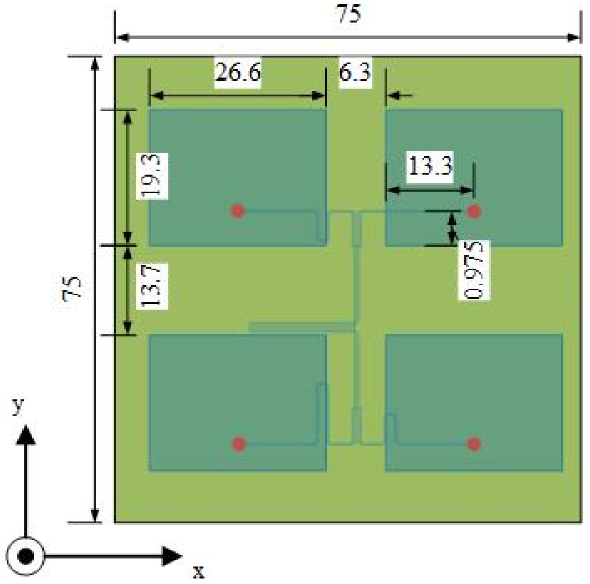

Figure 4.16: Layout of single port with dimensions (in mm).

The reflection coefficient is shown in Fig. 4.17. There is a difference between HFSS and CST simulators results, since different solving methods between them. The −10dB bandwidth is 450 MHz using HFSS simulator, and 396 using CST one. For the other three basic single port subarrays design with different beam tilts, the reflection coefficient are the same. The 3D realized gain for the single port design is shown in Fig. 4.18.

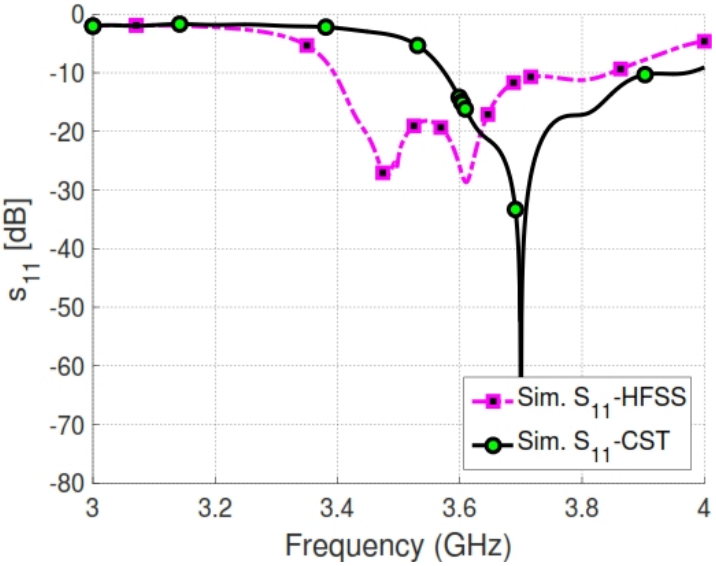

Figure 4.17: Reflection coefficient for single port array.

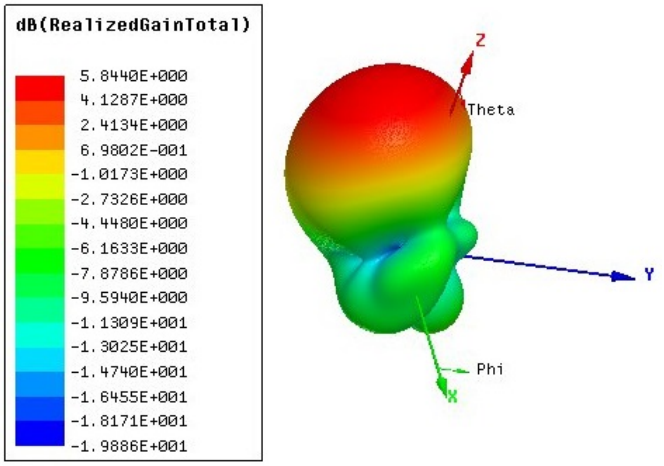

Figure 4.18: 3D realized gain radiation pattern for single port.

From Fig. 4.18, the radiation of the single ports is tilted toward a specific angle away from broadside direction. The maximum realized gain is about 5.84 dB that is toward the angle 25 degrees in the elevation plane.

4.2.2 16 ports mMIMO design

The final model of the design has 8×8 patches, which is a 4×4 mMIMO as shown in Fig. 4.19. The total size of the array is $30 \times 30 \times 0.16$ cm^3. The spacing between adjacent elements is 7.5 cm, which is equal to 0.9λ. Each port is located in the array beside adjacent ports that has different beam tilts to guarantee lower ECC.

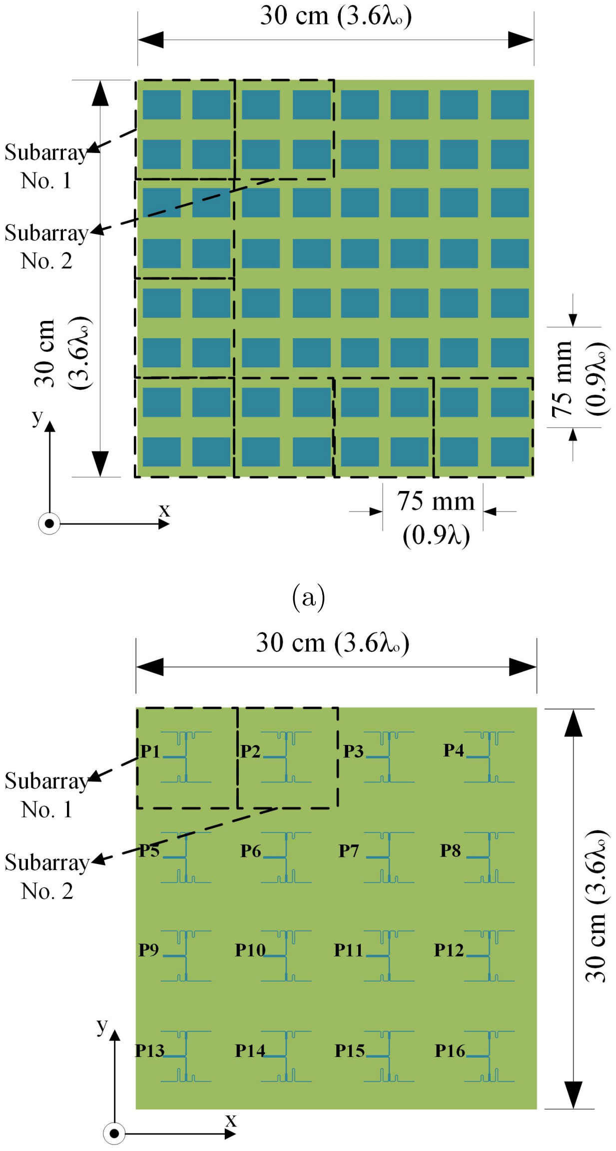

(a)

(b)

Figure 4.19: 16 port MIMO design.

Fig. 4.20 shows the 2D radiation pattern as a function of ϕ at the angle in elevation plane of maximum gain for each port of all 16 ports. The 2D pattern of each port is a function of ϕ that is taken at boresight direction of it.

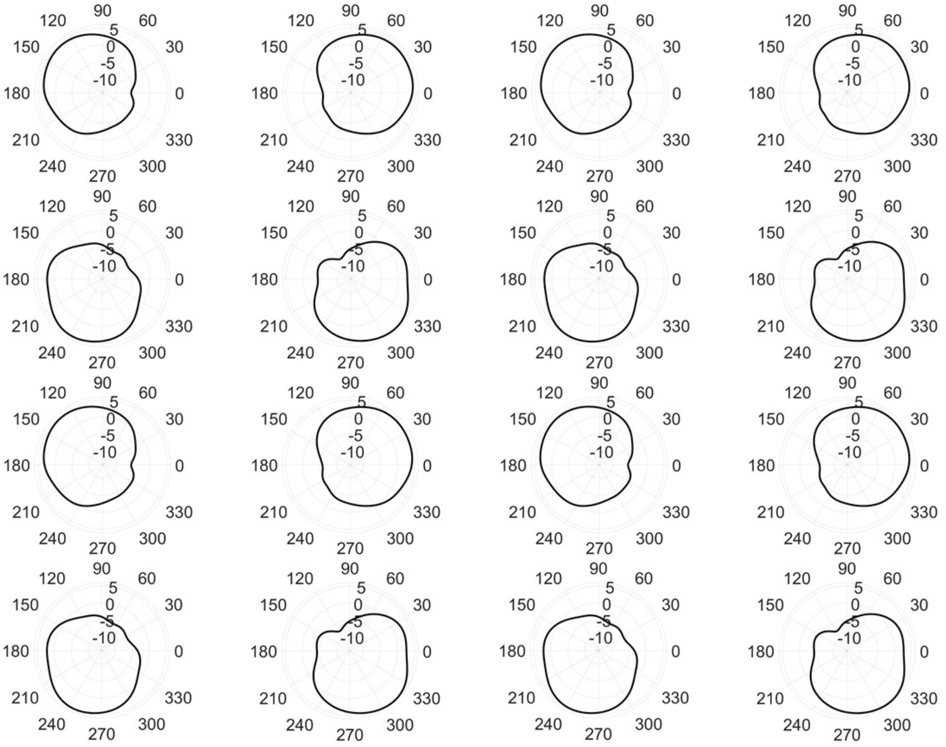

Figure 4.20: 2D radiation patterns at elevation angles θ=17^o-27^o of the beams of 16 ports design.

The whole design is simulated using CST and HFSS software packages and the S-parameters are shown in Figs. 4.21-4.24. The bandwidth is from 3.46-3.908 GHz by using HFSS, and from 3.555-3.932 GHz by using CST. The maximum coupling between ports (measured at a middle port, which is the sixth one) is -25 dB in the band of interest in CST, and -24 in HFSS. The maximum correlation coefficient found is equal to 0.0975, which means that the ports are almost uncorrelated.

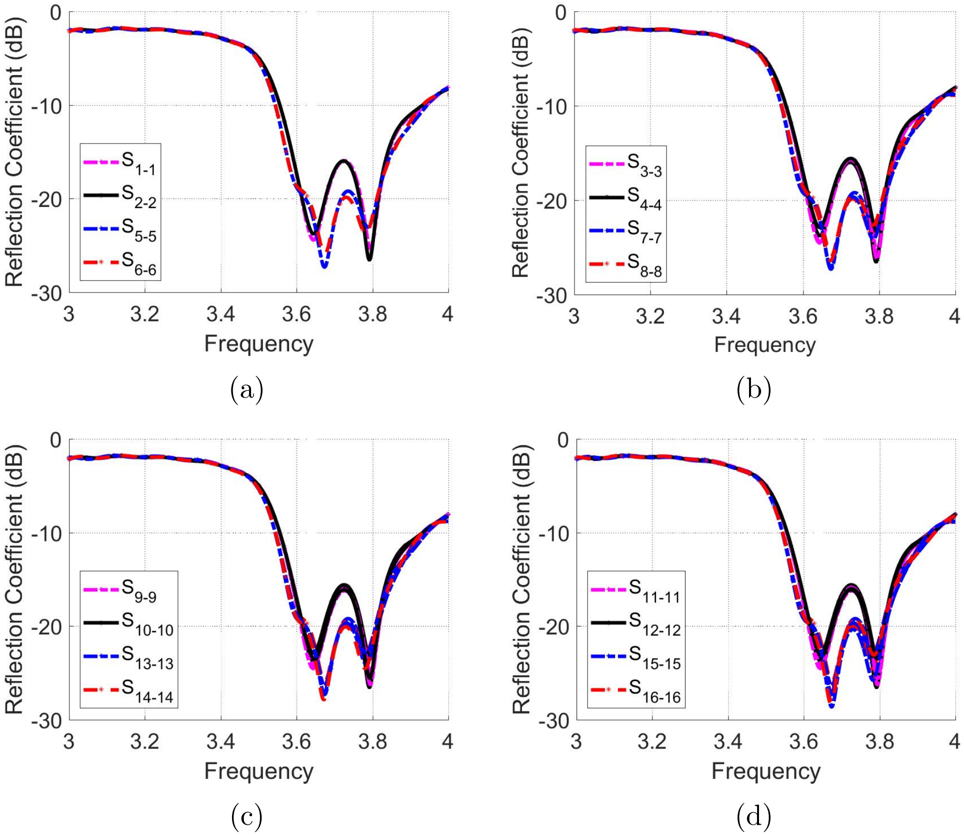

(a) (b)

(c) (d)

Figure 4.21: Reflection coefficient at all 16 ports using CST. (a) 1,2,5,6 ports, (b) 3,4,7,8 ports, (c) 9,10,13,14 ports and (d) 11,12,15,16 ports.

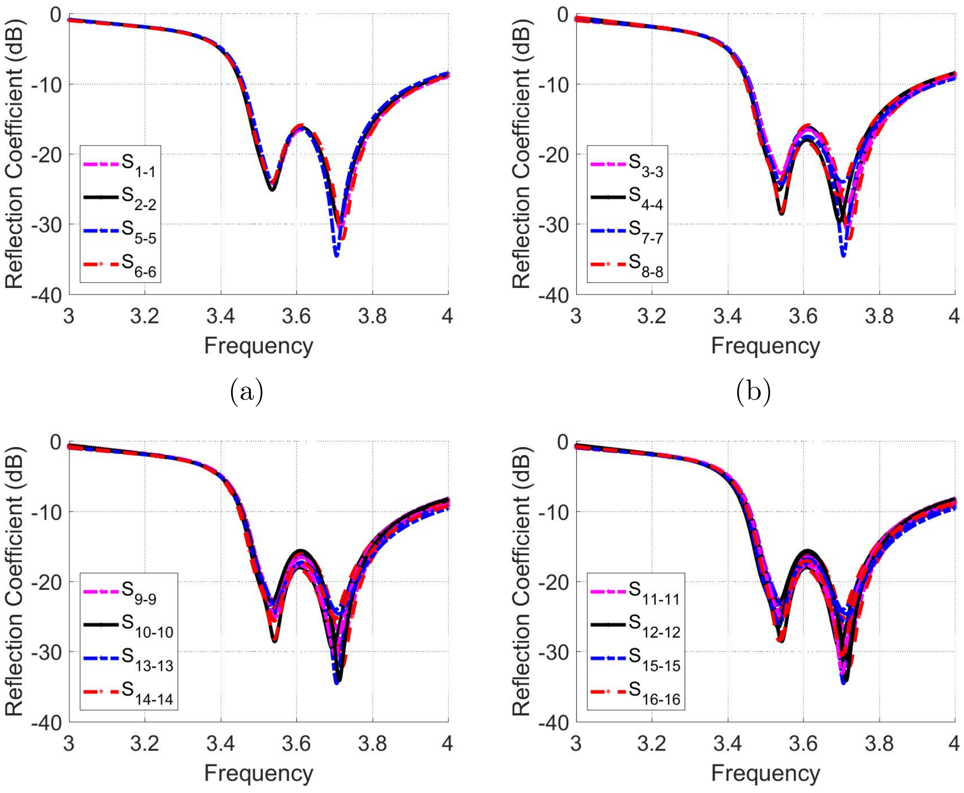

(a) (b)

(c) (d)

Figure 4.22: Reflection coefficient at all 16 ports using HFSS. (a) 1,2,5,6 ports, (b) 3,4,7,8 ports, (c) 9,10,13,14 ports and (d) 11,12,15,16 ports.

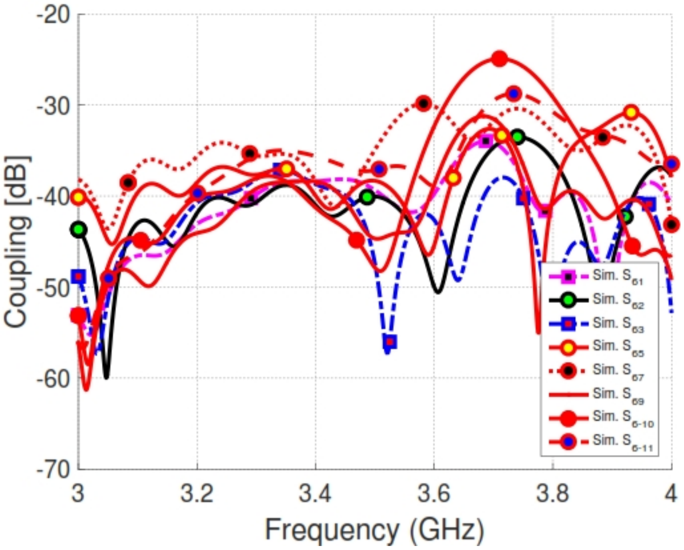

Figure 4.23: Coupling coefficient at port 6 with all adjacent ports using CST.

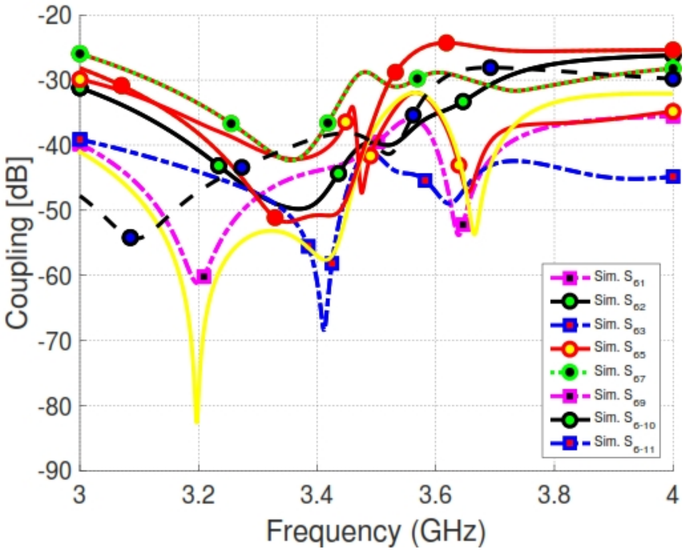

Figure 4.24: Coupling coefficient at port 6 with all adjacent ports using HFSS.

4.2.3 Summary

This section presents a 4×4 mMIMO system using FR4 material. It shows the simulation results of the array using both HFSS and CST softwares. To summarize the results and to compare them, Table 4.2 shows the comparison between them. It shows a good agreement between them with some differences due to different methods. The efficiency by each ports is very low since the material used has high tangent loss value.

Table 4.2: FR4 material design results with comparison between CST and HFSS simulators

Simulator	CST	HFSS
Covered Band (GHz)	3.555-3.932	3.46-3.91
Bandwidth (MHz)	377	450
Efficiency (%)	25.2-27.5	27.3-38.5
Realized Gain (dB)	2.05-3.03	4.46-5.65
Maximum Coupling (dB)	-25	-24

4.3 Design using ROGER material

Since using FR4 material results in an antenna with low efficiency, so we should have more efficient material with lower loss tangent value to achieve higher efficiency. This section presents an mMIMO antenna system design using RO4350 material.

4.3.1 Single port design

The same general idea of using a 2×2 patch subarray is utilized. The total design is based on also a 3-layer structure. The top layer is for patches, the middle for the ground, and the bottom one is for the feeding network as shown in Fig.4.25. The RO4350 material has a 0.002 loss tangent, and with 0.762 mm hight of the board. The dielectric constant is 3.5. The feeding network for a single port is shown in Fig. 4.26 with the dimensions. The single port on desired mMIMO system using the previous feeding network is shown as in Fig. 4.27.

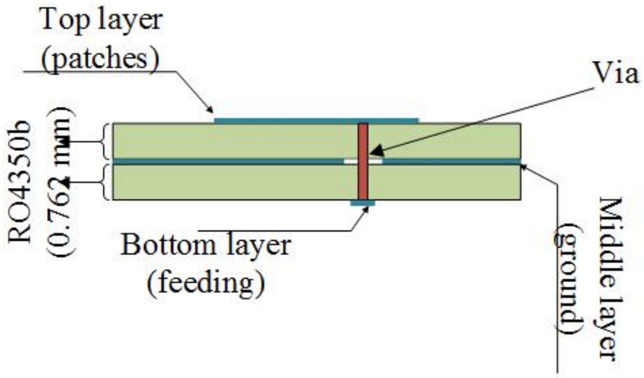

Figure 4.25: Stackup of three layer design.

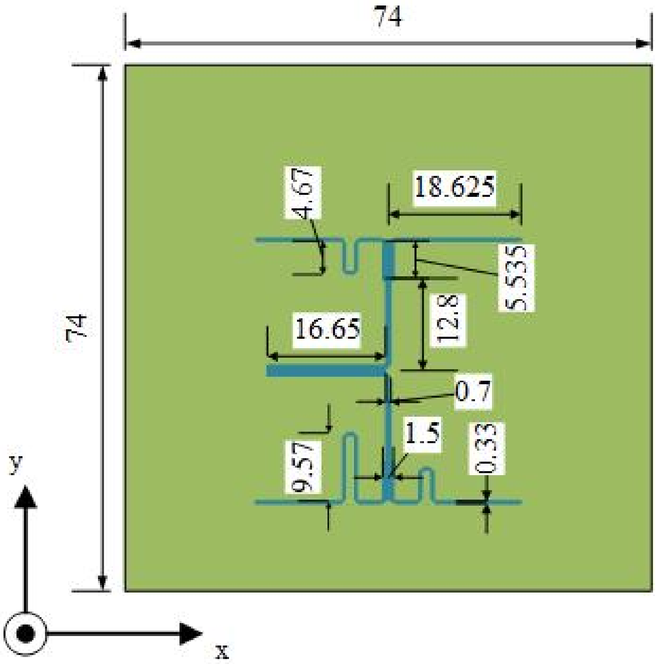

Figure 4.26: Feeding network for single port array (the dimensions are in mm).

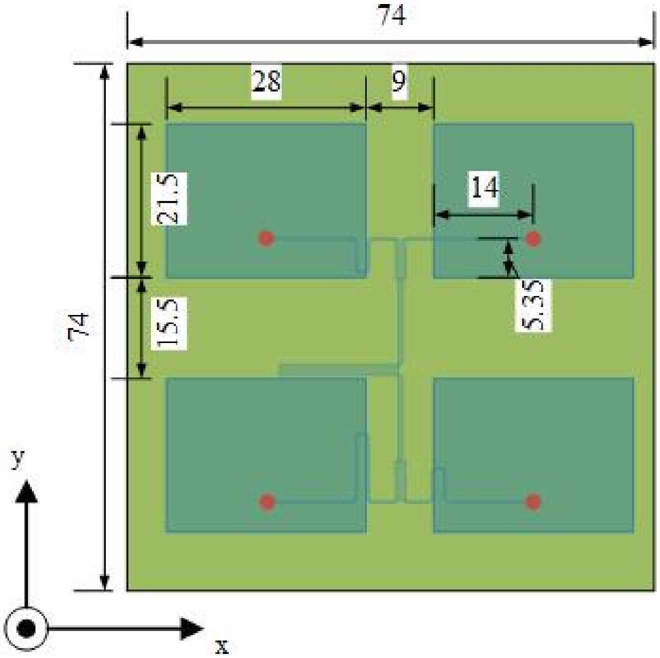

Figure 4.27: Layout of single port with dimensions (in mm).

This array is simulated to understand its performance. The reflection coefficient is as shown Fig. 4.28. The −10dB bandwidth is 120 MHz using HFSS, and 70 using CST. For the other directions, the reflection coefficients are the same as the one in Fig. 4.28. The 3D realized gain for the single port design is shown in Fig. 4.29. The radiation of the single ports is steered towards a tilted angle away from broadside direction. The maximum realized gain is about 7.78 dBi that is toward the angle 24 degrees in the elevation plane. Since each patch is fed on its linearly polarized edge, then the total subarray (single port) is linearly polarized.

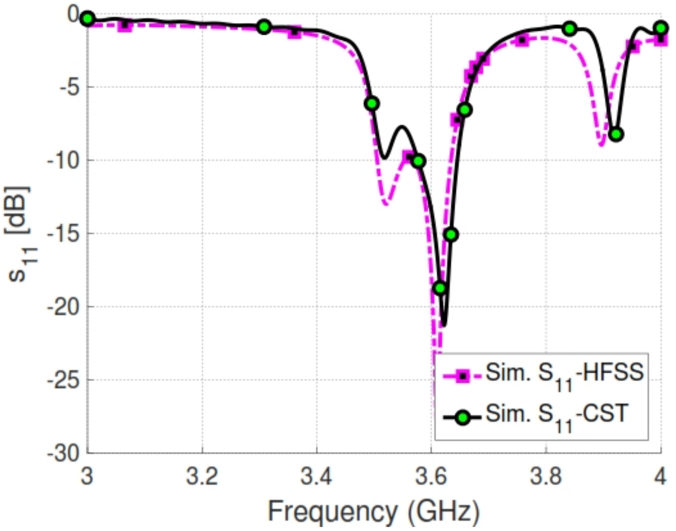

Figure 4.28: Reflection coefficient for single port array.

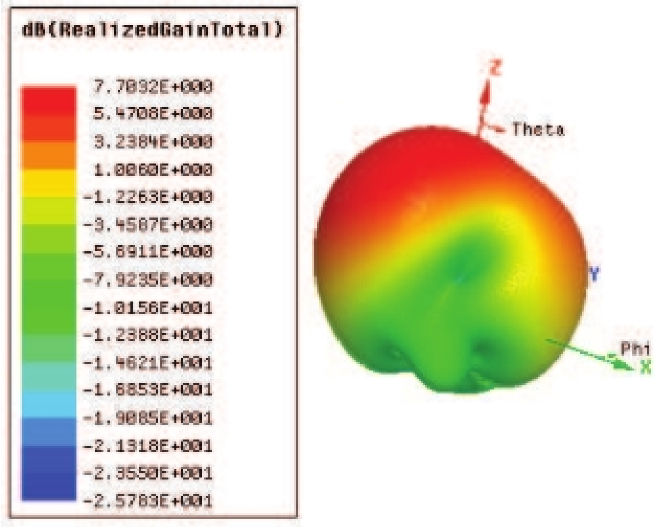

Figure 4.29: 3D realized gain radiation pattern for single port.

4.3.2 16 ports mMIMO design

The final model of the design is an 8×8 patches, 4×4 mMIMO is as shown in Fig. 4.30. Fig. 4.30(a) show the top layer of the 16 ports mMIMO system, where Fig. 4.30(b) shows the bottom layer. The size of the array is $29.6 \times 29.6 \times 0.1524$ cm^3, and the spacing between adjacent elements is 7.4 cm which represents $0.89\lambda_o$. Fig. 4.31 shows the 2D radiation pattern as a function of ϕ at the angle in elevation plane of maximum gain for each port of all 16 ports. Note that the distribution of the elements are is changed here comparing to that is used in FR4 material design. This is done to get the radiation of the edge elements are not tilted outward the total array itself, so the side lobe level (SLL) values are reduced when the system is operated in an array mode as will be discussed in Chapter 5.

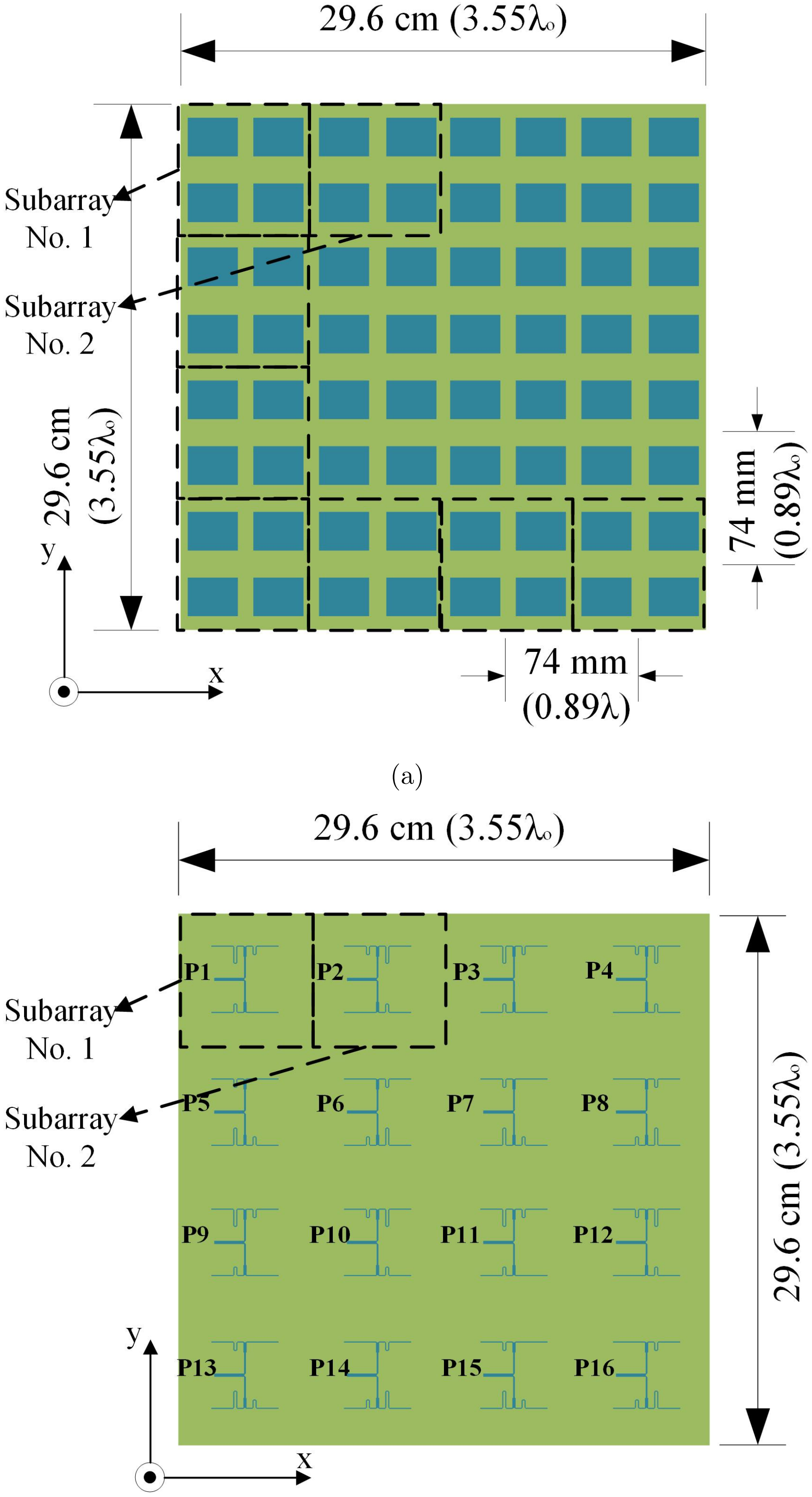

(a)

(b)

Figure 4.30: 16 port MIMO design.

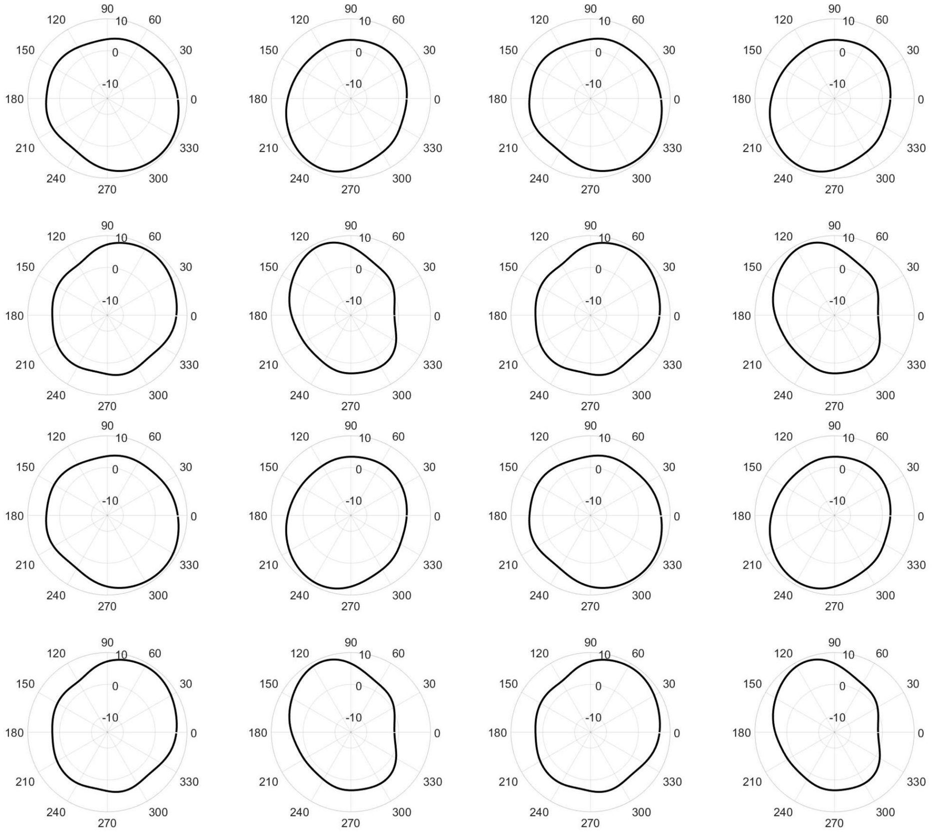

Figure 4.31: 2D radiation patterns at elevation angles θ=17^o-27^o of the beams of 16 ports design.

The design is simulated using CST and HFSS and the S-parameters are shown in Figures 4.32-4.35. In HFSS, just few selected ports are used to be defined to save RAM memory on the machine (1,2,5,6,7,10 ports), so the other ports at different connectors are not defined to save the complexity. The -10 dB bandwidth using HFSS is 123 MHz, where it is 145 MHz in CST. The maximum coupling between ports (measured at a middle port, which is the sixth one) is -15.9 dB in the band of interest in CST, and -17.5 in HFSS. The maximum correlation coefficient found is equal to 0.1198, which means that the ports are almost uncorrelated. The efficiency of a single port design is 74.5%.

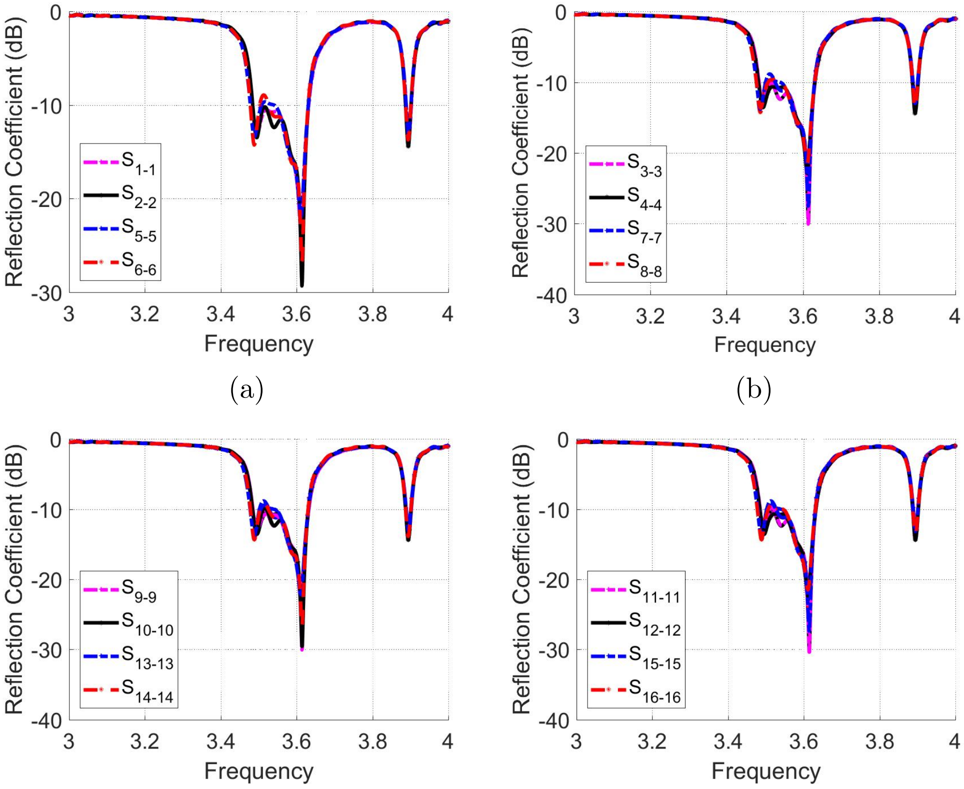

(a) (b)

(c) (d)

Figure 4.32: Reflection coefficient at all 16 ports using CST. (a) 1,3,9,11 ports, (b) 2,4,10,12 ports, (c) 5,7,13,15 ports and (d) 6,8,14,16 ports.

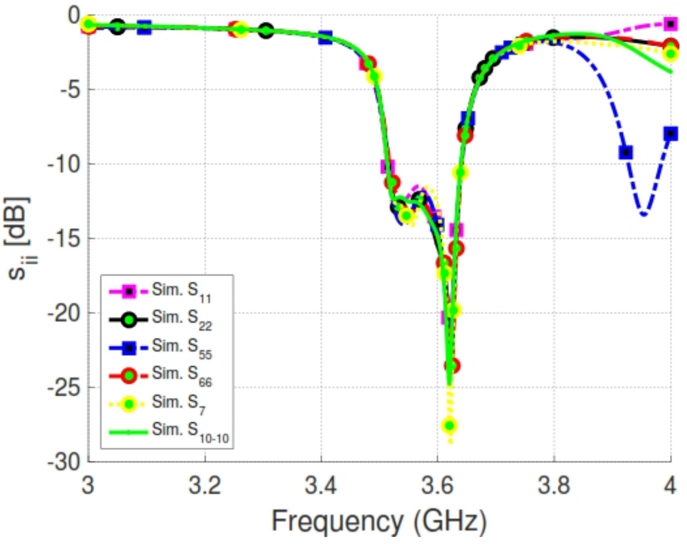

Figure 4.33: Reflection coefficient at al 16 ports using HFSS.

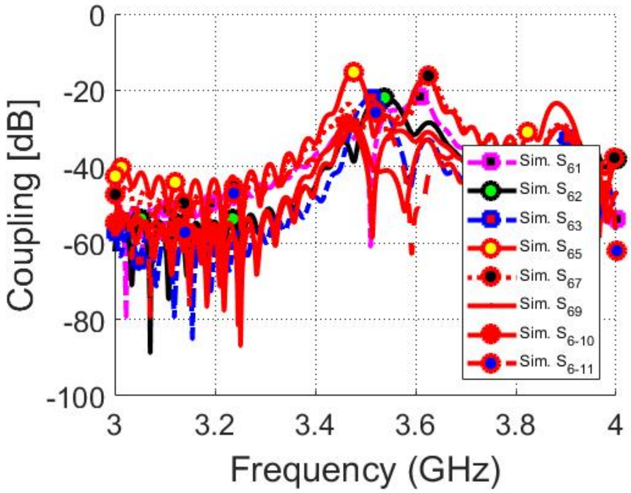

Figure 4.34: Coupling coefficient at port 6 with all adjacent ports using CST.

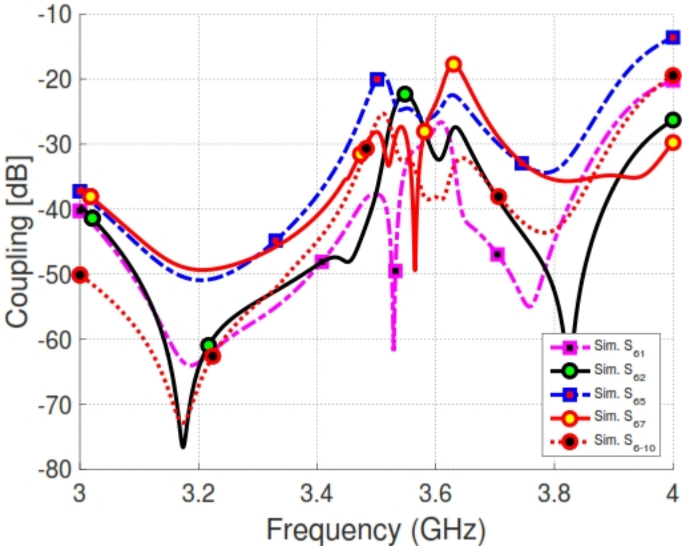

Figure 4.35: Coupling coefficient at port 6 with all adjacent ports using HFSS.

4.3.3 Summary

So far, a 4×4 mMIMO system is presented using RO4350b material. The results is shown by using both HFSS and CST softwares. To summarize the results and to compare them in the simulators, Table 4.3 shows the comparison between them.It shows a good agreement between them, with about 20 MHz difference in bandwidth. It shows a very good efficiency in both of them, and similar values of the gain.

Table 4.3: ROGER material design results with comparison between CST and HFSS simulators

Simulator	CST	HFSS
Covered Band (GHz)	3.485-3.63	3.517-3.64
Bandwidth (MHz)	145	123
Efficiency (%)	72.3-73.3	72.5-74.5
Realized Gain (dB)	8-8.5	7.9-9.5
Maximum Coupling (dB)	-15.9	-17.5

4.3.4 Comparison between using FR4 and ROGER materials

To summarize the results and to compare them in the two different materials, Table 4.4 shows the comparison between them. Using ROGER material helps to get more efficient design with higher gain. The efficiency is obviously improved from less than 40% in FR4 design to more than 70% in Rogers one. The bandwidth is decreased when using Rogers material, that is below 150 MHz, where it can reach 400 MHz using FR4 material. Also the maximum coupling between adjacent ports is higher in Rogers material, but still it can be accepted.

Table 4.4: Design results comparison between FR4 and RO4350b material substrates

Simulator	HFSS		CST	
Material	FR4	RO4350b	FR4	RO4350b
Covered Band (GHz)	3.46-3.91	3.517-3.64	3.555-3.932	3.485-3.63
Bandwidth (MHz)	450	123	377	145
Efficiency (%)	27.3-38.5	72.5-74.5	25.2-27.5	72.3-73.3
Realized Gain (dB)	4.46-5.65	7.9-9.5	2.05-3.03	8-8.5
Maximum Coupling (dB)	-24	-17	-25	-15.9

4.3.5 35 ports antenna design

The total array can be expanded to include more number of ports with the maximum allowable panel size as per base station specifications. This subsection is showing a 35 ports design using RO4350b material that is used in this section. The final model of the design is a 14×10 patches, which is 7×5 MIMO as shown in Fig. 4.36. Fig. 4.36(a) shows the top layer of the mMIMO system, where Fig. 4.36(b) show the bottom one. The total size of the panel is $37 \times 51.8 \times 0.1524$ cm^3.

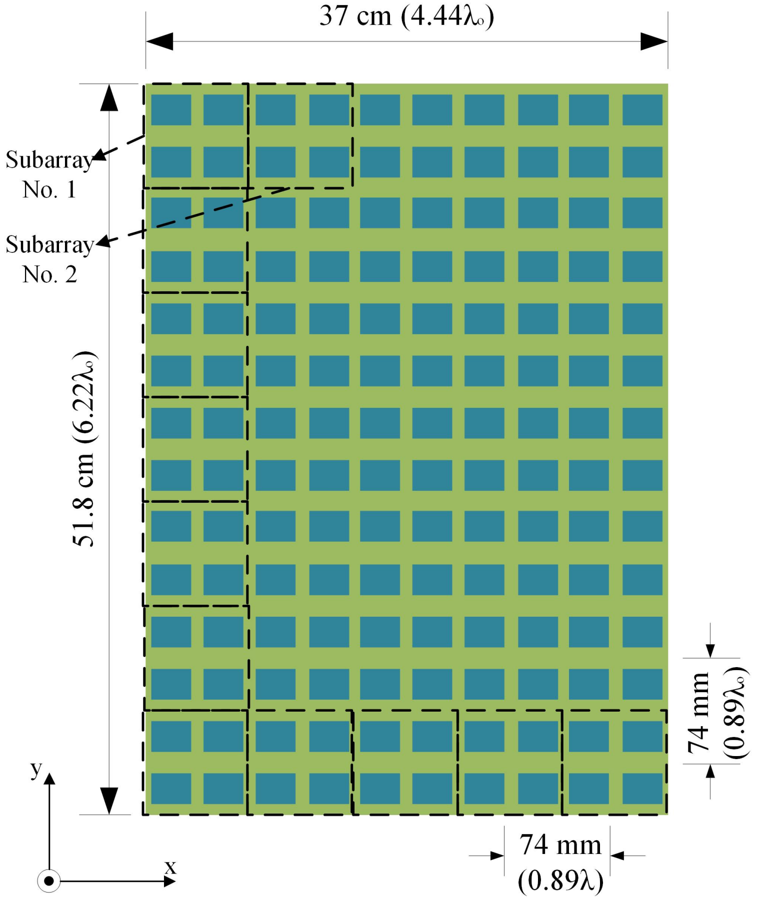

(a)

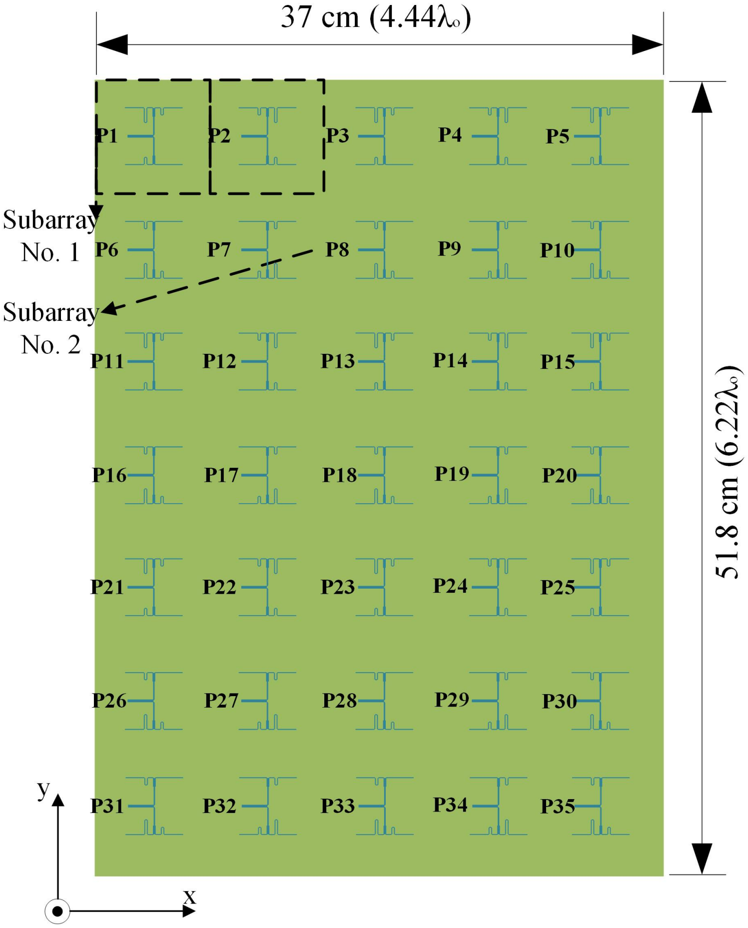

(b)

Figure 4.36: 35 port MIMO design.

4.4 24 ports antenna design

In fabrication process, many factors has been taken in consideration other than the design details itself, such as the size of offered board, fabrication cost and number of SMP connectors. For this reason, 24 ports is fabricated according to these limits. The designed array was simulated using CST studio suite and then it was fabricated and measured to check its performance. Port measurements were done using an Agilent Fieldfox N9928A VNA, while the radiation pattern were measured using a Satimo Starlab 18 GHz Anechoic chamber. The final model of the design is a 12×8 patches, which resembles a 6×4 mMIMO as shown in Fig. 4.37. Fig. 4.37(a) shows the top layer, and Fig. 4.37(b) shows the bottom one, where the total size is $29.6 \times 44.4 \times 0.1524$ cm^3.

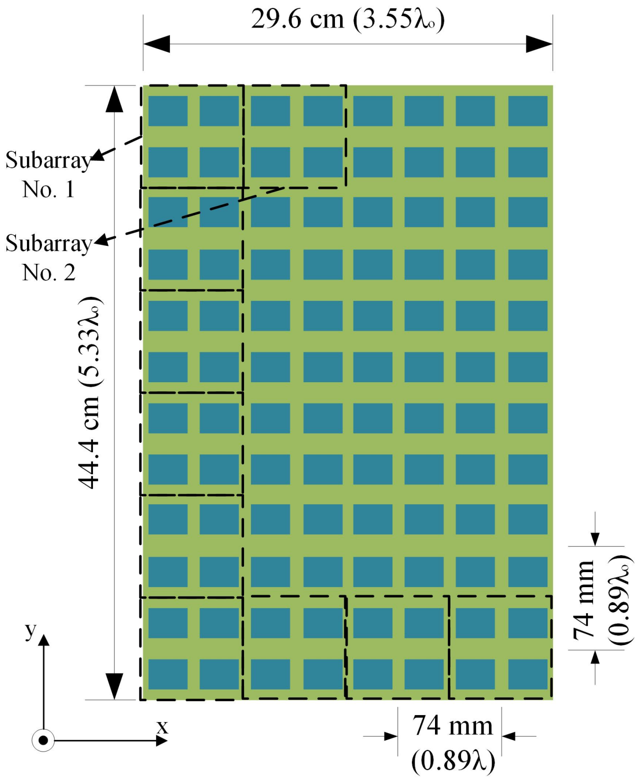

(a)

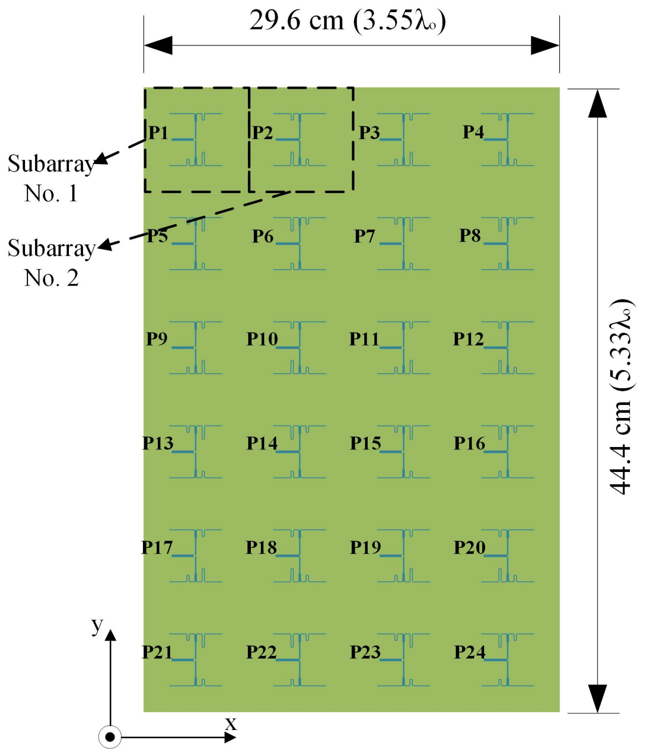

(b)

Figure 4.37: 24 port MIMO design.

The complete base station mMIMO antenna system consists of three boards like the board in Fig. 4.37. So, the total number of ports will be 72 ports, with 288 patches. Fig. 4.38 shows the proposed triangular base station mMIMO antenna with 72 ports, with 288 patch antenna elements. Fig. 4.41 shows the 2D radiation pattern as a function of ϕ at the angle in elevation plane of maximum gain for each port of all 24 ports.

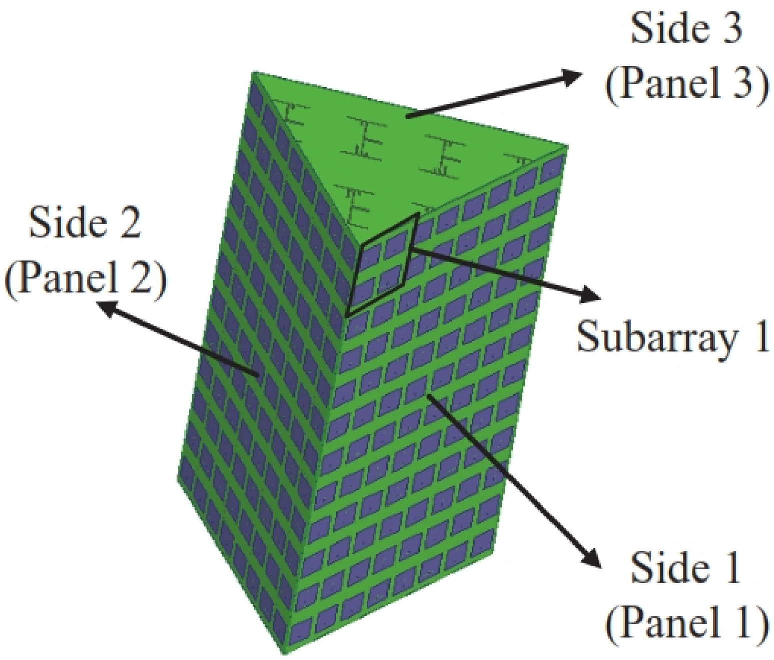

Figure 4.38: Diagram of 72 ports mMIMO base station system.

The three boards have been fabricated and measured using an Agilent Fieldfox N9928A VNA. Fig. 4.39(a) shows the bottom side of the fabricated design, and Fig. 4.39(b) show the top side. Fig. 4.40 shows the port measurement setup for measuring the S-parameters.

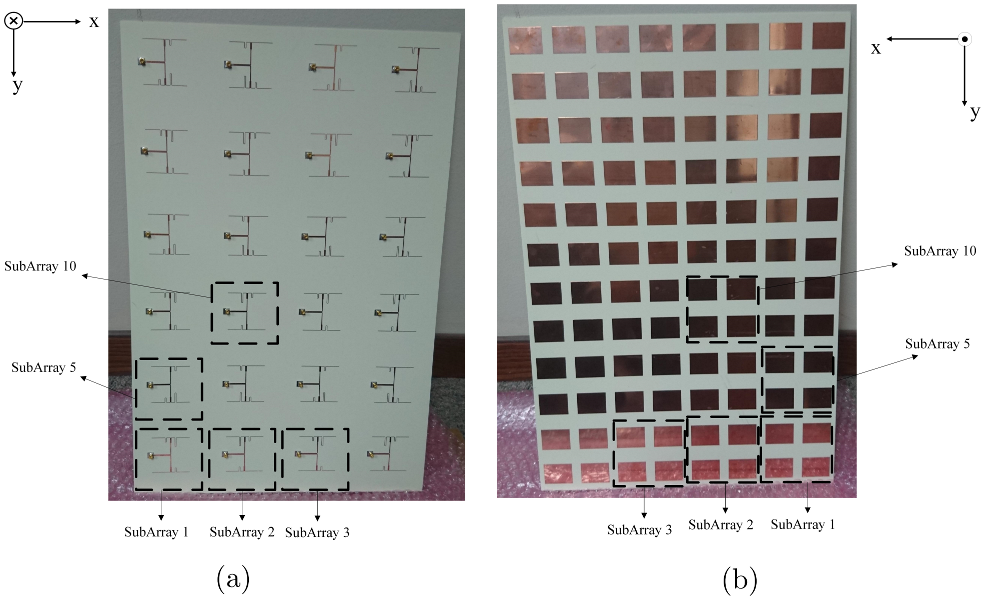

Figure 4.39: Fabricated 24 port MIMO design. (a) Bottom side. (b) Top side.

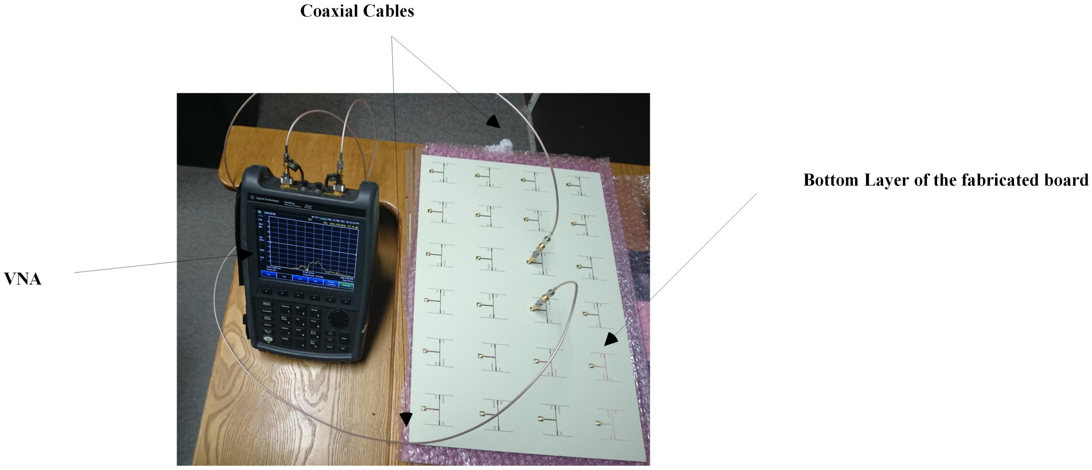

Figure 4.40: Measurement setup of 24 ports design board.

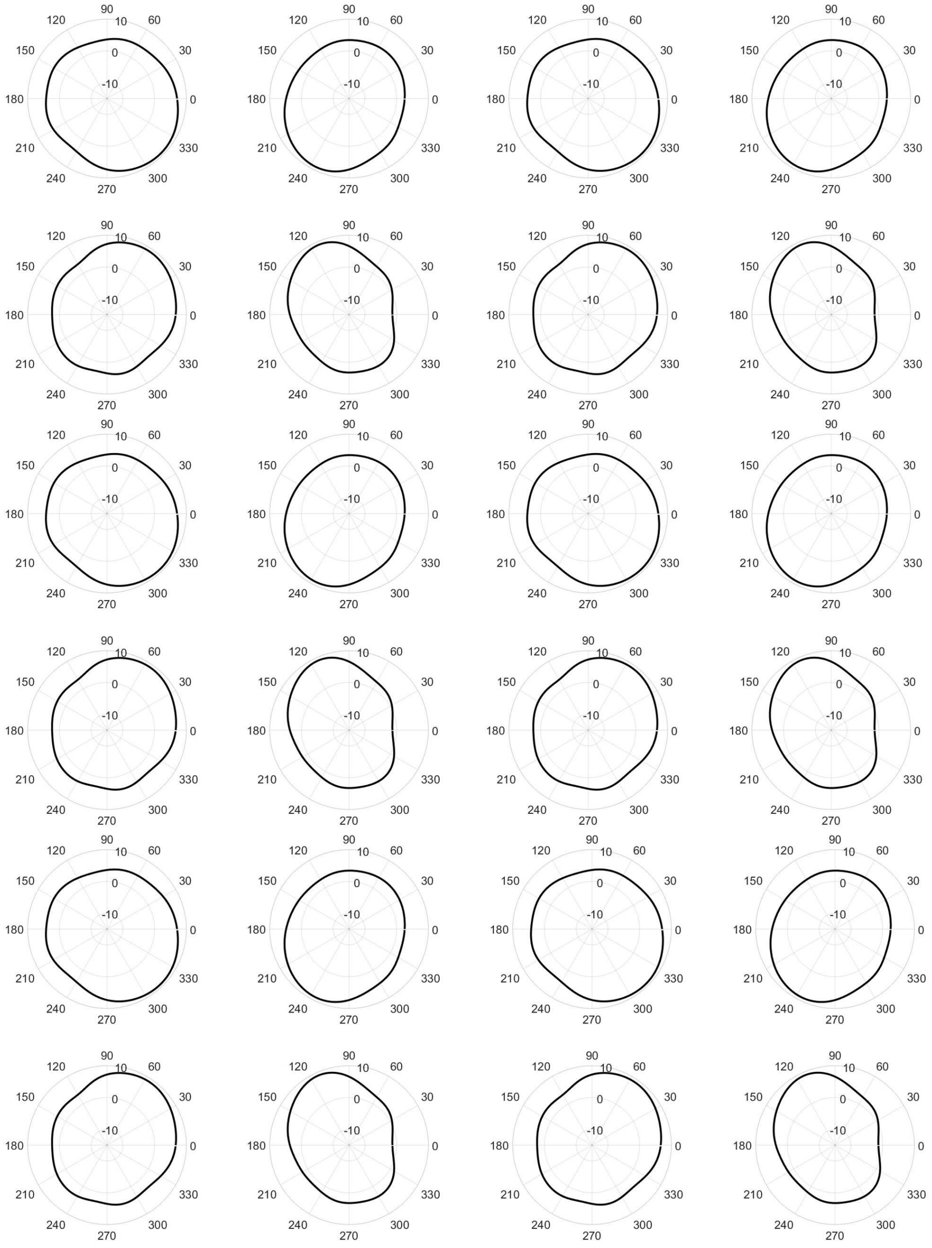

Figure 4.41: 2D radiation patterns at elevation angles θ=17^o-27^o of the beams of 24 ports design.

The measured and simulated S-parameters are shown in Figs. 4.42,4.43. The band supported by this array is 3.45-3.55 GHz, which gives 100 MHz bandwidth. The maximum coupling between ports is -14.8 dB in the band of interest. The efficiency of a single port is 74.5%. The maximum ECC that is calculated between the sixth subarray and the adjacent subarrays is equal to 0.1198, which means that the ports can achieve good MIMO performance. The realized gain by each port is found to be between 8-8.5 dB for different subarrays. The radiation pattern is measured by Satimo Starlab 18 GHz Anechoic chamber as shown in measurement setup in Fig. 4.44. It shows a good agreement between the simulations and measurements as shown in Fig. 4.45 for port 10. The measure gain equals to 7.99 dBi.

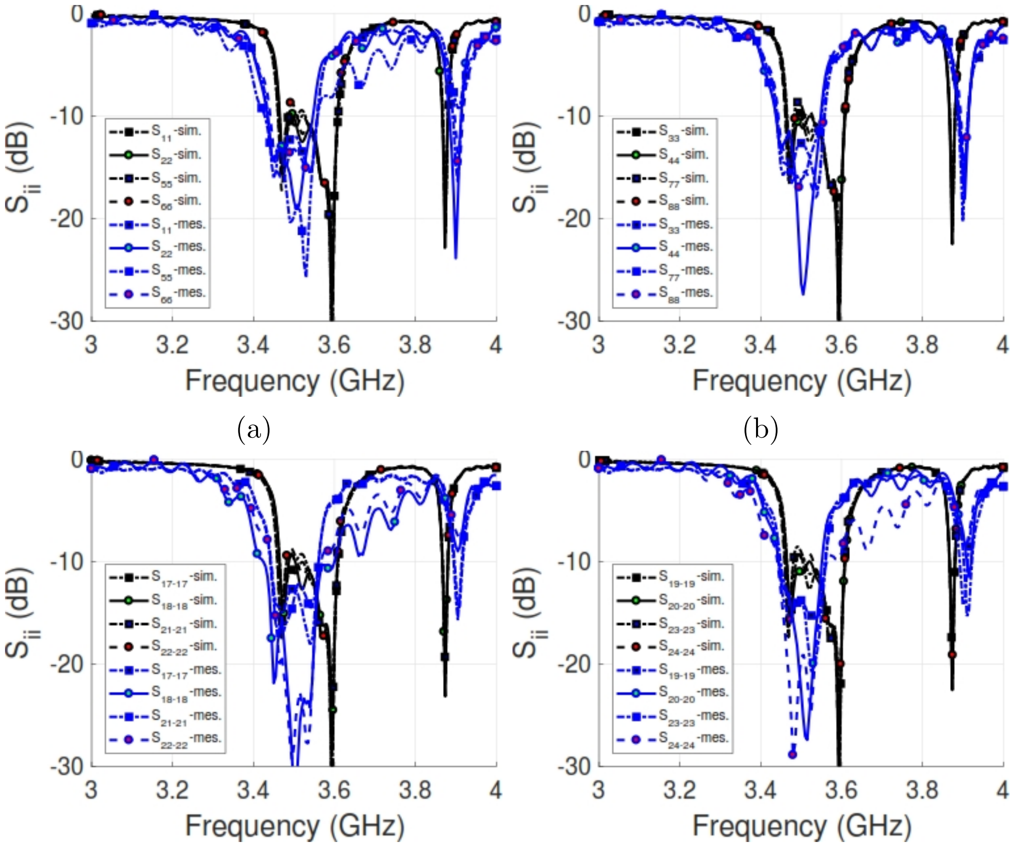

(a) (b)

(c) (d)

Figure 4.42: Reflection coefficient at all 24 ports. (a) 1,2,5,6 ports, (b) 3,4,7,8 ports, (c) 17,18,21,22 ports and (d) 19,20,23,24 ports.

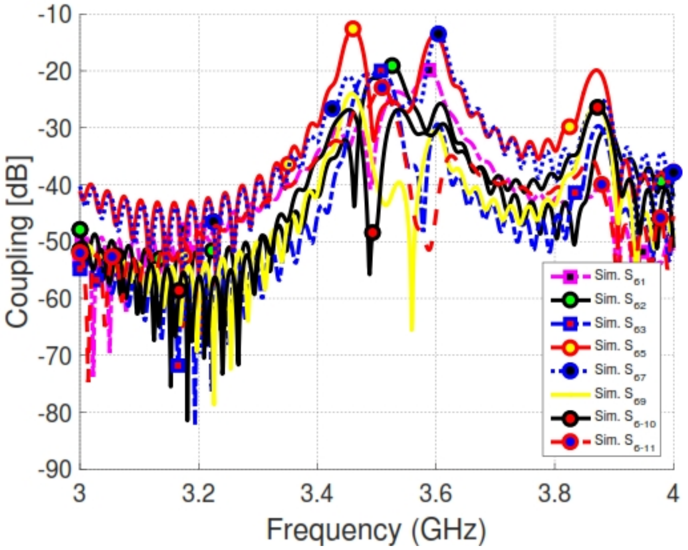

Figure 4.43: Coupling coefficient at port 6 with all adjacent ports.

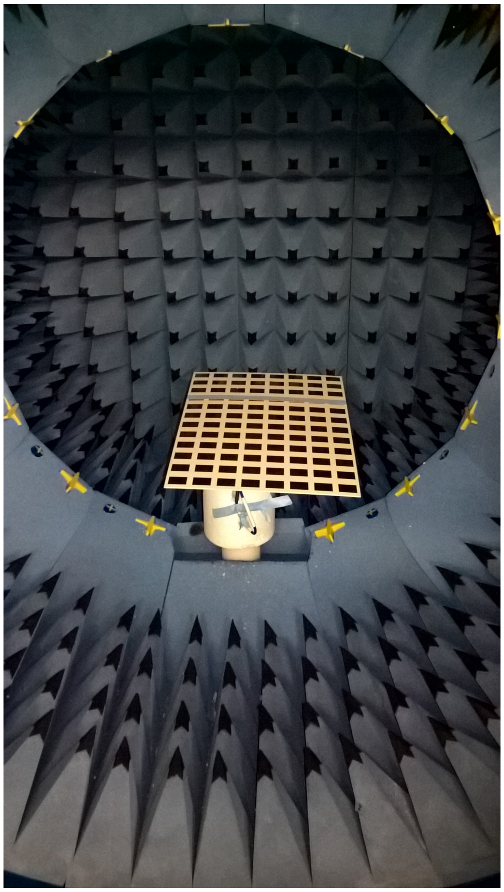

Figure 4.44: Radiation pattern measurement setup by Satimo Starlab Chamber.

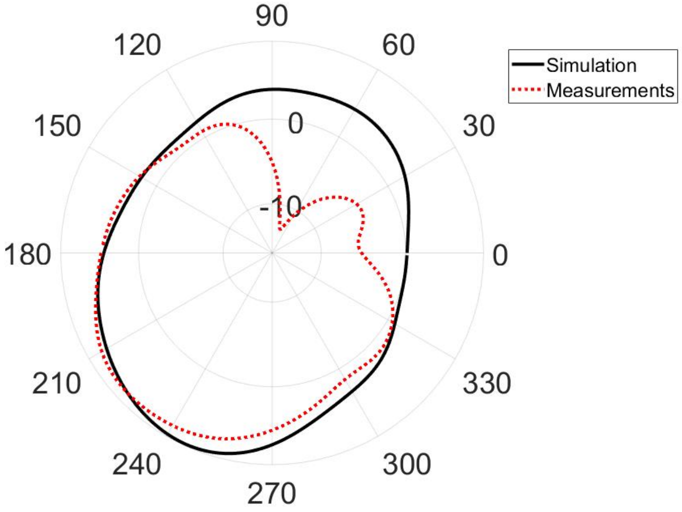

Figure 4.45: 2D radiation pattern measured and simulated at port 10 on the boresight angle.

Comparing the measurement and simulation results is shown in Table 4.5. There is a slight mismatch in terms of bandwidth. This mismatch comes from that the SMP model used in simulations was ARF1596-ND, where the fabrication company used PE44489 model, which has smaller size that made a problem in soldering at the fabricated board.

Table 4.5: Results comparison between Measurement and CST outcomes

Simulator	CST	Measurements
Covered Band (GHz)	3.485-3.63	3.45-3.55
Bandwidth (MHz)	145	100
Efficiency (%)	72.3-73.3	64
Gain (dBi)	8-8.5	9.4
Maximum Coupling (dB)	-15.9	-14.8

CHAPTER 5

BEAMSTEERING ALGORITHM

In antenna array structures, the pattern for the overall array is the summation of the patterns of each element. If the elements in the array are identical, the total pattern can be found by using pattern multiplication principle as follows [36]:

$$E_t = E_o.AF \tag{5.1}$$

where E_t is the total pattern (electrical field) of the array, E_o is the pattern of single element and AF is the array factor of the array. This chapter discusses the radiation response assuming nonidentical elements, and provides a beam switching method for the proposed mMIMO array in Chapter 4.

5.1 Array factor for planar arrays

The array factor represents the behavior of the array according to antennas distribution and the excitation of each element. For the linear array, the array factor is written as [36]:

$$AF = \sum_{m=1}^{M} I_m e^{j(m-1)\psi} \tag{5.2}$$

where I_m is the amplitude excitation at mth element, and:

$$\psi = kdu + \beta \tag{5.3}$$

where β is the progressive phase excitation, and:

$$k = \frac{2\pi}{\lambda} \tag{5.4}$$

$$\begin{aligned} u &= sin\theta cos\phi \qquad elementalong\, x - axis \\ &= sin\theta sin\phi \qquad elementsalong\, y - axis \\ &= cos\theta \qquad elementsalong\, z - axis \end{aligned} \tag{5.5}$$

Assuming that the antenna elements of array are distributed along xy-plane, then the array factor can be written as:

$$AF = AF_x AF_y \tag{5.6}$$

where AF_x and AF_y are the array factor for a linear array along x-axis and y axis, respectively. By extracting the equations, the array factor becomes as:

$$AF = \sum_{n=1}^{N} I_{1n} (\sum_{m=1}^{M} I_{m1} e^{j(m-1)\psi_x}) e^{j(n-1)\psi_y} \tag{5.7}$$

where M and N are the number of elements along x and y axes, respectively, and,

$$\begin{aligned} \psi_x &= kd_x sin\theta cos\phi + \beta_x \\ \psi_y &= kd_y sin\theta sin\phi + \beta_y \end{aligned} \tag{5.8}$$

where d_x and d_y are the spacing between elements along x and y directions, respectively. β_x and β_y are progressive phase excitations along x and y directions, respectively. For an example, the array factor for 2×2 elements is given as:

$$AF = I_{11} + I_{12} e^{j\psi_x} + I_{21} e^{j\psi_y} + I_{22} e^{j(\psi_x + \psi_y)} \tag{5.9}$$

where I_{mn} represents the amplitude excitation of the element mn, and the exponent is phase excitation at that element.

Assuming that the array elements are not identical, then the pattern multiplication principle cannot be applied. Here is an investigation of pattern of an array using the array factor calculation in previous equations.

Assume a 2×2 different elements array over xy-plane, the exact pattern of this array is given as following:

$$E_{t_4} = E_{11} + E_{12} + E_{21} + E_{22} \tag{5.10}$$

where E_{mn} is the pattern of mnth element. If the pattern of each single port is given at the origin individually, then the space factor for the whole array can be applied as:

$$E_{t_4} = I_{11}E_{11} + I_{12}e^{j\psi_x}E_{12} + I_{21}e^{j\psi_y}E_{21} + I_{22}e^{j(\psi_x+\psi_y)}E_{22} \tag{5.11}$$

Assume a 2×2 array as shown in Fig. 5.1. Applying Eq. (5.11) to the proposed design and comparing results with the simulated one is shown in Fig. 5.2. (The amplitude excitation is assumed 1 for all elements, and β=0). The HPBW using the algorithm is about 30^o, where it is about 27^o by simulation. The SLL is 8.68 dB using the algorithm, and 8.18 dB by simulation.

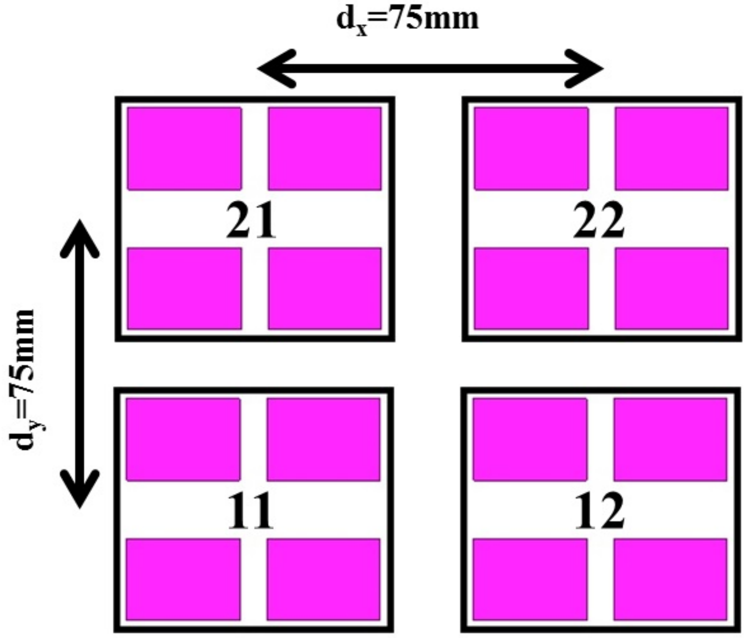

Figure 5.1: 2×2 antenna array example, each element insists of 2×2 patches with different pattern.

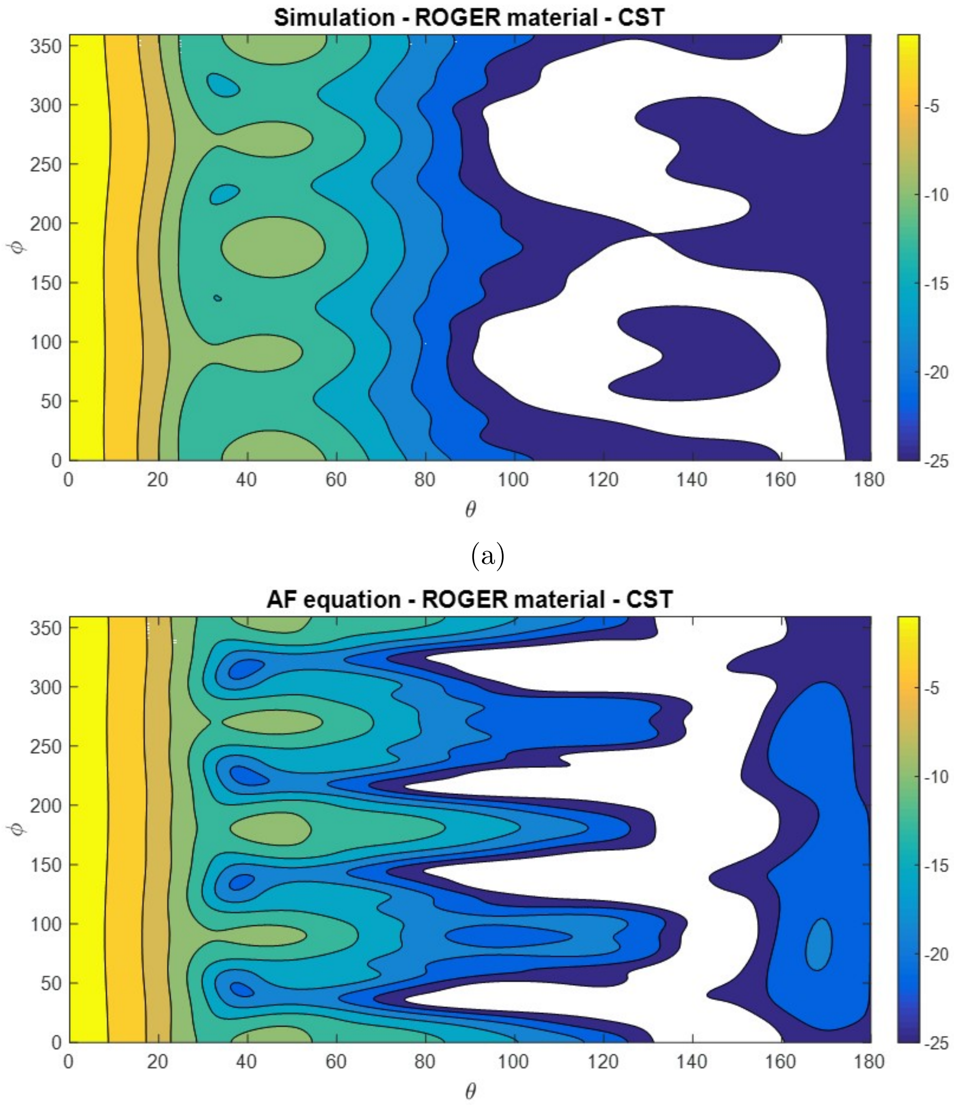

(a)

(b)

Figure 5.2: (a) Simulated normalized pattern for 4 antenna elements using CST simulator. (b) Normalized pattern of 4 antennas using equ. (5.11) based on the single port patterns of CST simulation results.

In Fig. 5.2, the pattern has a broadside behavior(maximum point of the pattern is located at $\theta = 0$) with high side lobes. These side lobes appear because the spacing between the elements is higher than $\lambda/2$ and each element has a pattern with different directed beam (different maximum locations). The pattern that is resulted using equ. (5.11) shows side lobes at shifted locations from the simulated one since it is approximated formula.

5.2 Beamsteering Algorithm for the Proposed Design

For the designed mMIMO antenna system, the antennas are distributed along the whole array as shown in Fig. 5.3.

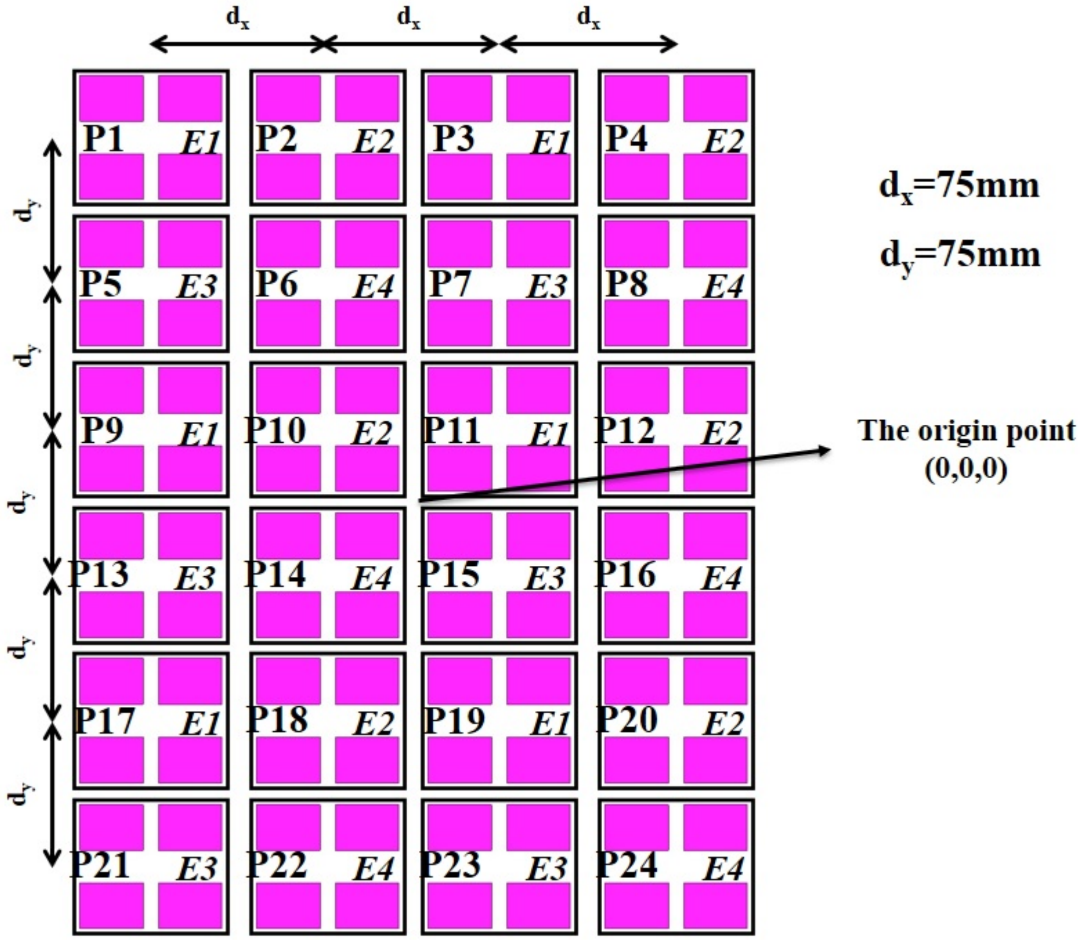

Figure 5.3: 6 × 4 antenna array example.

In this case, the total pattern of the whole array, where the single port pattern is given, can be written row-by-row as:

$$
\begin{aligned}
E_{t_{24}} = {} & I_1 e^{j(-3\psi_x/2+5\psi_y/2+\beta_1)}E_1 + I_2 e^{j(-\psi_x/2+5\psi_y/2+\beta_2)}E_2 + I_3 e^{j(\psi_x/2+5\psi_y/2+\beta_3)}E_1 \\
& + I_4 e^{j(3\psi_x/2+5\psi_y/2+\beta_4)}E_2 \\
& + I_5 e^{j(-3\psi_x/2+3\psi_y/2+\beta_5)}E_3 + I_6 e^{j(-\psi_x/2+3\psi_y/2+\beta_6)}E_4 + I_7 e^{j(\psi_x/2+3\psi_y/2+\beta_7)}E_3 \\
& + I_8 e^{j(3\psi_x/2+3\psi_y/2+\beta_8)}E_4 \\
& + I_9 e^{j(-3\psi_x/2+\psi_y/2+\beta_9)}E_1 + I_{10} e^{j(-\psi_x/2+\psi_y/2+\beta_{10})}E_2 + I_{11} e^{j(\psi_x/2+\psi_y/2+\beta_{11})}E_1 \\
& + I_{12} e^{j(3\psi_x/2+\psi_y/2+\beta_{12})}E_2 \\
& + I_{13} e^{j(-3\psi_x/2-\psi_y/2+\beta_{13})}E_3 + I_{14} e^{j(-\psi_x/2-\psi_y/2+\beta_{14})}E_4 + I_{15} e^{j(\psi_x/2-\psi_y/2+\beta_{15})}E_3 \\
& + I_{16} e^{j(3\psi_x/2-\psi_y/2+\beta_{16})}E_4 \\
& + I_{17} e^{j(-3\psi_x/2-3\psi_y/2+\beta_{17})}E_1 + I_{18} e^{j(-\psi_x/2-3\psi_y/2+\beta_{18})}E_2 + I_{19} e^{j(\psi_x/2-3\psi_y/2+\beta_{19})}E_1 \\
& + I_{20} e^{j(3\psi_x/2-3\psi_y/2+\beta_{20})}E_2 \\
& + I_{21} e^{j(-3\psi_x/2-5\psi_y/2+\beta_{21})}E_3 + I_{22} e^{j(-\psi_x/2-5\psi_y/2+\beta_{22})}E_4 + I_{23} e^{j(\psi_x/2-5\psi_y/2+\beta_{23})}E_3 \\
& + I_{24} e^{j(3\psi_x/2-5\psi_y/2+\beta_{24})}E_4
\end{aligned}
\tag{5.12}
$$

And it can be in more compact form as following:

$$
\begin{aligned}
E_{tot} = \sum_{m=1}^{2}\sum_{n=1}^{3} \\
& I_{(2m-1)(2n-1)} \exp^{j\{(4m-7)\frac{\psi_x}{2}+(4n-9)\frac{\psi_y}{2}+\beta_{(2m-1)(2n-1)}\}} E_1 \\
& + I_{(2m)(2n-1)} \exp^{j\{(4m-5)\frac{\psi_x}{2}+(4n-9)\frac{\psi_y}{2}+\beta_{(2m)(2n-1)}\}} E_2 \\
& + I_{(2m-1)(2n)} \exp^{j\{(4m-7)\frac{\psi_x}{2}+(4n-7)\frac{\psi_y}{2}+\beta_{(2m-1)(2n)}\}} E_3 \\
& + I_{(2m)(2n)} \exp^{j\{(4m-5)\frac{\psi_x}{2}+(4n-7)\frac{\psi_y}{2}+\beta_{(2m)(2n)}\}} E_4)
\end{aligned}
\tag{5.13}
$$

To make the excitations for each port more clear, Fig. 5.4 shows the excitation for each port with its given electric field pattern extracted at the origin.

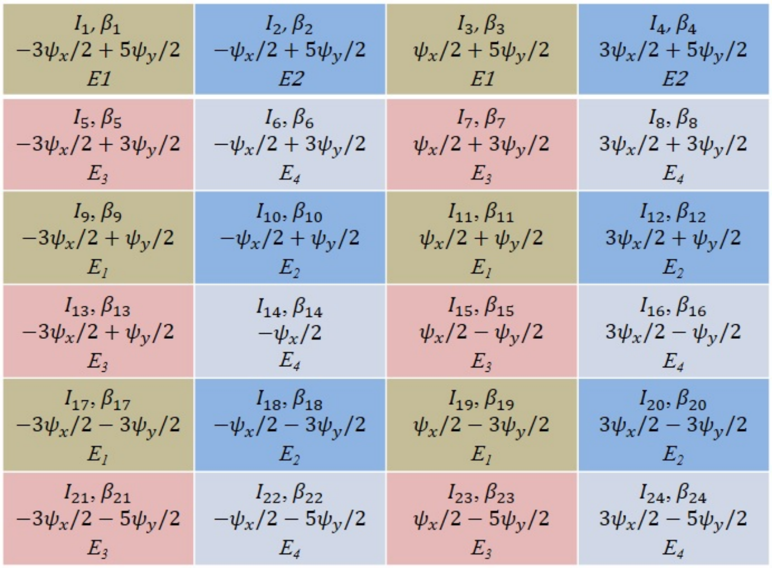

I_1, β_1 $-3\psi_x/2 + 5\psi_y/2$ E1	I_2, β_2 $-\psi_x/2 + 5\psi_y/2$ E2	I_3, β_3 $\psi_x/2 + 5\psi_y/2$ E1	I_4, β_4 $3\psi_x/2 + 5\psi_y/2$ E2
I_5, β_5 $-3\psi_x/2 + 3\psi_y/2$ E_3	I_6, β_6 $-\psi_x/2 + 3\psi_y/2$ E_4	I_7, β_7 $\psi_x/2 + 3\psi_y/2$ E_3	I_8, β_8 $3\psi_x/2 + 3\psi_y/2$ E_4
I_9, β_9 $-3\psi_x/2 + \psi_y/2$ E_1	I_{10}, β_{10} $-\psi_x/2 + \psi_y/2$ E_2	I_{11}, β_{11} $\psi_x/2 + \psi_y/2$ E_1	I_{12}, β_{12} $3\psi_x/2 + \psi_y/2$ E_2
I_{13}, β_{13} $-3\psi_x/2 + \psi_y/2$ E_3	I_{14}, β_{14} $-\psi_x/2$ E_4	I_{15}, β_{15} $\psi_x/2 - \psi_y/2$ E_3	I_{16}, β_{16} $3\psi_x/2 - \psi_y/2$ E_4
I_{17}, β_{17} $-3\psi_x/2 - 3\psi_y/2$ E_1	I_{18}, β_{18} $-\psi_x/2 - 3\psi_y/2$ E_2	I_{19}, β_{19} $\psi_x/2 - 3\psi_y/2$ E_1	I_{20}, β_{20} $3\psi_x/2 - 3\psi_y/2$ E_2
I_{21}, β_{21} $-3\psi_x/2 - 5\psi_y/2$ E_3	I_{22}, β_{22} $-\psi_x/2 - 5\psi_y/2$ E_4	I_{23}, β_{23} $\psi_x/2 - 5\psi_y/2$ E_3	I_{24}, β_{24} $3\psi_x/2 - 5\psi_y/2$ E_4

Figure 5.4: 6 × 4 antenna array amplitude and phase excitations.

To have a beam with broadside direction, the array elements should be uniformly excited with zero progressive phase excitation. Fig. 5.5 shows the amplitude and phase excitations along the whole 24 ports. The normalized AF of a 6×4 array is shown in Fig. 5.6. The AF is found by the same Eq. (5.13), but just by removing the patterns (E_1, E_2, E_3, E_4). The AF can represent the location of side lobes and their values, but with shift and scaled amplitudes. The normalized patterns using the algorithm and CST simulator are shown in Figs. 5.7,5.8. The algorithm here can be compared with the simulation results, so we can check the validity of the proposed algorithm.

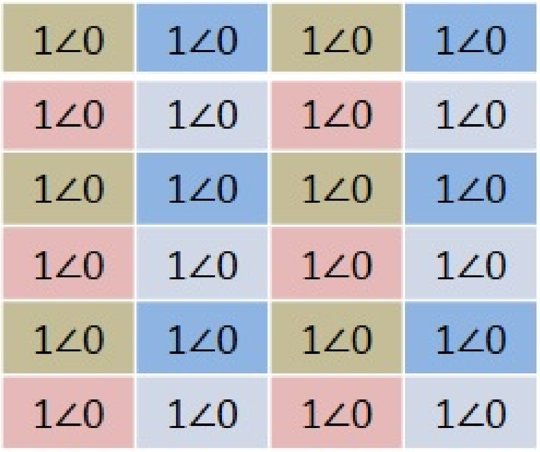

$1\angle 0$	$1\angle 0$	$1\angle 0$	$1\angle 0$
$1\angle 0$	$1\angle 0$	$1\angle 0$	$1\angle 0$
$1\angle 0$	$1\angle 0$	$1\angle 0$	$1\angle 0$
$1\angle 0$	$1\angle 0$	$1\angle 0$	$1\angle 0$
$1\angle 0$	$1\angle 0$	$1\angle 0$	$1\angle 0$
$1\angle 0$	$1\angle 0$	$1\angle 0$	$1\angle 0$

Figure 5.5: Uniform excitations for broadside direction.

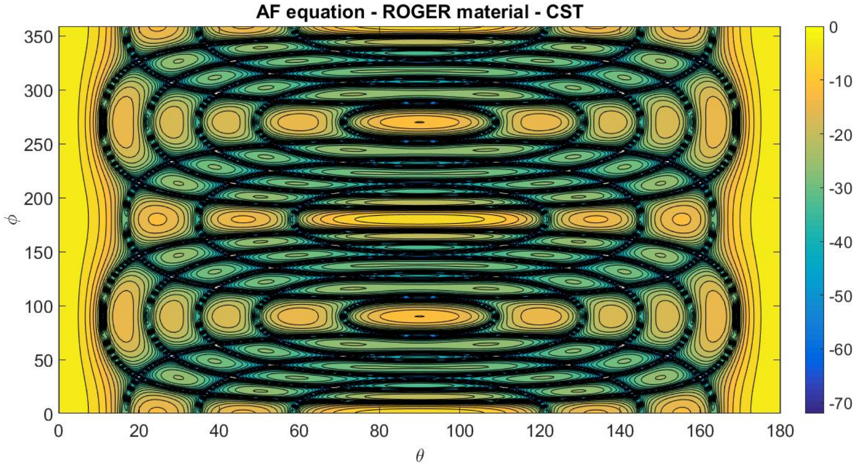

Figure 5.6: Normalized AF of 24 antennas using Fig. 5.5 excitations.

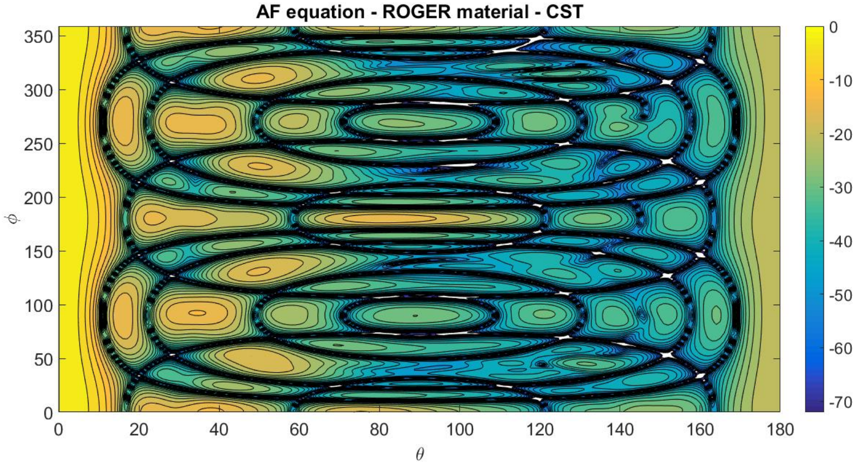

Figure 5.7: Normalized pattern of 24 antennas using equ. (5.13) based on the single port patterns of CST simulation results using Fig. 5.5 excitations.

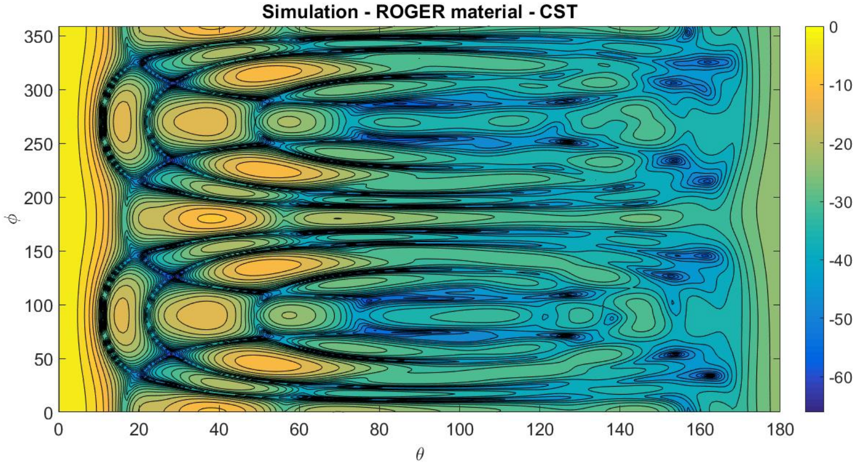

Figure 5.8: Normalized simulated pattern of 24 antennas using CST simulator using Fig. 5.5 excitations.

The 3D pattern in the three cases shows the maximum at $\theta = 0$ as expected for broadside array with 20 dBi simulated realized gain. But a high SLL level appears, 3.3 dB in AF pattern, 11.2 dB using the algorithm, and 8.31 dB in simulated pattern. This is because the large spacing between the ports. Also, different beam boresight angles by each port contributes in new maxima's as side lobes, and the fixed side lobes of each port pattern affects the total SLL.

5.3 SLL reduction

Amplitude excitations plays a main role in SLL reduction. The Binomial technique is one of most popular ones that is based on changing amplitude excitations to reduce the SLL. Here we are trying to reduce SLL by changing the ports excitations using some well-known techniques.

5.3.1 Binomial along x direction

Here, the binomial excitation that is based on the Pascal's triangle [36] is applied along the x-axis direction for 4 elements as shown in figure 5.9. The AF, applied algorithm and CST simulated results for normalized patterns are shown in Figs. 5.10, 5.11 and 5.12, respectively. The SLL in AF is 1.87 dB, which gets worse than the uniform excitations. The SLL using the proposed algorithm remains almost the same (11.3 dB), while it is improved not that much in simulations (9.58 dB). But, the half-power beamwidth HPBW at ϕ=0^o cut (HPBW=20^o) has different value than it is at ϕ=90^o cut (HPBW=10^o).

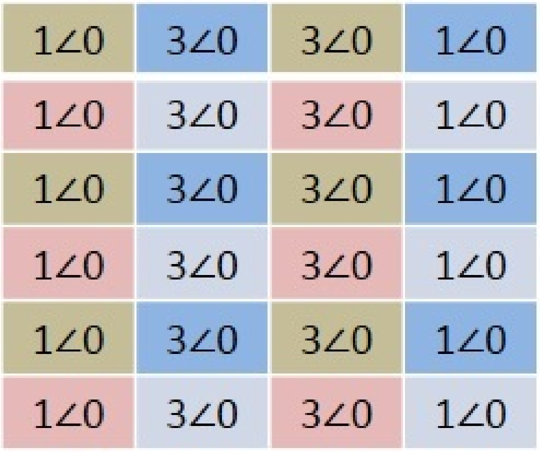

$1\angle0$	$3\angle0$	$3\angle0$	$1\angle0$
$1\angle0$	$3\angle0$	$3\angle0$	$1\angle0$
$1\angle0$	$3\angle0$	$3\angle0$	$1\angle0$
$1\angle0$	$3\angle0$	$3\angle0$	$1\angle0$
$1\angle0$	$3\angle0$	$3\angle0$	$1\angle0$
$1\angle0$	$3\angle0$	$3\angle0$	$1\angle0$

Figure 5.9: Binomial excitation along x direction.

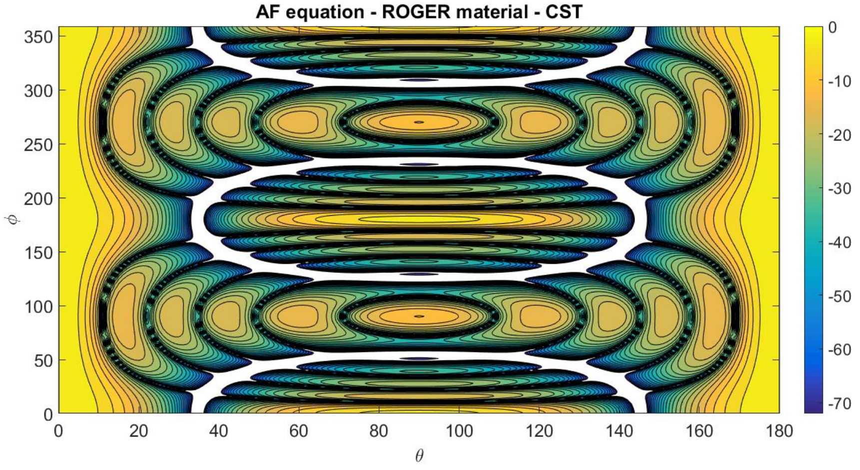

Figure 5.10: AF using Fig. 5.9 excitations.

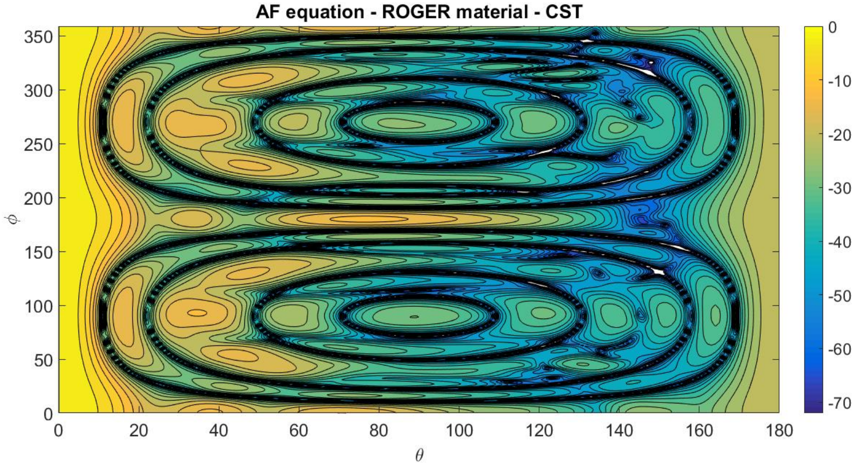

Figure 5.11: Normalized pattern using Fig. 5.9 excitations.

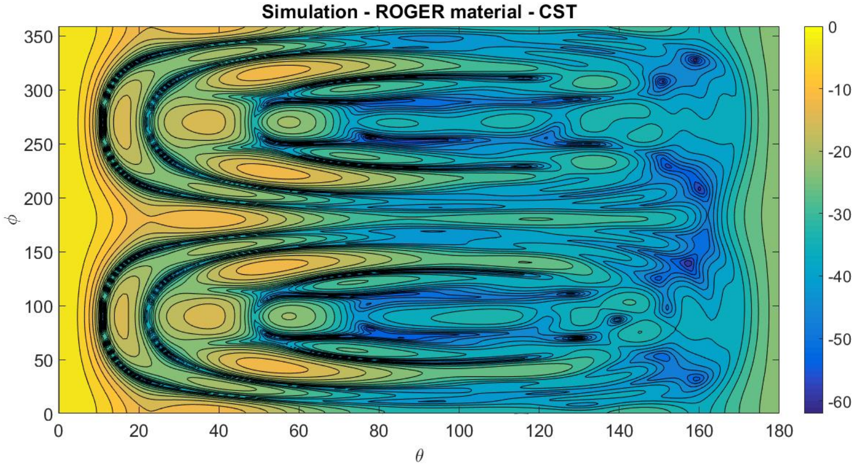

Figure 5.12: Normalized simulated (CST) pattern using Fig. 5.9 excitations.

5.3.2 Binomial along y direction

Binomial excitation is applied along y-axis direction for 6 elements as shown in figure 5.13. The AF, applied algorithm and CST simulated results for normalized patterns are shown in Fig.'s 5.14, 5.15 and 5.16, respectively. The SLL in AF is 3.1 dB, which is almost the same as in uniform excitations. The SLL using the proposed algorithm remains almost the same (11.2 dB), as well as in simulations (8 dB). The HPBW equals to 15^o at all ϕ cuts.

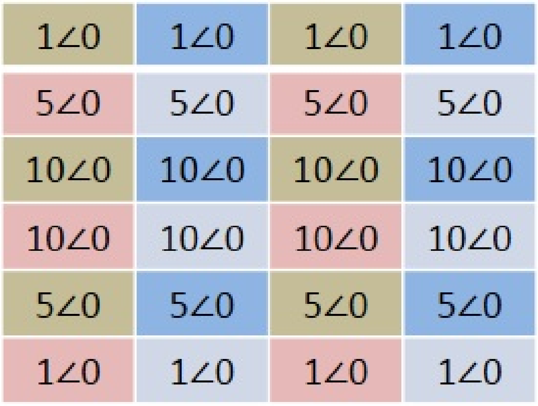

1∠0	1∠0	1∠0	1∠0
5∠0	5∠0	5∠0	5∠0
10∠0	10∠0	10∠0	10∠0
10∠0	10∠0	10∠0	10∠0
5∠0	5∠0	5∠0	5∠0
1∠0	1∠0	1∠0	1∠0

Figure 5.13: Binomial excitation along y direction.

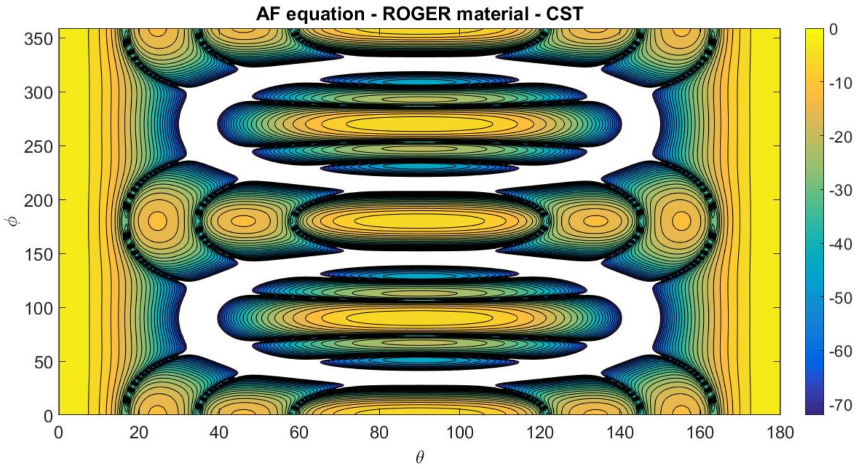

Figure 5.14: AF using Fig. 5.13 excitations.

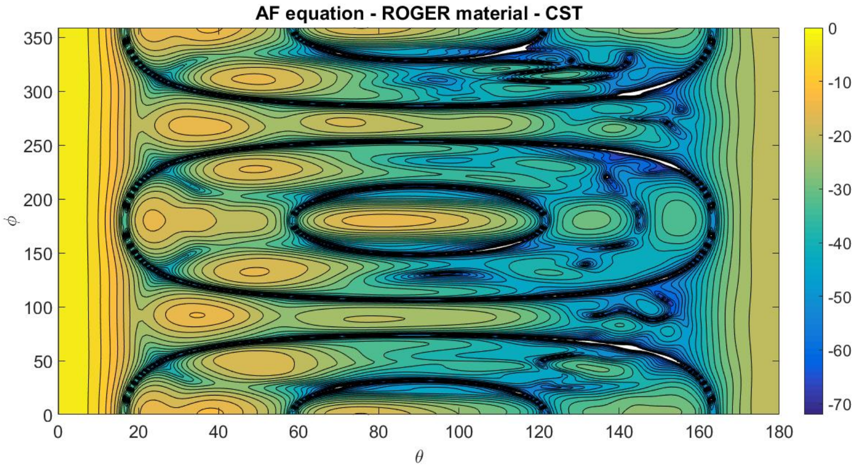

Figure 5.15: Normalized pattern using Fig. 5.13 excitations.

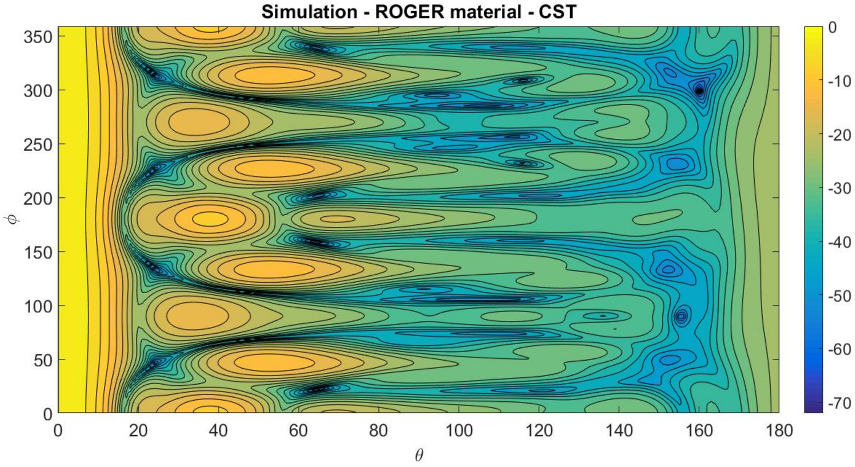

Figure 5.16: Normalized simulated (CST) pattern using Fig. 5.13 excitations.

5.3.3 Chebyshev along x direction (R=40dB)

Chebyshev excitation (desired SLL of $R = 40dB$) is applied along x-axis direction as shown in Fig. 5.17. The AF, applied algorithm and CST simulated results for normalized patterns are shown in Fig.'s 5.18, 5.19 and 5.20, respectively. The SLL in AF is 1.9 dB, which gets worse than the uniform excitations. The SLL using the proposed algorithm is 11.2 dB as in uniform excitations, while it is improved not that much in simulations (9.45 dB). But, the half-power beamwidth HPBW at ϕ=0^o cut (HPBW=19^o) has different value than it is at ϕ=90^o cut (HPBW=10^o).

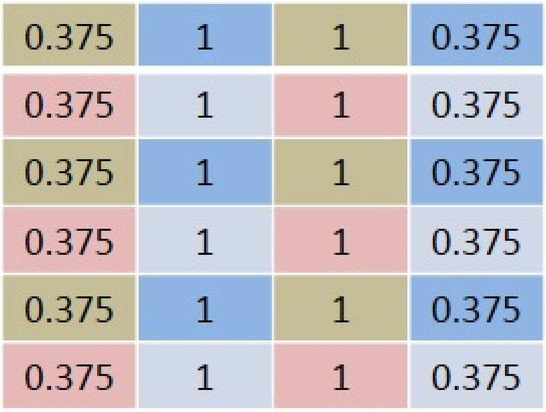

0.375	1	1	0.375
0.375	1	1	0.375
0.375	1	1	0.375
0.375	1	1	0.375
0.375	1	1	0.375
0.375	1	1	0.375

Figure 5.17: Chebyshev excitation along x direction ($R = 40dB$).

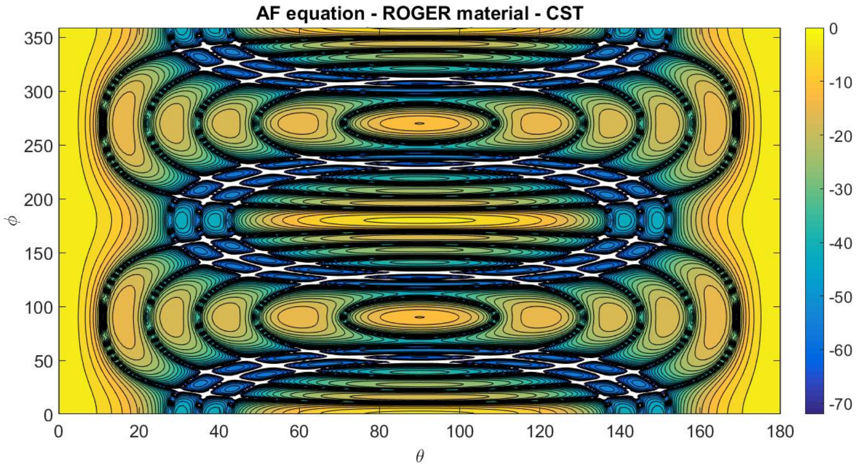

Figure 5.18: AF using Fig. 5.17 excitations.

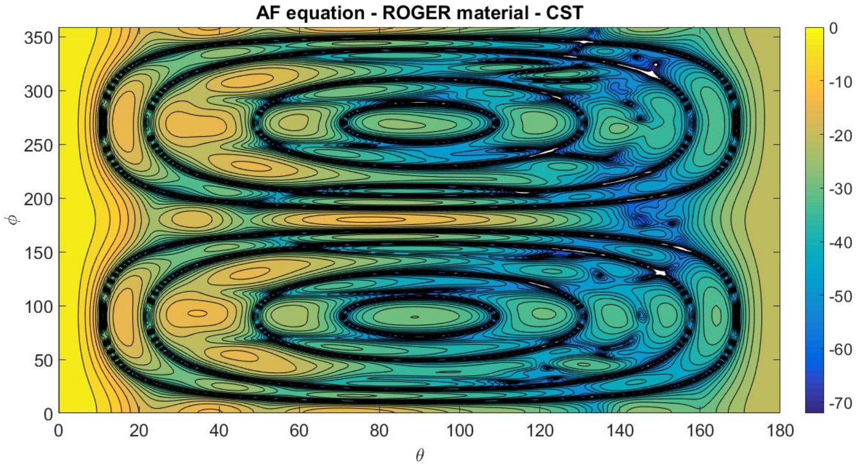

Figure 5.19: Normalized pattern using Fig. 5.17 excitations.

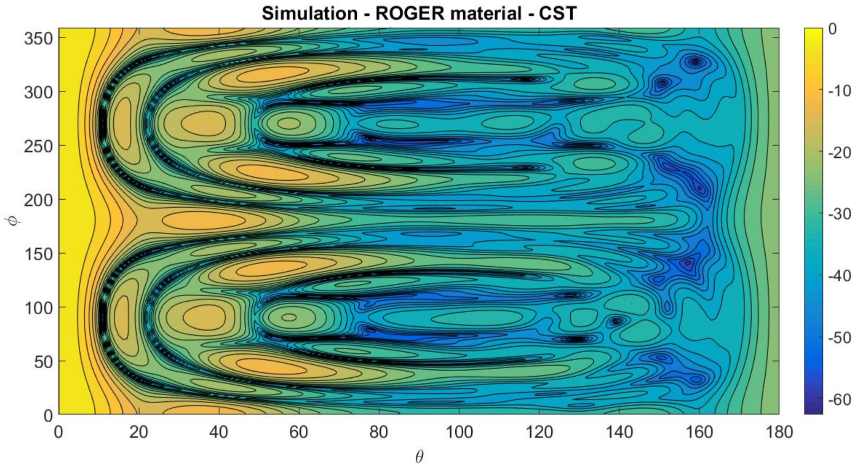

Figure 5.20: Normalized simulated (CST) pattern using Fig. 5.17 excitations.

5.3.4 Chebyshev along y direction (R=40dB)

Chebyshev excitation is applied along y-axis direction with $R = 40dB$ for 6 elements as shown in figure 5.21. The AF, applied algorithm and CST simulated results for normalized patterns are shown in Fig.'s 5.22, 5.23 and 5.24, respectively. The SLL in AF is 3.3 dB, which is almost the same as in uniform excitations. The SLL using the proposed algorithm remains almost the same (11.2 dB), as well as in simulations (8 dB). The HPBW equals to about 15^o at all ϕ cuts.

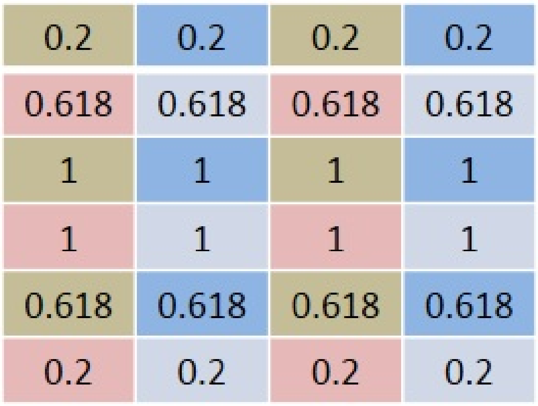

0.2	0.2	0.2	0.2
0.618	0.618	0.618	0.618
1	1	1	1
1	1	1	1
0.618	0.618	0.618	0.618
0.2	0.2	0.2	0.2

Figure 5.21: Chebyshev excitation along y direction ($R = 40dB$).

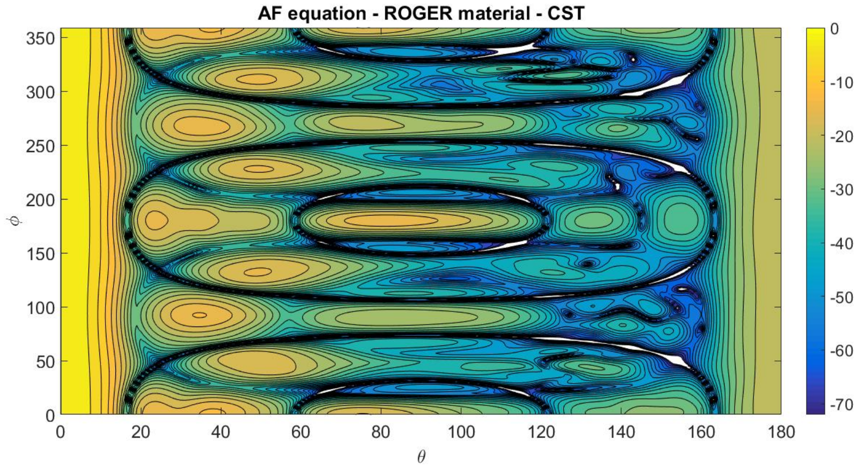

Figure 5.22: AF using Fig. 5.21 excitations.

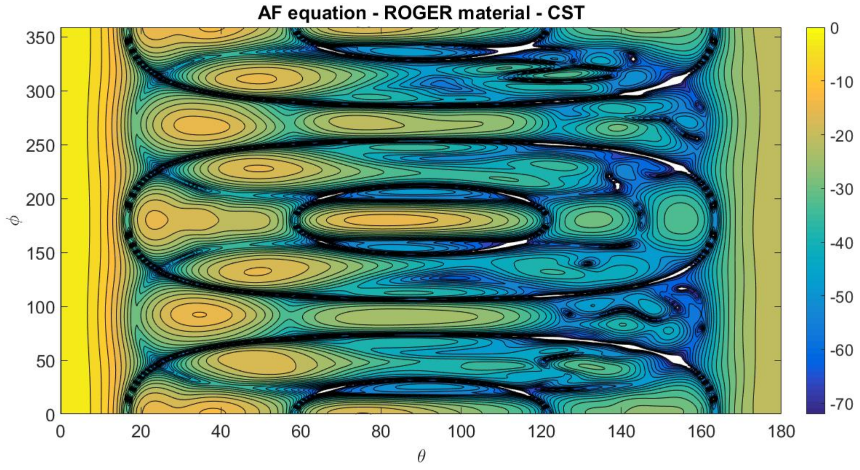

Figure 5.23: Normalized pattern using Fig. 5.21 excitations.

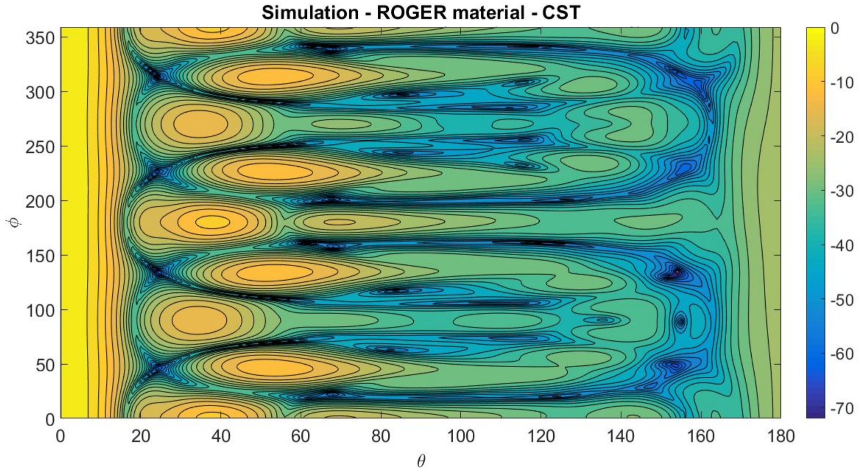

Figure 5.24: Normalized simulated (CST) pattern using Fig. 5.21 excitations.

5.3.5 Summary

To summarize the results in terms of SLL at main side lobes using Binomial and Chebyshev techniques, Table 5.1 shows the effects on SLL, half-power beamwidth (HPBW) and realized gain. The SLL has not improve, and this comes basically from the fixed tilted beams by each port. According to the HPBW, it shows non-equal coverage degrees in any ϕ cut except in using Binomial or Chebyshev excitations along y-axis. In this work, Chebyshev's excitations along y-axis will be used because the ratio between array element amplitude excitations didn't exceed 1:5 (the ratio between the minimum amplitude and the maximum one), where the largest ratio in Binomial along y-axis technique reaches to 1:10.

Table 5.1: Comparison between different SLL reduction techniques.

	SLL (AF) (dB)	SLL (Algorithm) (dB)	SLL (CST) (dB)	HPBW-θ (Algorithm)	HPBW-θ (CST)	Realized Gain (dBi)
Uniform	3.3	11.2	8.31	10-15	9-14	20
Binomial-x	1.87	11.3	9.58	10-20	9-19	19.16
Binomial-y	3.1	11.2	8	15	14-15	18.32
Chebyshev-x	1.9	11.2	9.45	10-19	10-18	19.3
Chebyshev-y	3.3	11.2	8	14-15	14	18.9

5.4 Switched Beamsteering

From previous section, Chebyshev along y-axis will be used for amplitude excitation in steering the main beam. To steer the beam towards different directions, the phase excitation should be changed according to the desired tilt angle. Here are 10 possible angles (areas) that our array can cover.

5.4.1 Case No. 1

Phase excitations that is shown in Fig. 5.25(a) are used to tilt the beam towards $\theta = 12, \phi = 0$ degrees. Fig. 5.25(b) shows the simulation 3D contour plot results of used excitations. Fig. 5.26 shows the resulted pattern by applying the proposed algorithm on the four basic patterns from the simulation. The simulated SLL is 6.95 dB, where it is 6.6 dB using the algorithm. HPBW is almost equal in both simulation and algorithm results, and it is along θ direction from 6^o-20^o, and along ϕ direction from -30^o-29^o. The simulated realized gain is 18.51 dBi.

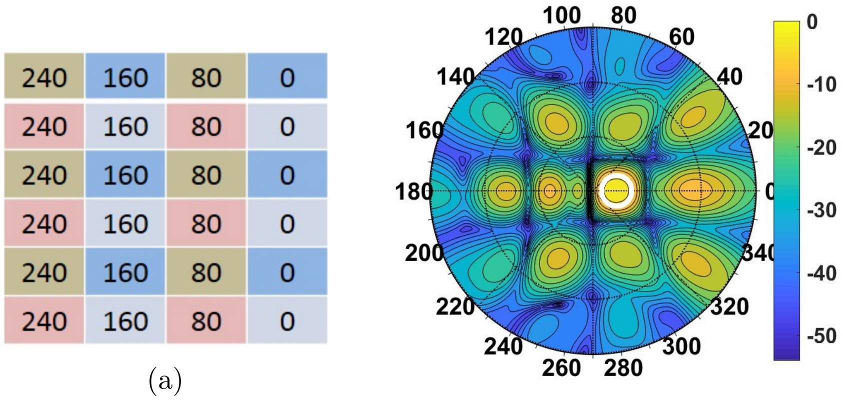

240	160	80	0
240	160	80	0
240	160	80	0
240	160	80	0
240	160	80	0
240	160	80	0

(a)

(b)

Figure 5.25: (a) Phase excitations for steering the beam towards $\theta = 12, \phi = 0$ degrees. (b) Normalized pattern using CST simulator based on given excitations.

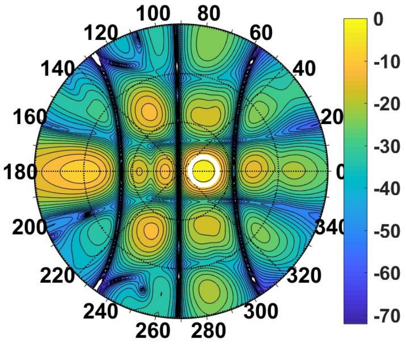

Figure 5.26: Normalized pattern using excitations of Fig. 5.25 with the four basic patterns from CST simulation.

5.4.2 Case No. 2

Phase excitations and simulated results are shown in Fig. 5.27 to tilt the beam towards $\theta = 12, \phi = 90$ degrees. Fig. 5.28 shows the resulted pattern by applying the proposed algorithm on the four basic patterns from the simulation. The simulated SLL is 9.8 dB, where it is 8.47 dB using the algorithm. HPBW is almost equal in both simulation and algorithm results, and it is along θ direction from 6^o-20^o, and along ϕ direction from 56^o-122^o. The simulated realized gain is 18.76 dBi.

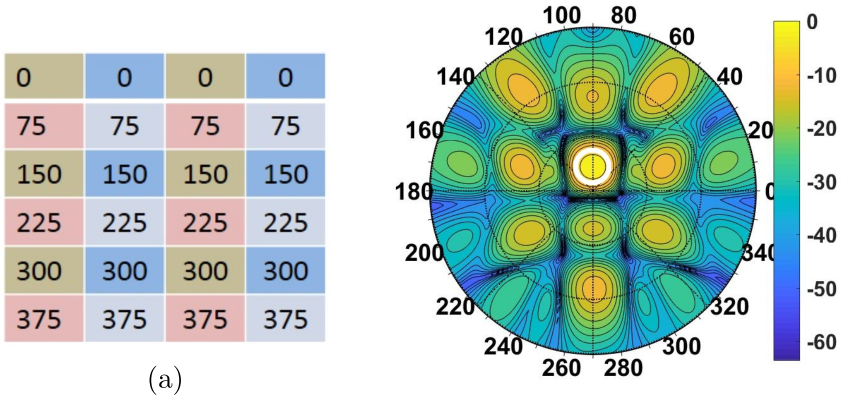

0	0	0	0
75	75	75	75
150	150	150	150
225	225	225	225
300	300	300	300
375	375	375	375

(a)

(b)

Figure 5.27: (a) Phase excitations for steering the beam towards $\theta = 12, \phi = 90$ degrees. (b) Normalized pattern using CST simulator based on given excitations.

5.4.3 Case No. 3

Phase excitations and simulated results are shown in Fig. 5.29 to tilt the beam towards $\theta = 12, \phi = 180$ degrees. Fig. 5.30 shows the resulted pattern by applying the proposed algorithm on the four basic patterns from the simulation. The simulated SLL is 6.95 dB, where it is 6.3 dB using the algorithm. HPBW is

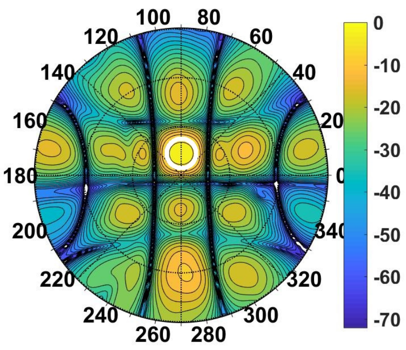

Figure 5.28: Normalized pattern using excitations of Fig. 5.27 with the four basic patterns from CST simulation.

almost equal in both simulation and algorithm results, and it is along θ direction from 6^o-20^o, and along ϕ direction from 150^o-210^o. The simulated realized gain is 18.52 dBi.

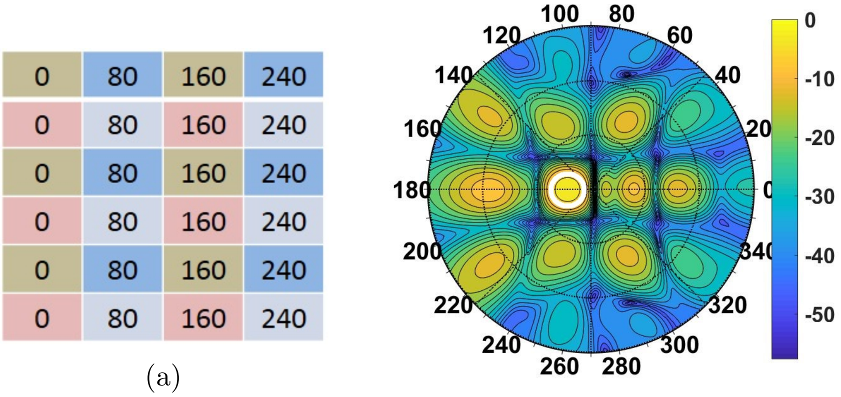

0	80	160	240
0	80	160	240
0	80	160	240
0	80	160	240
0	80	160	240
0	80	160	240

(a)

(b)

Figure 5.29: (a) Phase excitations for steering the beam towards $\theta = 12, \phi = 180$ degrees. (b) Normalized pattern using CST simulator based on given excitations.

5.4.4 Case No. 4

Phase excitations and simulated results are shown in Fig. **??** to tilt the beam towards $\theta = 12, \phi = 270$ degrees. Fig. 5.32 shows the resulted pattern by applying

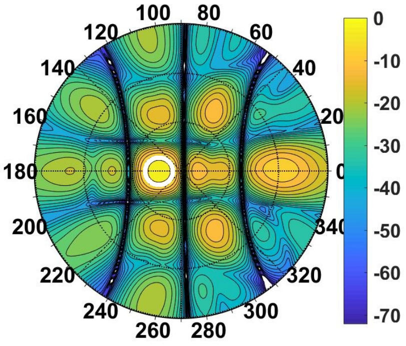

Figure 5.30: Normalized pattern using excitations of Fig. 5.29 with the four basic patterns from CST simulation.

the proposed algorithm on the four basic patterns from the simulation. The simulated SLL is 9.87 dB, where it is 10.2 dB using the algorithm. HPBW is almost equal in both simulation and algorithm results, and it is along θ direction from 7^o-20^o, and along ϕ direction from 239^o-303^o. The simulated realized gain is 18.8 dBi.

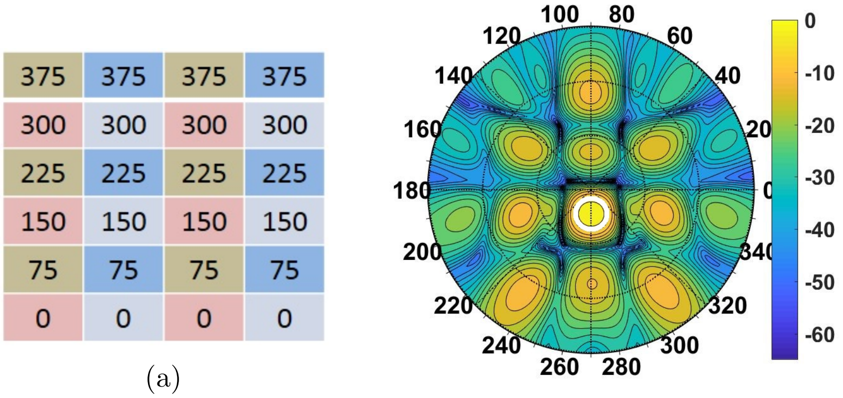

375	375	375	375
300	300	300	300
225	225	225	225
150	150	150	150
75	75	75	75
0	0	0	0

(a)

(b)

Figure 5.31: (a) Phase excitations for steering the beam towards $\theta = 12, \phi = 270$ degrees. (b) Normalized pattern using CST simulator based on given excitations.

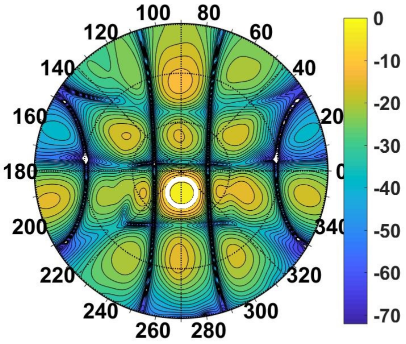

Figure 5.32: Normalized pattern using excitations of Fig. 5.31 with the four basic patterns from CST simulation.

5.4.5 Case No. 5

Phase excitations and simulated results are shown in Fig. 5.33 to tilt the beam towards $\theta = 20, \phi = 45$ degrees. Fig. 5.34 shows the resulted pattern by applying the proposed algorithm on the four basic patterns from the simulation. The simulated SLL is 6.82 dB, where it is 5.84 dB using the algorithm. HPBW is almost equal in both simulation and algorithm results, and it is along θ direction from 12^o-26^o, and along ϕ direction from 25^o-67^o. The simulated realized gain is 17.84 dBi.

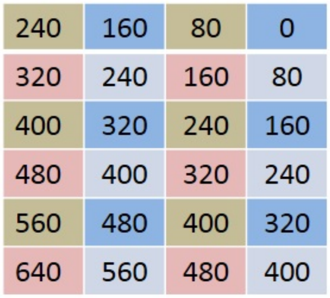

240	160	80	0
320	240	160	80
400	320	240	160
480	400	320	240
560	480	400	320
640	560	480	400

(a)

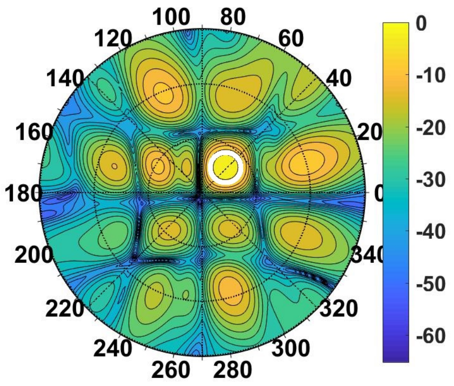

(b)

Figure 5.33: (a) Phase excitations for steering the beam towards $\theta = 20, \phi = 45$ degrees. (b) Normalized pattern using CST simulator based on given excitations.

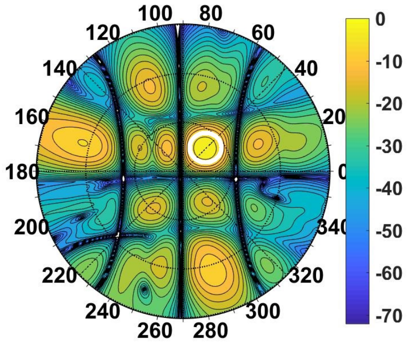

Figure 5.34: Normalized pattern using excitations of Fig. 5.33 with the four basic patterns from CST simulation.

5.4.6 Case No. 6

Phase excitations and simulated results are shown in Fig. 5.35 to tilt the beam towards $\theta = 20, \phi = 135$ degrees. Fig. 5.36 shows the resulted pattern by applying the proposed algorithm on the four basic patterns from the simulation. The simulated SLL is 6.77 dB, where it is 5.85 dB using the algorithm. HPBW is almost equal in both simulation and algorithm results, and it is along θ direction from 12^o-26^o, and along ϕ direction from 113^o-154^o. The simulated realized gain is 17.86 dBi.

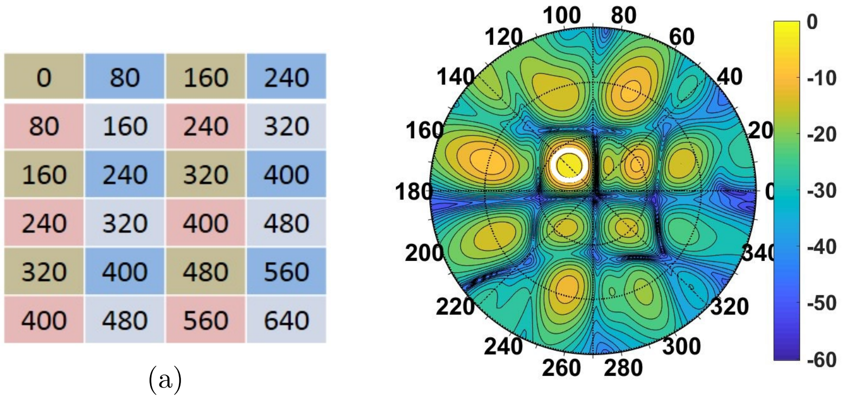

0	80	160	240
80	160	240	320
160	240	320	400
240	320	400	480
320	400	480	560
400	480	560	640

(a)

(b)

Figure 5.35: (a) Phase excitations for steering the beam towards $\theta = 20, \phi = 135$ degrees. (b) Normalized pattern using CST simulator based on given excitations.

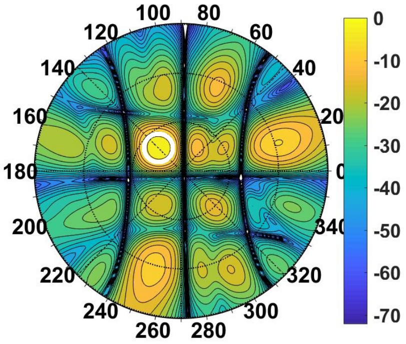

Figure 5.36: Normalized pattern using excitations of Fig. 5.35 with the four basic patterns from CST simulation.

5.4.7 Case No. 7

Phase excitations and simulated results are shown in Fig. 5.37 to tilt the beam towards $\theta = 20, \phi = 225$ degrees. Fig. 5.38 shows the resulted pattern by applying the proposed algorithm on the four basic patterns from the simulation. The simulated SLL is 6.75 dB, where it is 6.24 dB using the algorithm. HPBW is almost equal in both simulation and algorithm results, and it is along θ direction from 12^o-26^o, and along ϕ direction from 206^o-247^o. The simulated realized gain is 17.91 dBi.

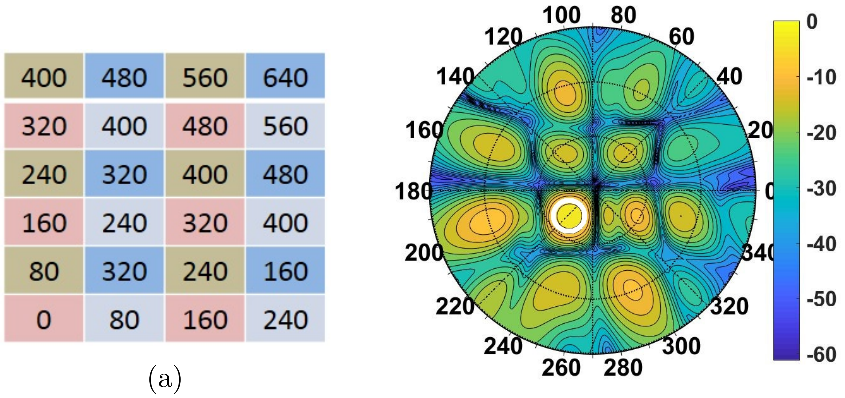

400	480	560	640
320	400	480	560
240	320	400	480
160	240	320	400
80	320	240	160
0	80	160	240

(a)

(b)

Figure 5.37: (a) Phase excitations for steering the beam towards $\theta = 20, \phi = 225$ degrees. (b) Normalized pattern using CST simulator based on given excitations.

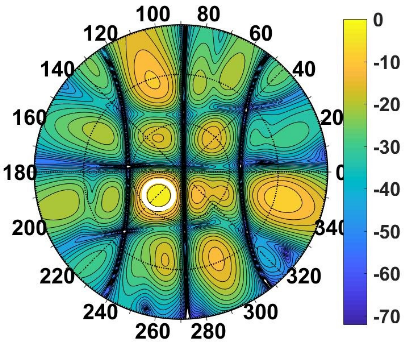

Figure 5.38: Normalized pattern using excitations of Fig. 5.37 with the four basic patterns from CST simulation.

5.4.8 Case No. 8

Phase excitations and simulated results are shown in Fig. 5.39 to tilt the beam towards $\theta = 20, \phi = 315$ degrees. Fig. 5.40 shows the resulted pattern by applying the proposed algorithm on the four basic patterns from the simulation. The simulated SLL is 6.78 dB, where it is 6.6 dB using the algorithm. HPBW is almost equal in both simulation and algorithm results, and it is along θ direction from 12^o-26^o, and along ϕ direction from 292^o-334^o. The simulated realized gain is 17.91 dBi.

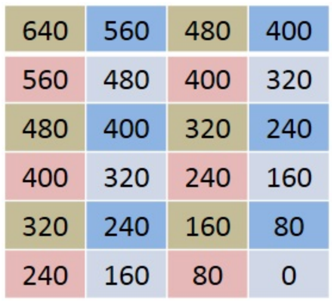

640	560	480	400
560	480	400	320
480	400	320	240
400	320	240	160
320	240	160	80
240	160	80	0

(a)

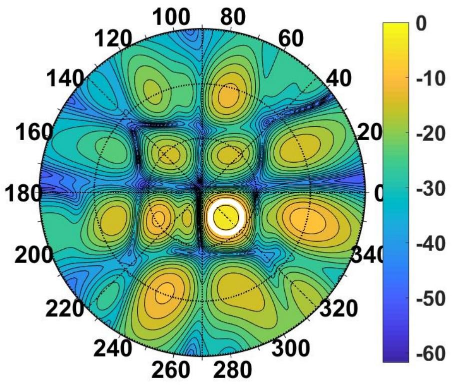

(b)

Figure 5.39: (a) Phase excitations for steering the beam towards $\theta = 20, \phi = 315$ degrees. (b) Normalized pattern using CST simulator based on given excitations.

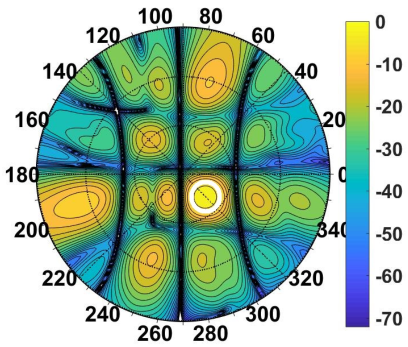

Figure 5.40: Normalized pattern using excitations of Fig. 5.39 with the four basic patterns from CST simulation.

5.4.9 Case No. 9

Phase excitations and simulated results are shown in Fig. 5.41 to tilt the beam towards $\theta = 30, \phi = 0\&180$ degrees. Fig. 5.42 shows the resulted pattern by applying the proposed algorithm on the four basic patterns from the simulation. Two beams are supported by this excitations. The simulated SLL is 1.7 dB, where it is 4.53 dB using the algorithm. HPBW is almost equal in both simulation and algorithm results at the two beams. For the first beam, HPBW along θ direction is from 23^o-35^o, and along ϕ direction is from -13^o-13^o. The HPBW for the second beam along θ direction is from 23^o-35^o, and along ϕ direction is from 167^o-192^o.

The simulated realized gain is 11.93 dBi.

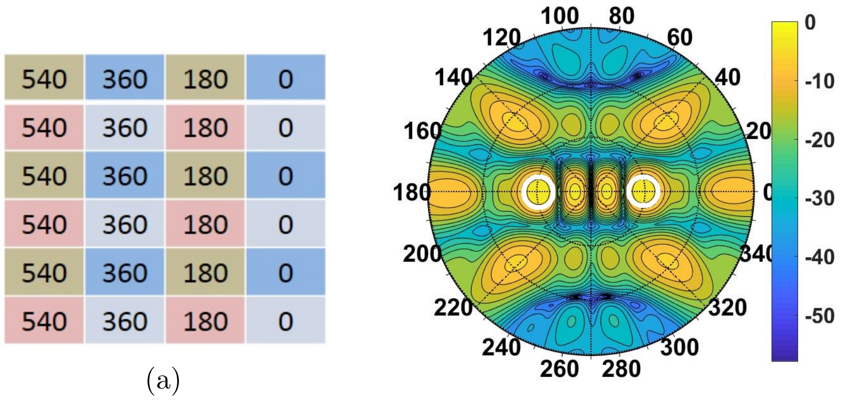

540	360	180	0
540	360	180	0
540	360	180	0
540	360	180	0
540	360	180	0
540	360	180	0

(a)

(b)

Figure 5.41: (a) Phase excitations for steering the beam towards $\theta = 30, \phi = 0\&180$ degrees. (b) Normalized pattern using CST simulator based on given excitations.

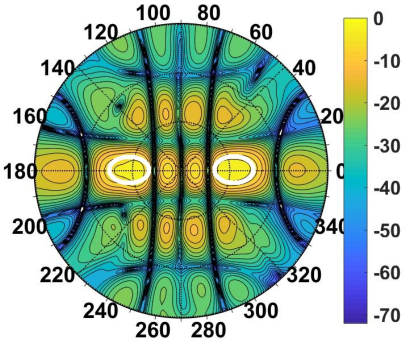

Figure 5.42: Normalized pattern using excitations of Fig. 5.41 with the four basic patterns from CST simulation.

5.4.10 Case No. 10

Phase excitations and simulated results are shown in Fig. 5.43 to tilt the beam towards $\theta = 32, \phi = 90\&270$ degrees. Fig. 5.44 shows the resulted pattern by applying the proposed algorithm on the four basic patterns from the simulation. The simulated SLL is 8 dB, where it is 9.4 dB using the algorithm. HPBW is almost equal in both simulation and algorithm results at the two beams. For the first beam, HPBW along θ direction is from 26^o-40^o, and along ϕ direction is from 77^o-103^o. The HPBW for the second beam along θ direction is from 25^o-40^o, and along ϕ direction is from 257^o-283^o. The simulated realized gain is 16.55 dBi.

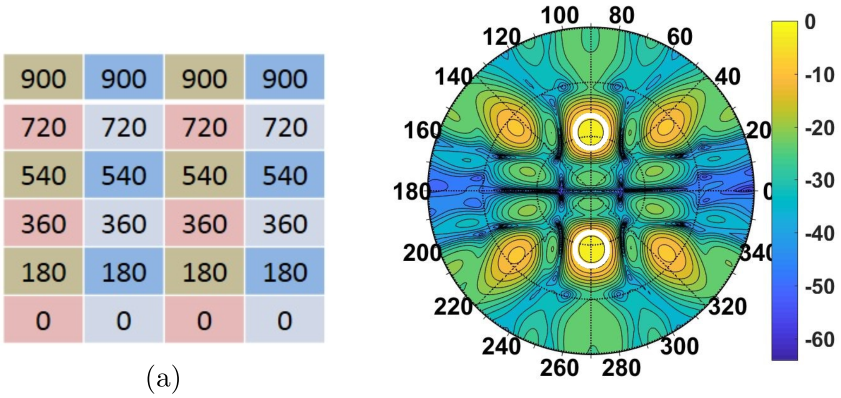

900	900	900	900
720	720	720	720
540	540	540	540
360	360	360	360
180	180	180	180
0	0	0	0

(a)

(b)

Figure 5.43: (a) Phase excitations for steering the beam towards $\theta = 32, \phi = 90\&270$ degrees. (b) Normalized pattern using CST simulator based on given excitations.

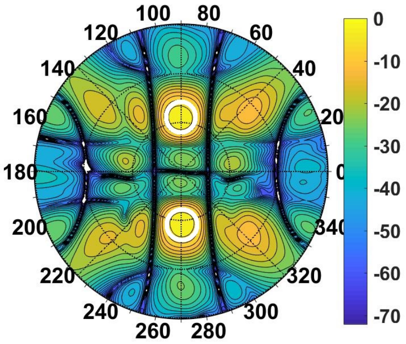

Figure 5.44: Normalized pattern using excitations of Fig. 5.43 with the four basic patterns from CST simulation.

5.4.11 Summary

Table 5.2 shows the coverage areas and the SLL and the gain for each case. By steering the beam to higher angles in θ, the SLL gets lower, and the gain gets lower too. The SLLs values are almost similar in both simulation and algorithm results. The gain is decreased gradually from the maximum at broadside (18.9 dBi) to have a gain of 16.55 dBi in Case no. 10. The odd case is no. 9, which has a very low value of gain (11.93 dBi) comparing with others, and this low value comes from high level at side lobes, which reaches to 1.7 dB in simulations. The main reason for high side lobes here comparing with other cases is that the array is not symmetric, so the number of elements along the axis that is responsible on steering the beam towards the desired angle (θ=30^o,ϕ=0^o,180^o), which is 4 elements, are not enough to cover that angle in elevation. Where in case no. 10, the axis that is responsible on steering the beam contains 6 elements. By gathering all cases in one plot, we can get Fig. 5.45.

Table 5.2: Comparison between different coverage areas cases.

Case No.	θ_o (degrees)	ϕ_o (degrees)	HPBW (θ) (degrees) (Algorithm)	HPBW (θ) (degrees) (CST)	HPBW (ϕ) (degrees) (Algorithm)	HPBW (ϕ) (degrees) (CST)	SLL (Algorithm) (dB)	SLL (CST) (dB)	Gain (dBi)
Case No. 1	13	0	6.5-20.5	6-20	330-29	328-31	6.6	6.95	18.51
Case No. 2	13	90	6.5-20.5	6.5-20	56-122	58-122	8.47	9.8	18.76
Case No. 3	13	180	6.5-20.5	6-20	150-210	149-212	6.3	6.95	18.52
Case No. 4	13	270	7-20.5	6.5-20	239-303	238-302	10.2	9.87	18.8
Case No. 5	20	226	12-26	12-26	25-67	26-68	5.84	6.82	17.84
Case No. 6	20	46	12.5-27	12-26	113-154	112-154	5.85	6.77	17.86
Case No. 7	20	134	12.5-27	12-26	206-247	206-248	6.24	6.75	17.91
Case No. 8	20	313	12.5-26.5	12-26	292-334	292-334	6.6	6.78	17.91
Case No. 9	30	0,180	22-42 22.5-41	23-35.5 23-35.5	347-13 167-192	347-13 167-199	4.53	1.7	11.93
Case No. 10	32	90,270	26-40 24-40	25-39.5 25-39.5	77-103 257-284	77-102 257-283	9.4	8	16.55

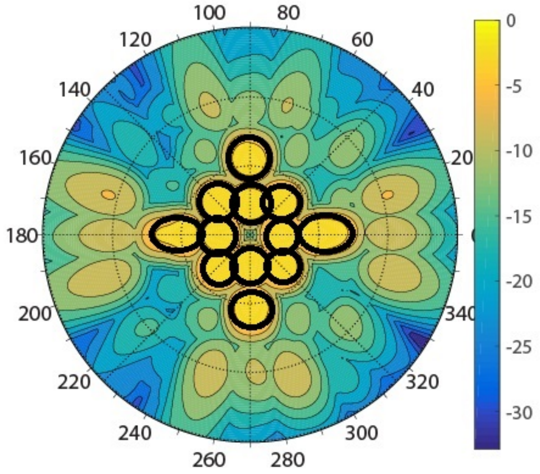

Figure 5.45: Normalized pattern using the algorithm showing all 10 cases (12 beams).

CHAPTER 6

CONCLUSIONS AND FUTURE WORK

6.1 Conclusion

5G is going to be applied by 2020, and one of the key technologies is mMIMO systems. In mMIMO, large number of antennas are utilized at the base station side. The capacity in 5G is much larger (about 1000×) than its in 4G, and mMIMO plays a main role in channel capacity enhancement. So, the mMIMO antenna systems is one of the hot areas for researchers.

In this work, a design of a mMIMO antenna system is presented that is supporting two operating modes; simultaneous individual port operation and mMIMO array operation. The design is based on patch antennas. Each 2×2 patches are excited in a way to tilt their beam. The tilts at every subarray is made to achieve low correlation between them. The array is made at the beginning with 16 ports for the board, but since the fixed board sizes, 24 ports are utilized at one board. A 24 subarrays are distributed on a board, that is one of three boards which is the proposed base station. Triangular shape is used instead of hexagonal one because of cost limitations. The three boards are fabricated and measured, and a good agreement were noticed between the measurement results and simulated ones. The minimum achieved bandwidth is about 100 MHz over 3.5 GHz band. It is shifted down from the proposed resonance (3.6 GHz) that comes from the fabrication process. The maximum measured gain by single subarray is 9.4 dBi, with measured efficiency of 64%. The maximum ECC between the ports was 0.1192.

After that, a beamsteering algorithm is introduced to operate the designed MIMO system in array mode. The algorithm is used to run a switched beam array to cover specific spots. Then, the performance is observed in terms of HPPW and the realized gain. 13 beams (including broadside) are shown that covers from broadside to 32^o in elevation. The gain dropped down from 18.9 dBi at broadside direction to 11.93 dBi at the beam towards the last beam tilt angle. The HPBW along ϕ direction (azimuth plane) also decreased from 60^o at first beam tilt (towards θ=13^o) to 26^o at the last beam tilt angle (towards θ=32^o). The simulated SLL deviates from 1.7 dB for the worst case (case no. 9) to 9.87 dB for the best case (case no. 4). There are blind area equals to 36^o at each board (108^o by whole system) that cannot be covered when operating in switch beamsteering mode system by using Triangular shape. This can be avoided by utilizing Hexagonal shape for base station.

6.2 Future Work

For future work, the array can be redesigned to operate at other frequencies according to different standards. Also, it can be improved to cover a wider band, and to have a higher number of antennas for capacity enhancement. The algorithm can be improved to achieve lower levels in side lobes. And it can be designed depending on the proposed excitations for different switched beams. Also, the beams can be controlled to be more directive with higher gain for the desired users.

REFERENCES

[1] Cisco, ”Cisco Visual Networking Index: Global Mobile Data Traffic Forecast Update, 20162021 (White Paper),” Mar. 2017

[2] E. G. Larsson, F. Tufvesson, O. Edfors, and T. L. Marzetta, ”Massive MIMO for next generation wireless systems,” IEEE Communication Magazine, vol. 52, no. 2, pp. 186195, Feb. 2014.

[3] J. G. Andrews et al., ”What will 5G be?” IEEE J. Sel. Areas Commun., vol. 32, no. 6, pp. 10651082, Jun. 2014.

[4] F. Hu, ”Opportunities in 5G Networks: A Research and Development Perspective,” CRC Press, 2016.

[5] T. L. Marzetta, ”Massive MIMO: An Introduction,” Bell Labs Technical Journal, vol. 20, no. , pp. 11-22, 2015.

[6] F. Rusek, D. Persson, B. K. Lau, E. G. Larsson, T. L. Marzetta, O. Edfors and F. Tufvesson, ”Scaling Up MIMO: Opportunities and Challenges with Very Large Arrays,” IEEE Signal Processing Magazine, vol. 30, no. 1, pp. 40-60, Jan. 2013.

[7] L. Song and J. Shen, "Evolved Cellular Network Planning and Optimization for UMTS and LTE," London, CRC Press, 2011.

[8] L. Lu, G. Y. Li, A. L. Swindlehurst, A. Ashikhmin, and R. Zhang, "An overview of massive MIMO: Benets and challenges," IEEE J. Sel. Topics Signal Process., vol. 8, no. 5, pp. 742758, Oct. 2014.

[9] M. S. Sharawi, "Printed multi-band MIMO antenna systems and their performance metrics," IEEE Antennas Propag. Mag., vol. 55, no. 5, pp. 218232, Oct. 2013.

[10] S. Blanch, J. Romeu and I. Corbella, "Exact Representation of Antenna System Diversity Performance from Input Parameter Description," IET Electronic Letters, 39, 9, May 2003, pp. 705707.

[11] P. Hallbjorner, "The Significance of Efficiencies when Using S-Parameters to Calculate the Received Signal Correlation from Two Antennas," IEEE Antennas and Wireless Propagation Letters, 4, 2005, pp. 97-99.

[12] M. Manteghi and Y. Rahmat-Samii, "Multiport Characteristics of a Wideband Cavity Backed Annular Patch Antenna for Multipolarization Operations," IEEE Transactions on Antennas and Propagation, AP-53, 1, January 2005, pp. 466-474.

[13] T. Taga, "Analysis of Mean Effective Gain of Mobile Antennas in Land Mobile Radio Environments," IEEE Transactions on Vehicular Technology, 39, 2, May 1990, pp. 117-131.

[14] Plicanic, V., ”Diversity Antenna Studies and Evaluations,” Master’s thesis, Lund Institute of Technology, 2004.

[15] C. A. Balanis, ”Antenna Theory, Analysis and design,” 2^{nd} edition John Wiley & Sons, 1997.

[16] D. M. Pozar, ”Microwave Engineering,” Second Edition, New York, John Wiley, 1998.

[17] J. I. Litouw and A. Munir, ”16-port array antenna feeding network with programmable phase shifter capability,” 2015 International Seminar on Intelligent Technology and Its Applications (ISITIA), 2015, pp. 409-412.

[18] R. Garg, I., Bahl and M., Bozzi, ”Microstrip Lines and Slotlines,” Second Edition, Artech House, 2013.

[19] ”ANSYS HFSS: High Frequency Electromagnetic Field Simulation”. Ansys.com, June 2017.

[20] ”CST STUDIO SUITE - Electromagnetic Field Simulation Software - Overview”, Cst.com, June 2017.

[21] P. Xingdong, H. Wei, Y. Tianyang and L. Linsheng, ”Design and implementation of an active multibeam antenna system with 64 RF channels and 256 antenna elements for massive MIMO application in 5G wireless communications,” China Communications, vol.11, no.11, pp.16-23, Nov. 2014

[22] J. Vieira, S. Malkowsky, K.Nieman, Z. Miers, N. Kundargi, L. Liu, I. Wong, V. Owall, O. Edfors and F. Tufvesson, "A flexible 100-antenna testbed for Massive MIMO," Globecom Workshops (GC Wkshps), 2014 , vol., no., pp.287-293, 8-12 Dec. 2014

[23] R. Ma, Y. Gao, L. Cuthbert and Q. Zeng, "Antipodal linearly tapered slot antenna array for millimeter-wave base station in massive MIMO systems," Antennas and Propagation Society International Symposium (APSURSI), 2014 IEEE , vol., no., pp.1121-1122, 6-11 July 2014

[24] S. Rajagopal, S. Abu-Surra, P. Zhouyue and F. Khan, "Antenna Array Design for Multi-Gbps mmWave Mobile Broadband Communication," Global Telecommunications Conference (GLOBECOM 2011), 2011 IEEE , vol., no., pp.1-6, 5-9 Dec. 2011

[25] I. Tzanidis, B. Loong, Y. Li, Y. Nam, G. Xu, J. Zhang; Y. Kim and J. Lee, "Patch antenna array configuration for application in FD-MIMO systems," Antennas and Propagation Society International Symposium (APSURSI), 2013 IEEE , vol., no., pp.2241-2242, 7-13 July 2013

[26] I. Tzanidis, Y. Li, G. Xu, J. Seol, and J. Zhang, "2D Active Antenna Array Design for FD-MIMO System and Antenna Virtualization Techniques," International Journal of Antennas and Propagation, vol. 2015, Article ID 873530, 9 pages, 2015.

[27] A. Jain and S. K. Yadav, "Design and Analysis of Compact 108 Element Multimode Antenna Array for Massive MIMO Base Station," Progress In Electromagnetics Research C, Vol. 61, 179184, 2016.

[28] M. Ali and A. Sebak, "Design of compact millimeter wave massive MIMO dual-band (28/38 GHz) antenna array for future 5G communication systems," 2016 17th International Symposium on Antenna Technology and Applied Electromagnetics (ANTEM), pp. 1-2, July 2016.

[29] Y. Gao, R. Ma, Y. Wang, Q. Zhang and C. Parini, "Stacked Patch Antenna With Dual-Polarization and Low Mutual Coupling for Massive MIMO," IEEE Transactions on Antennas and Propagation, vol. 64, no. 10, pp. 4544-4549, Oct. 2016.

[30] H. Zhou, H. Peng, W. Jin and J. Mao, "A new low-profile and closely spaced dual-polarized antenna for massive-MIMO applications," 2016 IEEE International Conference on Microwave and Millimeter Wave Technology (ICMMT), Beijing, pp. 659-661, June 2016.

[31] S. Krishna and S. Sharma, "A dual polarization massive MIMO panel array antenna at Ka-band with beamforming capability," 2017 United States National Committee of URSI National Radio Science Meeting (USNC-URSI NRSM), pp. 1-2, Jan. 2017.

[32] D. Manteuffel and R. Martens, "Compact Multimode Multielement Antenna for Indoor UWB Massive MIMO," IEEE Transactions on Antennas and Prop-

agation, vol. 64, no. 7, pp. 2689-2697, July 2016.

[33] uniteChannel, ”Active Antenna Demo for 5G by Nokia and Mitsubishi,” https://www.youtube.com, 2015.

[34] X. Gao, O. Edfors, F. Rusek and F. Tufvesson, ”Linear Pre-Coding Performance in Measured Very-Large MIMO Channels,” IEEE Vehicular Technology Conference (VTC Fall), San Francisco, CA, 2011, pp. 1-5.

[35] H.-W. Yuan, G.-F. Cui, and J. Fan, ”A Method for Analyzing Broadcast Beamforming of Massive MIMO Antenna Array,” Progress In Electromagnetics Research Letters, Vol. 65, 15-21, 2017.

[36] R. L. Haupt, ”Antenna Arrays: A Computational Approach,” Wiley-IEEE Press, 2010.

[37] M. A. Al-Tarifi, Y. S. Faouri and M. S. Sharawi, ”A printed 16 ports massive MIMO antenna system with directive port beams,” IEEE 5th Asia-Pacific Conference on Antennas and Propagation (APCAP), Kaohsiung, 2016, pp. 125-126.

Vitae

- Name: Monjed Adnan Ahmed Al-Tarifi
- Nationality: Jordanian
- Date of Birth: 9th Dec. 1991
- Email: *g201409440@kfupm.edu.sa; eetarifi2009@yahoo.com*
- Permenant Address: Zarqa, Jordan

- BSc. in Electrical Engineering / Communications and Electronics, Jordan University for Science and Technology (JUST), Jordan.

Publications

1. M. A. Al-Tarifi, Y. S. Faouri and M. S. Sharawi, ”A printed 16 ports massive MIMO antenna system with directive port beams,” IEEE 5th Asia-Pacific Conference on Antennas and Propagation (APCAP), Kaohsiung, 2016, pp. 125-126.
2. M. A. Al-Tarifi, M. S. Sharawi and A. Shamim, ”A Massive MIMO Antenna System for 5G Base Stations with Directive Ports and Switched Beamsteering Algorithm,” To be Submitted to IEEE Transactions on Antennas and Propagation, May, 2017.